MINISTÉRIO DA EDUCAÇÃO
UNIVERSIDADE FEDERAL DO RIO GRANDE DO SUL
PROGRAMA DE PÓS-GRADUAÇÃO EM ENGENHARIA MECÂNICA

CONTINUUM DAMAGE EVALUATION AND HOMOGENIZATION PROCESS IN QUASI-FRAGILE MATERIALS SIMULATED USING A LATTICE DISCRETE ELEMENT METHOD

por

Gustavo Giordani

Dissertação para obtenção do Título de
Mestre em Engenharia

Porto Alegre, Março de 2020

CONTINUUM DAMAGE EVALUATION AND HOMOGENIZATION PROCESS IN QUASI-FRAGILE MATERIALS SIMULATED USING A LATTICE DISCRETE ELEMENT METHOD

por

Gustavo Giordani
Engenheiro Mecânico

Dissertação submetida ao Corpo Docente do Programa de Pós-Graduação de Engenharia Mecânica, PROMEC, da Escola de Engenharia da Universidade Federal do Rio Grande do Sul, como parte dos requisitos necessários para a obtenção do Título de

Mestre em Engenharia

Área de Concentração: Mecânica dos Sólidos

Orientador: Prof. Dr. Ignacio Iturrioz

Aprovada por:

Prof. Dr. Jakson Manfredini Vassoler..... PROMEC/UFRGS
Prof. Dr. Eduardo Bittencourt..... PPGEC/UFRGS
Prof. Dr. Luis Eduardo Kosteski…… UNIPAMPA

Prof. Dr. Fernando Marcelo Pereira
Coordenador do PROMEC

Porto Alegre,12 de Março de 2020

"... if you're doing an experiment, you should report everything that you think might make it invalid – not only what you think is right about it…details that could throw doubt on your interpretation must be given, if you know them… the idea is to try to give all of the information to help the others to judge the value of your contribution; not only the information that leads to judgement in one particular direction or another…"

"… you must not fool yourself – and you are the easiest person to fool. So, you have to be very careful about that. After you've not fooled yourself, it's easy not to fool others…"

Surely You're Joking Mr. Feynman!
Richard P. Feynman

ACKNOWLEDGMENTS

O processo de desenvolvimento e a ampliação de horizontes não podem ser atingidos de forma individual e dissociada de um grupo de indivíduos únicos e colaborativos. Desde sempre, imprescindíveis à minha educação, devo agradecer ao meu Irmão, Tiago Giordani, minha Mãe, Milede Possamai Giordani e ao meu Pai, Enuc Giordani pelos esforços e pelo encorajamento em seguir um caminho singular de formação.

Agradeço aos inumeráveis colegas de empresa e amigos próximos que me apoiaram na decisão de traçar novos caminhos e buscar novos conhecimentos dentro do ambiente acadêmico.

Em especial agradeço, a minha namorada Sasithorn que, apesar da distância, me apoiou e me encorajou nos momentos altos e baixos nesta singular etapa da minha formação.

Por fim, o apoio da instituição UFRGS e do Grupo de Mecânica Aplicada (GMAP) foram fundamentais para que este trabalho fosse realizado. Agradecimentos de forma distinta ao professor Ignácio Iturrioz, pelo compromisso e dedicação que demonstrou em transmitir motivação e conhecimento sem medir esforços durante estes últimos anos.

RESUMO

Conhecer, predizer e modificar como estruturas atingem o colapso é um desafio para a engenharia e também uma chave tecnológica no desenvolvimento de estruturas. Entre os materiais utilizados, aqueles que possuem comportamento dúctil, como é o caso de metais, apresentam um processo de dano que é estudado dentro da teoria da plasticidade, permitindo manter a hipótese dos meios contínuos até determinado grau de deterioração. No caso de matérias quasi-frágeis, como é o caso de cerâmicos, alguns tipos de rochas e concreto, a hipótese de modelos utilizados em materiais dúcteis é no mínimo discutível quando o nível de dano está em elevados patamares, havendo neste caso fenômenos particulares, como a localização, a iteração entre clusters de microfissuras e o efeito de escala, entre outros. É de interesse relacionar os resultados obtidos dentro do âmbito da mecânica do contínuo com teorias que preveem um conjunto de descontinuidades que podem crescer e interagir. Notavelmente, métodos alternativos baseados na mecânica do descontínuo tem apresentado resultados promissores. Neste cenário, o domínio é representado por nós vinculados entre si por funções de interação baseados em campos de forças. Estes métodos permitem incorporar naturalmente o dano e/ou a fratura. Na presente dissertação, uma versão do método dos elementos discretos é aplicada primeiramente para simular campos descontínuos que tem solução analítica conhecida dentro da mecânica do contínuo. Os parâmetros convencionalmente empregados na mecânica do contínuo e os conceitos de micromecânica são empregados para permitir comparações entre a solução analítica (mecânica do contínuo) e a extraída numericamente (modelo discreto). O efeito da mudança do número de trincas e de seus respectivos tamanhos é também estudada. Numa segunda aplicação, o modelo discreto é submetido a danos progressivos devido a carregamentos cíclicos proporcionais e não-proporcionais, permitindo avaliar como as propriedades mecânicas se degeneram ao longo do tempo. Por fim, é feito um estudo mostrando o efeito da subdivisão do domínio discreto, observando-se o erro associado ao se realizar este tipo de procedimento. Diversas observações feitas durante o trabalho permitem verificar não só a validade da metodologia, mas também interpretar os resultados obtidos dentro de cada teoria.

Palavras chave: Método dos elementos discretos; Mecânica do dano; Mecânica da fratura; Processo de homogeneização; Carregamento não-proporcional.

ABSTRACT

Knowing, predicting and modifying how the structure reaches the collapse is an engineering challenge and also a technological key for the development of structures. Among the materials, those with ductile behavior, as metals, are evaluated considering the damage process within the plasticity theory framework and, in this case, the hypothesis of a continuum medium is accepted up to a certain degree of deterioration. For quasi-fragile materials, such as ceramics, some types of ground stones and concrete, the hypothesis applied in ductile materials models is, at the very least, questionable when the damage level is high. In this situation, singular phenomena like the localization, interaction between the microcracks clusters, scale effect, among others, can happen. It is of interest to relate continuum mechanics results with theories that allow the material to present a set of interactive and growing discontinuities. Notably, the application of methods based on discontinuous mechanics has presented promising results. In this scenario, the domain is represented by nodes bounded with each other through interacting functions based on field forces. These methods permit to incorporate the damage and/or the fracture naturally. Firstly, in the present dissertation, a version of the discrete element method is applied to simulate discontinuous fields with a known analytical solution in the context of the continuum damage mechanics. The parameters conventionally applied in continuum mechanics and the concepts of micromechanics are incorporated to allow comparisons between the known analytical (continuum mechanics) and the extracted numerical approach (discrete model). The effect caused by the number of cracks and their corresponding sizes is also studied. In the second application, the discrete model is submitted to progressive damage due to proportional and nonproportional cyclic loading, allowing to discuss and evaluate how the material properties degenerate over time. Lastly, a scenario showing the effect of the domain's subdivision is made to visualize the associated error while performing this type of analysis. Many observations made during this work permit to verify not only the validity of the methodology but also to interpret the obtained results in the frameworks of the continuous damage mechanics and fracture/damage mechanics.

Keywords: Lattice discrete element method (LDEM); Damage mechanics; Fracture mechanics; Homogenization process; Nonproportional load.

TABLE OF CONTENTS

LIST OF FIGURES

LIST OF TABLES

LIST OF ABBREVIATIONS

APDL	Ansys parametric design
ASTM	American society for testing material
CDM	Continuum damage mechanics
COD	Crack opening displacement
C. Vol.	Control Volume
CV	Coefficient of variance
DEM	Discrete element method
LDEM	Lattice discrete element method
LSM	Level set method
DD: Σ	Solution for the dilute method applying a macrostress
DD: E	Solution for the dilute method applying a macrostrain
FEA	Finite element analysis
FMM	Fast marching method
GSR	Global sharing rule
LEFM	Linear elastic fracture mechanics
MMVP	Method for multiscale virtual power
MSAT	Matlab ® seismic anisotropy toolkit
PSN	Plane strain state
PSS	Plane stress state
RVE	Representative volume element
SC	Self-consistent approach
S. S. Y	Small-scale yielding
X − FEM	Extended finite element method

LIST OF SYMBOLS

Latin Symbols

A	Overall area, m^2
a	Crack size, m
a_c	Critical crack size, m
A^d	Damaged area, m^2
A_d	Diagonal area of the Dem model's cubic cell, m^2
A_{eff}	Effective area, m^2
a_{eff}	Effective crack size length. m
A^f	Equivalent fracture area, m^2
A_I, B_I	Influence tensor
A_n	Normal area of the DEM model's cubic cel, m^2
C	Stiffness tensor or one of its terms
C^*	Effective of averaged stiffness tensor or one of its terms
$C(x)$	Resultant tensor for the whole body according to position
C_a	Scale factor for the relation between the frac. Energy DEM x Continuum
C_{sec}^{eff}	Effective secant modulus
C_o	Stiffness tensor or one of its terms for the matrix material
c_n	Volume or area fraction of the material n
$CV(G_c)$	Coefficient of variation for G_c
D	Dimension of the macroscale
d	The dimension of the lateral of a cubic cell, m
$\dot{D}$	Damage rate
D_c	Critical damage value
D^d	Damage factor or damage tensor
D_{RVE}	Macro dimension of the representative volume the representative volume
E'	Young's modulus in plane strain or plane stress state
$\overline{E}^{d(SC)}$	Average Young's modulus for the self-consistent method
E_o	In-plane Young's modulus calculated analytically ca

F	Force, N
f	Crack size parameter
$\mathrm{f_{crit}}$	Critical damage density
$\mathrm{f_d}$	Damage density
$F(\mathrm{G_c})$	Probability function for $\mathrm{G_c}$
$\mathrm{f_i}$	Force in individual links , N
$\mathrm{f_{rup}}$	Rupture strength of the bonding links , N
$\mathrm{f_t}$	Tensile strength
$f(\mathrm{x})$	Distribution of forces at the boundaries
G	Shear modulus or energy release rate (see context)
$\mathrm{G^*}$	Effective shear modulus
$\mathrm{G_c}$	Critical energy release rate, $\mathrm{J/m^2}$
$\overline{\mathrm{G}}_\mathrm{c}$	Average value for the energy release rate distribution
$\overline{\mathrm{G}}^{\mathrm{d(SC)}}$	Average shear modulus for the self-consistent method
$\mathrm{G_o}$	Shear modulus calculated analytically for an undamaged structure
$H(\mathrm{x})$	Heaviside step function over the length x
$\mathrm{H^d}$	Compliance damage tensor
$\mathrm{H^{d(SC)}}$	Compliance damage tensor for the self-consistent method
$\mathrm{I_{ijkl}}$	Identity fourth order tensor components
J	Integral J, $\mathrm{J/m^2}$
$K, \mathrm{K_c}$	Stress intensity factor, Critical stress intensity factor $\mathrm{Pa}\sqrt{\mathrm{m}}$
$\mathrm{K_{eff}}$	Effective stress intensity factor $\mathrm{Pa}\sqrt{\mathrm{m}}$
K_{sec}^{eff}	Secant stiffness
k	Bulk modulus
L	Length of the size of the cubic cell, , m
$\mathrm{L_{BL}}$	Lateral dimension suuming all the cubic cells, m
$< \mathrm{M} >$	Notation for the average field over the domain
N	Number of uniaxial bars or number of cubic cells
$\vec{\mathrm{n}}$	Normal vector to a plane
$\mathrm{N_f}$	Density of cracks inside the domain
$\mathrm{N}(\vec{X})$	Norm of the vector $\vec{X}$
$p(\mathrm{f_{rup}})$	Probability function for the rupture strength

R	Material resistance to crack extension , $\mathrm{J/m^2}$
r	Radius from the crack tip, , m
$\mathrm{R_{ff}}$	Failure factor
$\mathrm{r_p}$	Radius of the plastic zone, m
$\mathrm{r_y}$	First order radius for the plastic zone correction, , m
$\mathrm{R_v}$	Triaxiality function
$R(\mathrm{x})$	Bond thermodynamic force distribution
S	Compliance tensor or one of its terms
s	Factor to define the damage evolution law
$\mathrm{S^e}$	Eshelby tensor or one of its terms
$\mathrm{U^d}$	Energy released during damage, J
$\mathrm{u_i}$	Displacement vectors at the boundaries
$\mathrm{u^o}$	Constant displacement at the boundaries
$\mathrm{u_y}$	Unilateral displacement at the crack tip, m
$u(\mathrm{x})$	Distribution of displacement at the boundaries
$\overline{\mathrm{u(x)}}$	Displacement perturbation caused by the inhomogeneity
V	Volume, $\mathrm{m^3}$
v	Subvolume of the overall domain, $\mathrm{m^3}$
$v(0^+), \mathrm{v}(0^-)$	The face separation during crack growth, m
W	Strain energy, $\mathrm{J/m^3}$
Y	Energy density release rate, $\mathrm{J/m^3}$
$\mathrm{Y_f}$	Geometry factor for the stress intensity factor evaluation
$\vec{X}$	Vectorial form for the constitutive tensor
1_{ijkl}	Unitary fourth order tensor components

Greek Symbols

β, γ	Parameters for the Weibull distribution
Γ	Fracture energy considering continuum approach , J
Γ_{DEM}	Fracture energy considering DEM approach , J
Δa	Variation or increament of the crack size or length , m
$\Delta \mathrm{t}$	Maximum time increment for dynamic analysis using discrete model , s
δ	Crack opening displacement, COD

$\hat{\delta}(x)$	Prescribed displacement at the borders, m
$\partial\varepsilon^{avg}$	Increment of an average strain
$\partial\sigma^{avg}$	Increment of an average stress
$\partial\Omega_o$	Boundaries of the domain
ε^{BC}	Strain at the boundaries
ε_c	Crack strain tensor
ε^{dev}	Deviatoric strain tensor or one of its terms
ε^{e}	Elastic strain
ε^{H}	Hydrostatic strain tensor or one of its terms
$\varepsilon^{o}, \varepsilon_o$	Constant strain state at the boundaries
$\dot{\varepsilon_p}$	Plastic strain rate
ε_r	Fracture strain
ε^{t}	Eigenstrain
$\overline{\varepsilon(x)}$	Strain perturbation caused by the inhomogeneity
ζ	Components of a constant strain or stress fields applied at the boundaries
θ	Angular position according to an origin and cylindrical coordinates, rad
κ^*	Effective bulk modulus
$\bar{\kappa}^{d(SC)}$	Average bulk modulus for the self-consistent method
κ_r	Ratio between ε_r and ε_p
λ	Lamé's first parameter
ϑ	Poisson's ratio
$\bar{\vartheta}^{d(SC)}$	Average Poisson's ratio for the self-consistent method
π	Potential energy, J
ρ	Density, kg/m^3
σ, σ_c	Nominal stress, critical nominal stress, N/m^2
σ^{BC}	Stress at the boundaries, N/m^2
σ^{dev}	Deviatoric stress tensor oro ne of its terms, N/m^2
σ_{Deq}	Damage equivalent stress, N/m^2
σ_{eff}	Effective nominal stress, N/m^2
σ_{Gc}	Standard deviation for the average release rate distribution, N/m^2
σ^{H}	Hydrostatic stress tensor or one of its components, N/m^2
σ_o, σ^o	Constant stress at the boundaries,, N/m^2

σ_u	Ultimate stress, N/m^2
σ_{vm}	Von mises stress, N/m^2
σ_y	Yield stress, N/m^2
$\overline{\sigma(x)}$	Stress perturbation caused by the inhomogeneity, N/m^2
Ω_o	Domain volume or area
Ω_i	Subdomain I, volume or area

1 INTRODUCTION

The evolution of the damage process in quasi-fragile materials, like ground stones, concrete, ceramic materials, reinforced concretes and other synthetic composites, is an open problem in solid mechanics. The damage that rules the mechanical behavior until the rupture is described as microcracks spread over the body, inducing anisotropy and loss of stiffness. The characteristic effects of this type of material are the localization of macrocracks characterized by clusters of microcracks, the scale effect and the form that the clusters interact with each other. For these types of materials at low levels of damage, it is conceivable to consider the approximations that the homogenization procedure allows. These models are based on Eshelby's proposal, which enables us to compute inhomogeneities, such as oriented or random cracks embedded in a medium.

The discussion developed by Krajcinovic, 1996, dealing with the classical damage methodology is inspiring. He and other authors developed and presented the discrete element method (DEM) as an alternative where the continuum mechanics assumptions are loosened up to a certain point at which the random distribution of properties can be easily incorporated. The discrete element models based on mass particles that interact by field functions, such as the one developed by Silling et al., 2007, is one of the alternatives. Another branch of research involves defining the interaction between the elements applying links that establish a regular or a non-regular structure. The latter method is hereon called the Lattice Discrete Element Method (LDEM), where the solid is characterized by an interconnected web of uniaxial elements with the masses located at the nodes.

1.1 Overview and Purpose

The present work will initially introduce concepts related to continuum damage mechanics, fracture mechanics, micromechanics concepts and homogenization techniques to serve as a base to describe the method that incorporates the LDEM approach into a continuum mechanical description. Therefore, a procedure for the extraction of mechanical properties defined by a representative lattice structure is developed.

The purpose of the developed technique is to enable the Analyst of an LDEM structure to visualize the loss of stiffness of a specific domain that undergoes a damaging process.

Therefore, characteristic features, as the changes of the representative constitutive tensor, can be evaluated for a given time-dependent LDEM analysis. It is important to emphasize that the study does not generate damage. It is a method that assesses how the mechanical properties of a given structure degenerate in a specific moment of a cumulative damage process.

1.2 Main Goals

Global Goal:

- Explore the capacity of the version of the lattice discrete element method (LDEM) in simulating the damage process in quasi-fragile materials through the application of damage mechanics concepts.

Specific Goals:

- Verify the LDEM ability to represent the analytical solutions found in the classical micromechanical approach using a finite element procedure.
- Suggest a methodology to evaluate the effective properties at different stages of an increasing damage process for an LDEM structure.
- Implement a method to define an appropriate representative volume element (RVE) of a discrete model (see Section 2.3.1 for the RVE definition).
- Describe comparative solutions between “open” and “closed” cracks avoiding complicated conjectures of damage mechanics.

The work focuses on applying the homogenization procedure defined by micromechanics concepts to evaluate damage in a specific type of discrete model. Scripts developed in Matlab ® and Ansys APDL ® are used to investigate the damage process and to establish new constitutive tensors as the damage evolves. In other words, the goal is to relate the loss of strength of uniaxial elements in a lattice structure with the modifications occurring in the continuum mechanics properties.

1.3 Organization of the Dissertation

Figure 1.1 presents the Chapters and Sections that constitute this work. The main sections regarding the theoretical background are highlighted in **bold.** The remaining bibliographical review is used as a support for the reader not acquainted with the main subjects here discussed.

After the theoretical background composed of six Sections (Chapter 2), the Development (Chapter 3) displays the workflow in detail covering the Methodology, Results and the Appendices. An overview of the state-of-the-art in Discrete Models is set apart in Chapter 2.7, highlighting different approaches that have been researched lately. The reader can find in the last part of this work (Appendix F) the adapted version of the paper based on the primary results discussed.

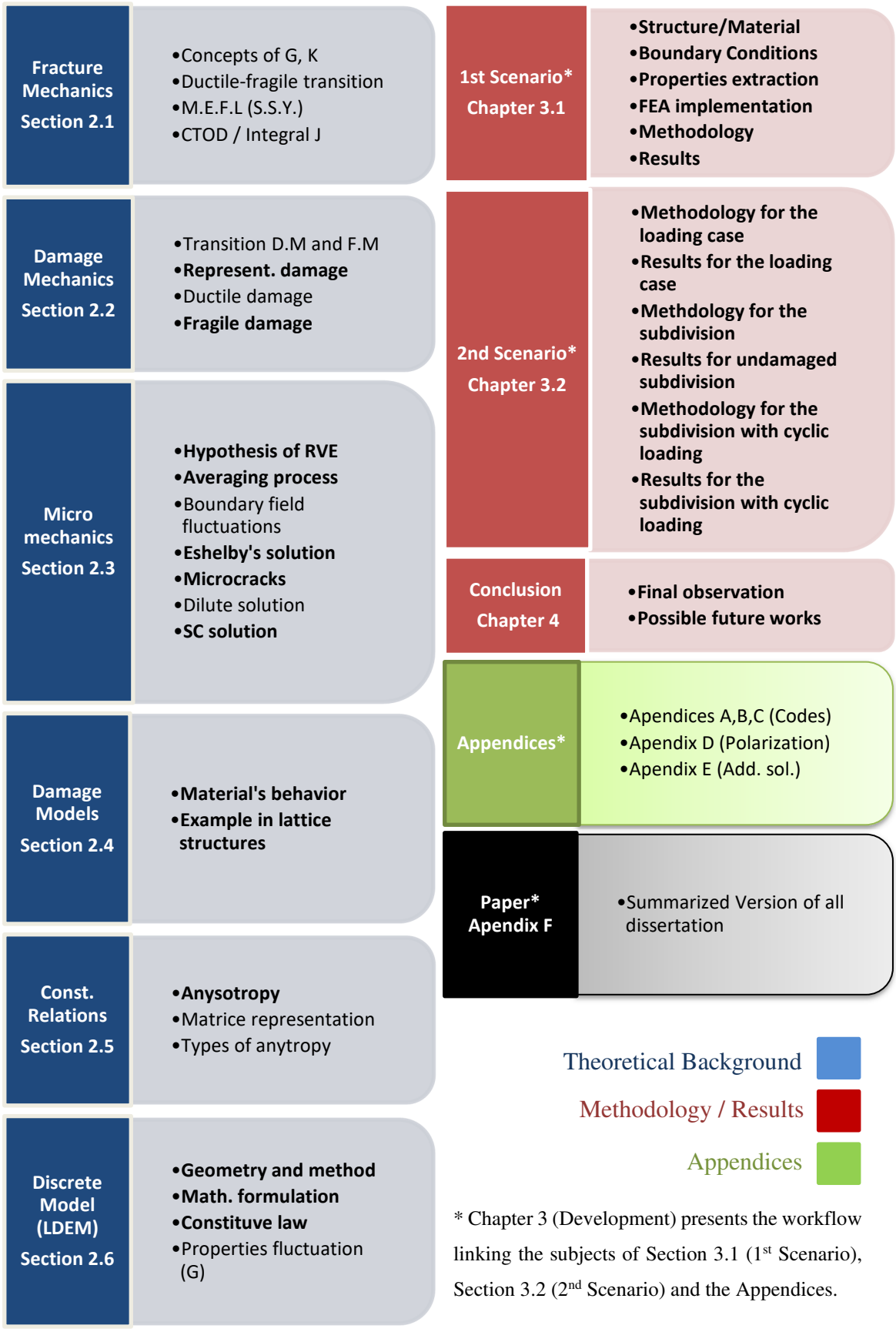

Figure 1.1 - Macro organization of the work defining the Chapters/Sections with theoretical background, methodology/results and appendices.

2 BIBLIOGRAPHICAL AND THEORETICAL REVIEW

The following sections will address different aspects of the damage, fracture and micromechanics, considering the basic and most essential concepts for the conception of the present work. Initially, Section 2.1 introduces the basic ideas of energy release rate and fracture toughness (G and K). Also, a short overview about Integral J and Crack Opening Displacement (COD) is offered with the discussion of stable and unstable cracks as an R-resistance curve dependency. Section 2.2 discusses the basic features of continuum damage mechanics (CDM), introducing the damage parameter in the elastic and plastic situations. Section 2.3.1 is added separately due to the importance of establishing a definition for the Representative Volume Element (RVE) within the micromechanics studies. Section 2.3.2 and 2.3.3 show how the material properties and fields can be averaged over the domain, introducing the micromechanics concepts later applied to the Eshelby solution in Section 2.3.4. Section 2.4 discusses lattice structures utilized to evaluate damage in brittle and quasi-brittle materials, focusing mainly on the profuse works of Krajcinovic, while Section 2.5 describes the concepts of anisotropy. Section 2.6.1 displays the specific discrete model that will be applied in this work and Section 2.7 discusses current works that apply different approaches to the domain of discrete methods.

2.1 Fracture Mechanics Concepts

The continuum mechanics establishes the concepts of stress and strain in a tensor form. This interpretation allows the characterization of each point in a body describing the strain/stress state in every direction. The transformation and rearrangement of these entities yield single values that can be compared to some standard value later. The maximum distortion energy criterion uses, e.g., the second deviatoric stress invariant to generate a value and correlate it with a material subjected to uniaxial tests. This well-established systematic succeeded at continuous, homogenous and undamaged structures. By the end of the XIX century and the beginning of the XX century, proposals such as Inglis, 1913, calculated the stress distribution in a plate when an inserted elliptical defect distorts a constant stress field. Nevertheless, when the ellipse stretches up to a point where the geometry becomes a macroscopic line, the stresses at both vertices tend to infinity. That is the moment when the classical continuum mechanics fails to evaluate the real-world observations. Alongside this, the engineering materials are never homogenous and continuous. Therefore, the fracture mechanics theory came to introduce new tools to deal with these unsolved scenarios.

Griffith, 1920, considering the state of equilibrium established by the minimum potential energy theorem, defined a new approach for the rupture phenomenon. He stated in his classical work: “if the equilibrium is possible, must be one in which rupture of the solid has occurred if the system can pass from the unbroken to the broken condition by a process involving a continuous decrease in potential energy.” To find the breaking load of real solids, “it is necessary to account of the increase in potential energy which occurs in the formation of new surfaces in the interior of such solid.”

This statement defines that the energy available for crack growth must overcome the material resistance, which includes surface energy, plastic work and other forms of dissipation. Griffith’s energy release rate G is introduced as the change rate in the potential energy π with the crack area. The moment of fracture is then defined when G approaches a critical value G_c. The most classical representation is described as in Equation 2.1, where it establishes the relation among G, crack size $2a$, Elastic Modulus E and a remotely applied uniaxial stress σ for an infinite and thin plate.

$$G = \frac{\pi \cdot \sigma^2 \cdot a}{E} \tag{2.1}$$

The critical resistance to fracture G_c occurs when a combination of critical stress σ_c and a critical crack size a_c is reached. The basic assumptions of this approach are that the energy release rate does not consider the specimen size or geometry and also that it can be applied predominantly for linear elastic bodies.

Irwin, 1957, introduces another form of considering the local crack analysis. A field is used to describe the stress state in the vicinity of a hypothetical crack tip, as represented by Equation 2.2. This field is a function of the angular position θ, radius from the crack tip r and the stress intensity factor K. Additionally, the boundary conditions defined by the load configuration of one or a combination of the three fracture modes presented in Figure 2.1c will also have influence. In general, the load scenario is a linear superposition of mode I and mode II for planar cases. In three dimensional cases, the mode III is added to the two previous ones.

Equation 2.2, along with Equation 2.3, demonstrates that the stress at a point approaching the crack tip reaches infinity. The field is controlled by the stress intensity factor K which is typically described by three independent terms and its fracture mode: the imposed stress at the boundary conditions σ, the size of the crack a and the geometry factor Y_f. The geometry factor

Y_f can be easily found for simple cases in handbooks of stress analysis or can be stipulated for complex geometries using Finite Element Analysis (FEA).

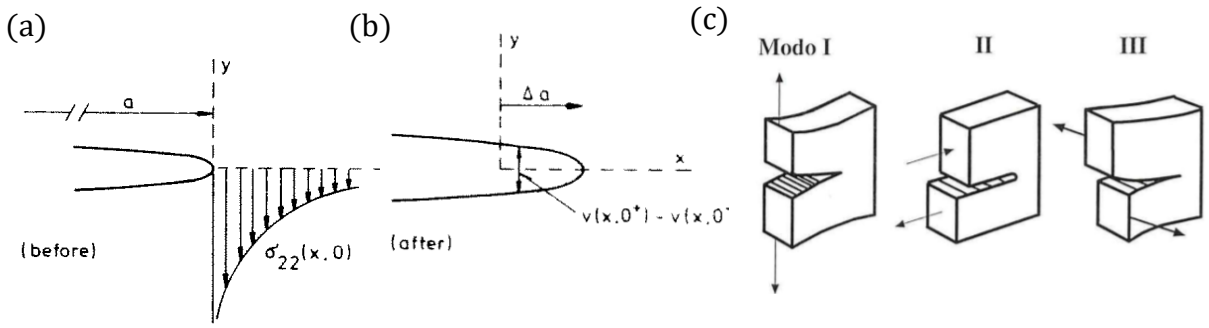

Figure 2.1 - (a) The stress profile close to the crack tip with size a. (b) the crack growth causes new free surfaces Δa [Hutchinson, 1979]. (c) The classical fracture modes [Iturrioz, 1995].

$$\sigma_{ij} = (K_{I,II\ or\ III}) \cdot f_{ij}^{I,II\ or\ III}(\theta) \cdot (2\pi r)^{-\frac{1}{2}} \tag{2.2}$$

$$K_{I,II\ or\ III} = Y_f \cdot \sigma \sqrt{\pi a} \tag{2.3}$$

The stress intensity factor K, as for the energy release rate G, can be compared to a critical value K_C (fracture toughness) to establish the crack propagation. Despite the different approaches for K and G, it is possible to derive a relationship between the two entities. For example, considering mode I, Figure 2.1a and b presents the description from Equation 2.4 for the stresses in the y-direction σ_{22} during the crack opening Δa.

$$\sigma_{22} = \frac{K_I(a)}{\sqrt{2\pi r}} \quad for\ \ 0 < a \leq \Delta a \tag{2.4}$$

The energy release rate G is the negative work done by the traction σ_{22} which integrating over the crack opening leads to Equation 2.5, where the term $[v(0^+) - v(0^-)]$ is related to the crack faces' separation.

$$G = -\frac{\partial \pi(a)}{\partial a} = \frac{1}{2 \cdot \Delta a} \int_0^{\Delta a} \sigma_{22} \cdot [v(0^+) - v(0^-)]\ dx \tag{2.5}$$

The combination of both Equations brings to a solution for plane strain and plane stress (Equation 2.6). For three-dimensional bodies, Rice et al., 1971 derived one solution for G as a linear combination of the three modes (Equation 2.7).

$$G = \frac{1-\vartheta^2}{E} \cdot {K_I}^2 \quad (plane\ strain) \quad G = \frac{{K_I}^2}{E} \quad (plane\ stress) \tag{2.6}$$

$$G = \frac{1-\vartheta^2}{E} \cdot \left({K_I}^2 + {K_{II}}^2\right) + \frac{1}{2G_{shear}} \cdot {K_{III}}^2 \qquad (3-D) \tag{2.7}$$

The use of G and K pursuits to avoid the intrinsic problems caused by plastification at the vicinity of the crack tip when any load is applied. However, the plastification zone must be small enough to be still able to use the Linear Elastic Fracture Mechanics (LEFM). When the toughness of the material is considerably high and the plastic zone is large, the employment of Nonlinear Fracture Mechanics must be considered. The use of LEFM can be defined using the concept of Small-Scale Yielding (S.S.Y). Roughly speaking, in most instances, S.S.Y seems to be reasonable as long as the applied load is below one half of the plasticity load [Hutchinson, 1979]. For this consideration, the characteristic length (crack length or uncracked ligament) must be much larger than the plastic zone length. However, except under brittle condition like glasses and rocks, the observed G_c is several orders of magnitude higher than the calculated.

Despite G and K being equivalent, the application of K is more convenient and it was also extended to large scale yielding in the last decades. It is also essential to clarify that the stress fracture toughness (K_c) varies widely with temperature leading to brittle-ductile transition. Also, different responses will be achieved with thin sheets (plane stress) or thick blocks (plane strain). Figure 2.2 shows the changes in K_C according to the thickness and temperature. Except for thin foils/sheets, the fracture toughness is defined as a plane strain condition, i.e., the lowest critical value for thicker samples. The recorded measurements are usually determined by the K_C tests standards (ASTM test – Fracture toughness testing method).

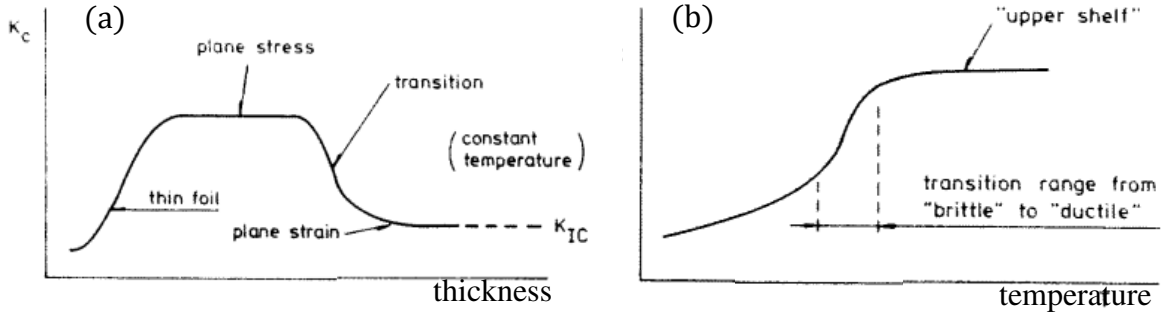

Figure 2.2 - (a) K_c changes are owing to the plate thickness. (b) K_c changes are owing to temperature changes [Hutchinson, 1979].

When the linear behavior no longer prevails, the nonlinear fracture mechanics, which includes Elastic-plastic, viscoelastic and viscoplastic fracture, will drive the solution approach. As the material toughness increases, the Linear Elastic Fracture Mechanics (LEFM) collapses and the failure mode is governed by flow properties. The two main criteria used in these cases are the crack tip opening displacement (COD) and the Integral J.

Wells, 1961, studying structural steels, demonstrated that these materials are too tough to consider the use of Linear Elastic Fracture Mechanics. His studies have shown that the crack tip normally blunted due to plastic deformation avoiding the propagation of the discontinuity [Anderson, 1994]. Along with Irwin's work, related to small plasticity at the vicinity of the crack tip, Wells proposed a correlation between the stress intensity factor and the Crack Opening Displacement assuming an effective crack length equal to $a + r_y$, where r_y is the first order plastic zone approximation. Assuming no strain hardening and a plane stress state, Irwin's approach brings to a relation between r_y, stress intensity factor K_I and the yielding stress σ_y as presented in Equation 2.8. As a result, an effective stress intensity factor K_{eff} will be defined due to the longer effective crack length a_{eff}. Figure 2.3b shows the correction and the stress distribution due to the plastic zone r_p. r_y is defined as half of the r_p value (Figure 2.3c).

Using Equation 2.8 and considering the LEFM formulation [see Branco, 1986], it is possible to find the Crack-tip Opening Displacement δ directly and relate it to the stress intensity factor and energy release rate. Equation 2.9 is an example in the plane stress state of how the COD method can be used as a parameter to characterize the crack tip evolution.

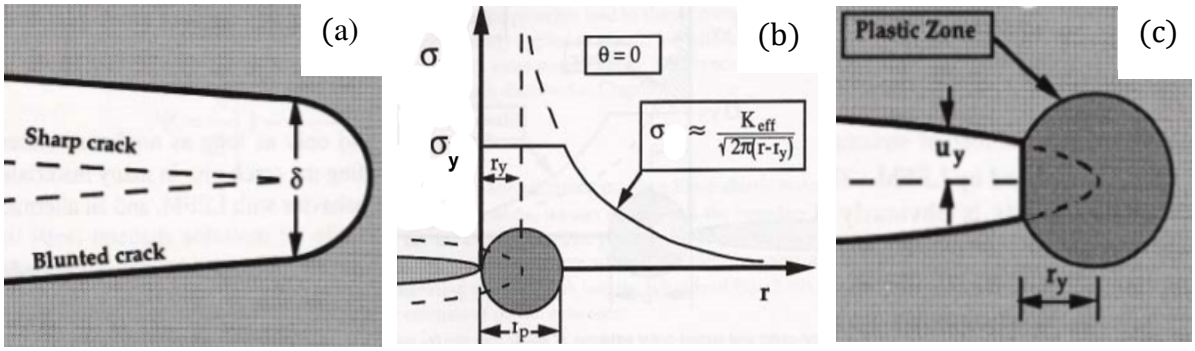

Figure 2.3 - (a) Crack Opening Displacement δ. The crack blunts resulting in a finite displacement. (b) Irwin plasticity correction. An effective stress intensity factor is resultant from an increased effective crack length caused by the factor r_y. (c) unilateral displacement considering the plastic region r_y.[Anderson, 1994]

$$r_y = \frac{1}{2\pi}\left(\frac{K_I}{\sigma_y}\right)^2 \tag{2.8}$$

$$\delta = 2 \cdot u_y = \frac{4}{\pi}\frac{{K_I}^2}{\sigma_y \cdot E} = \frac{4}{\pi}\frac{G}{\sigma_y} \tag{2.9}$$

Conventionally, a three-point bending test is proposed to evaluate indirectly the displacement δ. The procedure can be vastly found in the literature**.**

Integral J is another approach proposed by Rice, 1968. It is similar to Griffith's energy release rate but employed for non-linear elastic materials. Therefore, it can be represented as the potential energy variation due to a growing crack as presented in Equation 2.5 but changing from factor- G to factor- J. Landes and Begley, 1972, measured experimentally J using several specimens of the same size, same material, same geometry, but with different crack lengths. They plotted the load versus displacement, which makes the area below the curve the energy absorbed. The differential of these curves defines the J critical values.

However, the options presented until now are only capable of predicting the crack opening as the factors G, K or J approach a critical value. The stable or unstable crack development is dependent on material resistance to crack extension called factor-R. Therefore, for a specific condition of stress, the relation

$$\frac{dG}{da} > \frac{dR}{da} \quad or \quad \frac{dJ}{da} > \frac{dR}{da} \tag{2.10}$$

must also be fulfilled for unstable growth. For brittle material, the R-curve is usually flatter and for a dominant plastic material is more challenging to obtain the curve due to the size of the yielded region, the complexity of the geometry and the load configuration. Figure 2.4 shows the curves for G and J at the critical point where the unstable condition must occur.

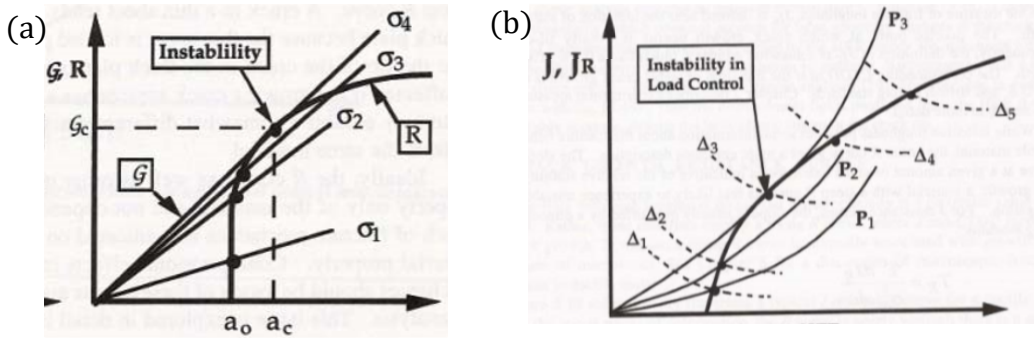

Figure 2.4 - (a) Energy release rate and factor-R curves defining the instability point according to critical crack size a_c. (b) Integral J according to displacement-controlled test Δ_n and a force-controlled test P_n. [Anderson, 1994]

2.2 Continuum Damage Mechanics Concepts

The Continuum Damage Mechanics (CDM) describes the material evolution from an initial undamaged scenario until a state of macrocracks initiation. The concepts were first introduced by Kachanov, 1958, when studying the creep evolution and its relation with fracture. Both fracture and damage mechanics are concerned with the behavior of the damaged medium to address the safety of a particular structure. However, in CDM, the defect is treated on a microscale and they are continuously distributed throughout the material. The macro properties such as strength and toughness are dependent on the micro effects caused by voids, discontinuities, micro-cavities and/or defects. On the other hand, the fracture mechanics considers the cracks tip singularity and its impact locally. Figure 2.5 shows a diagram that clarifies these two fields subdivision [Zhang, 1995].

"The ultimate goal of damage mechanics is to represent a discontinuous state by a continuous variable" [Lemaitre and Dufailly, 1987].

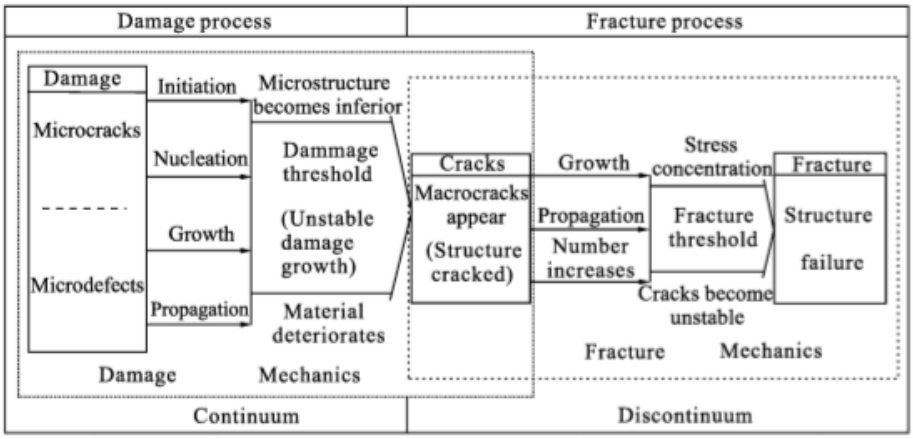

Figure 2.5 - The subjects defined normally as belonging to damage and fracture mechanics. [Zhang, 1995]

The purest form of mathematically representing a damaged body using the concepts of RVE is considering a normal plane $\vec{n}$, an overall area A and the decreasing resistance according to the damaged area A^d (Figure 2.6). The relation between the effective area A_{eff} and the total area A results in a scalar damage value D^d.

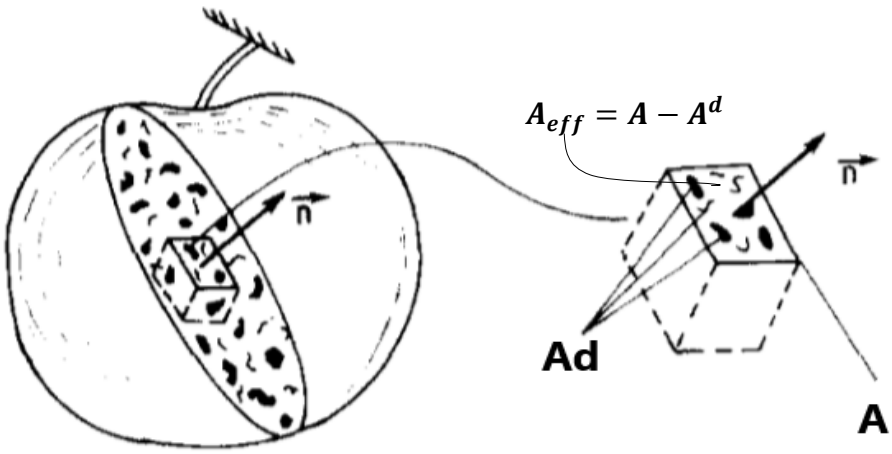

Figure 2.6 – Damaged element considering the reduction of the effective resistance area due to the presence of cracks and voids. [Lemaitre, 1984]

In the cases where D^d is a function of the orientation of the plane $\vec{n}$, the entity evolves into a tensorial form. When the value of D^d is invariant to $\vec{n}$, the damage is called isotropic, which means cracks and cavities are equally distributed in all directions. Equation 2.11 relates the usual engineering stress σ with the damage factor, introducing the concept of effective stress σ_{eff} owing to the decreasing area.

$$D^d = \frac{A - A^d}{A} = \frac{A_{eff}}{A}, \qquad \sigma_{eff} = \frac{\sigma}{1 - D^d} \tag{2.11}$$

The strain equivalence principle by Lemaitre, 1971 [apud Lerma et al., 2018] establishes that the constitutive formulation of any damaged material is attained as those for a virgin material, which means substituting the stress with the effective stress. For an elastic material and a uniaxial case, the relation in Equation 2.12 will conduct to the definition of an effective Young Modulus E_{eff} and into a direct relationship of damage and elastic strain ε^e.

$$\varepsilon^e = \frac{\sigma_{eff}}{E} = \frac{\sigma}{E(1 - D^d)}, \qquad E_{eff} = E(1 - D^d) \tag{2.12}$$

As an example of damage evolution, Figure 2.7 shows the uniaxial test of a ductile steel. In Figure 2.7a, the necking process changes the actual transversal area. The progressing damage alters E_{eff} according to Figure 2.7b up until the rupture stress σ_r. Figure 2.7c is the representation of the damage evolution term from the ultimate stress σ_u until rupture. For metals, normally the critical $D^d{}_c$ is between 0.2 and 0.8 [Lemaitre, 1984].

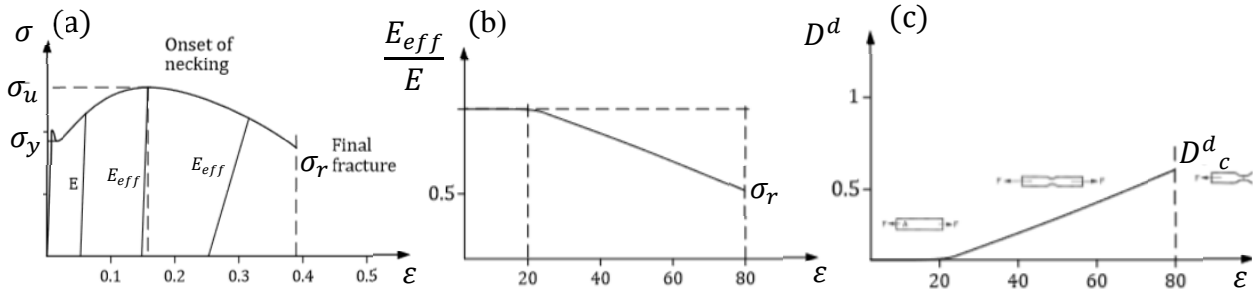

Figure 2.7 - (a) The uniaxial traction test in ductile material presenting the changes in E. (b) The relation between E_{eff} and E. (c) The damage evolution from the ultimate stress σ_u on due to the necking process. [Lerma et al., 2018]

For brittle materials, as the necking does not occur, the discussed concept would not lead to a damaging process, nevertheless, in the following sections, a different approach will be presented to evaluate damage in fragile materials.

Further development of CDM considers the introduction of the energy density release rate Y, which is related to the strain energy W ($\partial W = \sigma \partial \varepsilon$). Under uniaxial/linear case and

considering the equivalence principle for damaged materials, Equation 2.13 presents the simplest example of these entities.

$$W = \frac{1}{2}\sigma \cdot \varepsilon = \frac{1}{2}\frac{\sigma^2}{E(1-D^d)}\,, \qquad \frac{\partial W}{\partial D^d} = -\frac{W}{1-D^d} = -Y \tag{2.13}$$

This Equation represents the reduction that the damage causes at the elastic strain energy density W. This reduction is defined as the density release rate Y.

When the linear isotropic elasticity is coupled with damage directly, a tensor form can also be defined. The damage, in this section, will be kept as a scalar D^d (isotropic damage) despite the possibility to define a tensor D^d_{ijkl} for anisotropic damage. The three-dimensional development using linear elastic equations will result in a Damage Equivalent Stress Criterion. The damage mechanism is influenced by energy density W, which can be defined as the deviatoric components of stress (${\sigma_{ij}}^{dev}$) and strain (${\varepsilon_{ij}}^{dev}$) and another part as the hydrostatic component of stress (σ^h) and strain (ε^h), as shown in Equation 2.15.

$$\sigma_{ij} = C_{ijkl}\varepsilon^e_{kl}(1-D^d), \qquad \varepsilon^e_{ij} = \frac{1+\vartheta}{E(1-D^d)}\sigma_{ij} - \frac{\vartheta}{E(1-D^d)}\sigma_{kk}\delta_{ij} \tag{2.14}$$

$$W = \int \sigma_{ij}\, d\varepsilon^e_{ij} = \int {\sigma_{ij}}^{dev}\, d{\varepsilon_{ij}}^{dev} + \delta_{ij}\delta_{ij}\int \sigma^h\, d\varepsilon^h \tag{2.15}$$

The coupled damage relation also defines that

$${\sigma_{ij}}^{dev} = \frac{E(1-D^d)}{1+\vartheta}\cdot {\varepsilon_{ij}}^{dev} \qquad and \qquad \sigma^h = \frac{E(1-D^d)}{1-2\vartheta}\cdot \varepsilon^h \tag{2.16}$$

which substituting Equation 2.16 into Equation 2.15 yields

$$W = \frac{{\sigma_{vm}}^2}{2E(1-D^d)}\cdot\left[\frac{2}{3}(1+\vartheta) + 3(1-2\vartheta)\left(\frac{\sigma^h}{\sigma_{VM}}\right)^2\right] = \frac{{\sigma_{VM}}^2}{2E(1-D^d)}\cdot R_v \tag{2.17}$$

where the σ_{VM} is the von mises stress and the term R_v is called the triaxiality function related to the hydrostatic contribution. In uniaxial tests, the term R_v is equal to unity bringing back the

formulation to Equation 2.13. The triaxiality function takes into account the hydrostatic stress and its effects on energy density. The presented Equations are a form to relate uniaxial tests with scenarios where the stress state is complicated, generating a tool to diagnose the damage process. It is possible to visualize that, defining a damage equivalent stress σ_{Deq} and comparing Equation 2.17 with Equation 2.13 [Ibijola, 1998]:

$$\sigma_{Deq} = \sigma_{vm} \cdot {R_v}^{1/2} \tag{2.18}$$

The difference between the damage equivalent stress σ_{Deq} and the von mises stress σ_{vm} is the function R_v. It is interesting to note that for brittle materials, there is not a considerable plastic strain and, as the strain is related to the increasing damage, the damage term is null, transforming Equation 2.13 into Equation 2.19. The stress σ_u is the maximum stress before fracture and Y represents the total dissipated energy during fracture.

$$Y = \frac{{\sigma_u}^2}{2 \cdot E} \tag{2.19}$$

Another interesting approach is to consider a relationship between the required energy during crack growth using fracture mechanics and the involved energy in the damaging process of a cubic cell. Considering a brittle material, a cell with a volume d^3 and a crack with size a^2, Lemaitre and Dufailly, 1987 introduced the relation between G_c and Y_c resulting in Expression 2.20. For fragile material, Y is a constant and, therefore, it is already a critical value.

$$D^d = \frac{a^2}{d^2}\frac{G_c}{Y_c \cdot d} = \mathrm{A}_d \cdot \frac{G_c}{Y_c \cdot d^3} \tag{2.20}$$

The value of G_c can be easily found with the knowledge of K_c (books of fracture mechanics) according to Equation 2.6. Y_c can be derived from Equation 2.13 and can be found through uniaxial tests. If we consider a body with size length L_{BL} described as the summation of small cubes of length size d, the damage of the volume is taken as the mean value of the partial damages at each cell. This approach will lead to Equation 2.21.

$$D^d = \frac{G_c}{Y_c \cdot d \cdot {L_{BL}}^2} \sum_{i=1}^{n^o\ of\ cells} {a_i}^2 \tag{2.21}$$

A compelling case is when all the cracks have a length size d and the total damage is equal to unity. Equation 2.21 and Equation 2.20 yields a relation equal to Expression 2.22, where it is easy to observe that the damage is complete when all cells have the crack length the same to d.

$${D^d}_c = \frac{\sum_{i=1}^{n^o\ of\ cells} {a_i}^2}{{L_{BL}}^2} \tag{2.22}$$

An essential factor for the damage analysis, but not discussed in this work, is the configuration of the damage evolution law. The previous Equations ground its assumption considering the damage rate $\dot{D}$ as proportional to the plastic strain rate $\dot{\varepsilon_p}$ and by an energy relation $(Y)^{s=1}$. The s-factor is dependent on the material and temperature in which the test is performed and it can have different values for quasi-brittle, ductile and creep scenarios [Lemaitre and Desmorat, 2001].

2.3 Micromechanics Concepts

2.3.1 Representative Volume Element (RVE) Definition

Any real material is intrinsically heterogeneous at a particular scale, although most of the engineering application entails the existence of continuous and homogeneous materials. It is always a matter of analysis scale. Metals are the most known case where different alloying elements are applied to modify material properties. The assembly of phases, generating the so-called multi-phase materials, can significantly change material properties as, e.g., strength, hardness, stiffness and wear resistance. In the past decades, foams and composites received considerable attention due to functional enhancements in weight and resistance capabilities. Understanding the correlation between micro and macro-scale behavior provides a tool to design the material's microstructure and create possibilities not conceived before.

The simplest form to homogenize a structure composed of two or more materials is considering the volume proportion of each one of the constituents. The properties are, therefore,

based on the average portion and disregard the interactions among the different materials. Eshelby, 1957 established a more sophisticated approach followed by others as Mori and Tanaka, 1973 and Hashin, 1962. The equivalent material properties are, in these cases, analytical solutions for ellipsoidal inclusion and cannot be applied when complex interactions between the materials' interface exist. The primaries and most common hypotheses for homogeneous materials are [Kousznetsova, 2002]:

- The material must be considered sufficiently macroscopically homogeneous.

- The microscopic scale is much larger than the atomic and molecular size to apply continuum mechanics formulation.

- The material morphology can be distinguishable being easily defined by inclusion, cavities, grains, matrix, and so forth.

- There must be an order of magnitude between microscale and macroscale to establish a principle of scale separation.

- An assumed global periodicity of the microstructure with a spatially repeated structure defines a macroscopic specimen. In the case of complex configurations, a local recurrence can be determined (Figure 2.8).

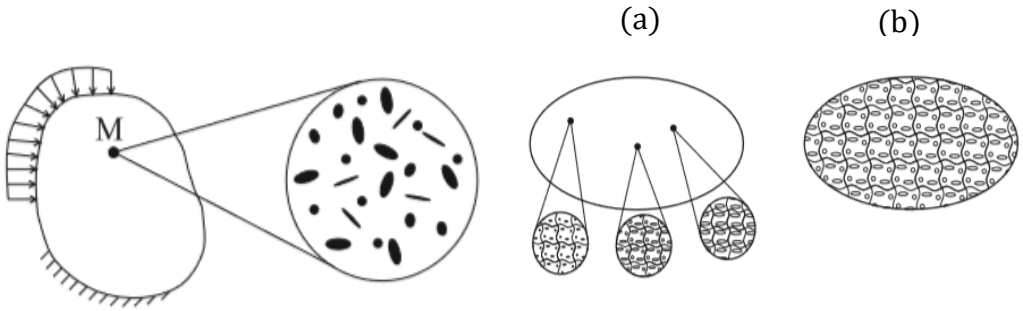

Figure 2.8 - (a) local periodicity of the microstructure which implies different properties in sufficient distance locations. (b) the complete body has the same periodicity. [Kousznetsova, 2002]

The definition of the representative volume is a tricky task. The boundaries must be chosen large enough to represent the microstructure but small enough to evaluate variation in the macro properties. This means that the smallest microstructural volume that represents an overall macroscopic property of interest is the RVE (Figure 2.9).

The RVE is used to obtain the response of a homogenized microscopic continuum in a macroscopic region. Hill, 1963 complements arguing that a well-defined RVE is the one in which the response under uniform displacement and traction boundary conditions coincides.

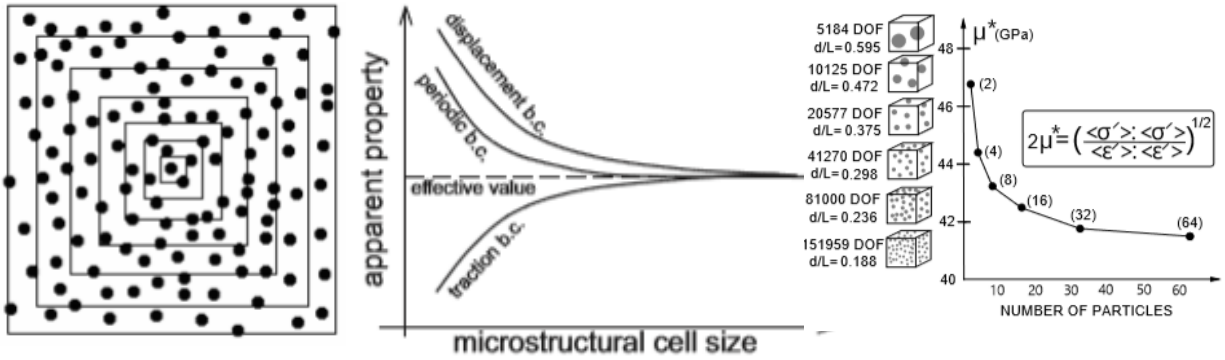

Figure 2.9 - The size of RVE must be large enough to reproduce microscopic effects but large enough to capture macroscopic response variations. [Kousznetsova, 2002]

The continuum mechanics assumes that for a specific point or material neighborhood, the material distribution, strain and stress are necessarily considered uniform (Point P - Figure 2.10). However, on the microscale level, the surrounding area of a specific region is not necessarily continuous and uniform, having possibly various constituents with its shapes and properties. Within the microscale, defects, grain boundaries and inclusions, among other inhomogeneities, can be described. The sum of their characteristics will yield averaged properties at the macro scale. To be representative, as mentioned, the RVE must have a large number of such microheterogeneities where the relation D (macroscale)/d (microscale) >>1 is preserved regardless of the fulfillment of periodicity and randomness.

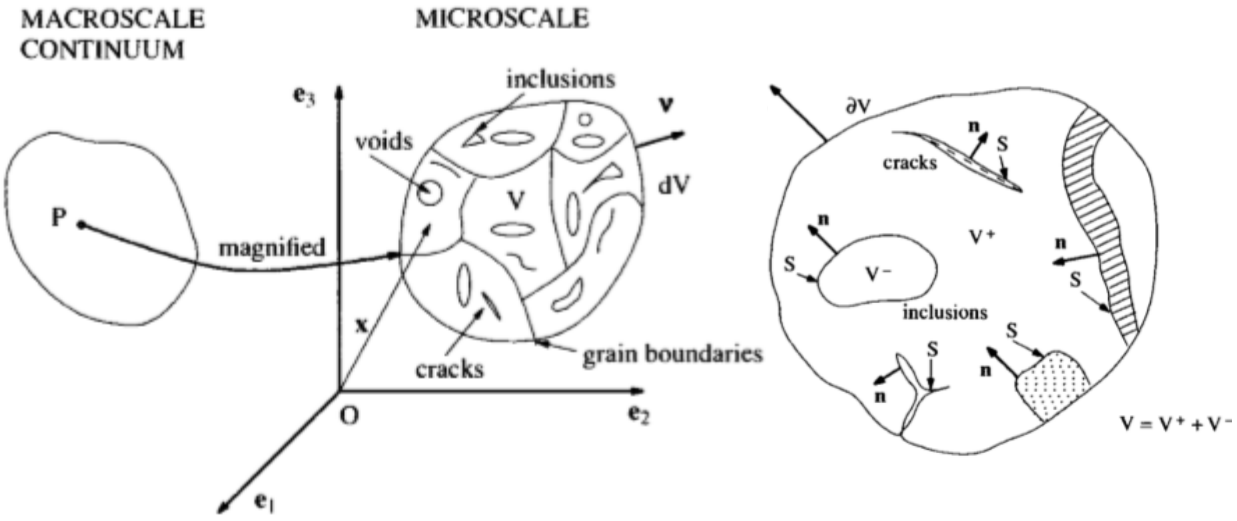

Figure 2.10 - Transition between macroscopic continuum and microscale. At microscale a variety of perturbation as inclusions, cracks and voids are presented. [Nemat-Nasser and Hori, 1999]

The definition of such RVE is complicated and depends on a particular problem and a specific concept. It is one of the most vital decisions the analyst must define.

2.3.2 Hill's Principle

The averaging process used in micromechanics defines averaged quantities that can be applied to represent characteristics of the RVE. The notation <M> can be used as a form to denote an averaged volume of a spatially and integrable quantity. M can represent stress or strain or any other quantity of interest, as defined in Equation 2.23.

$$< M >_{V_{RVE}} = \frac{1}{V_{RVE}} \cdot \int_v M(x)\, \partial v \tag{2.23}$$

In this work, only small-displacement and linear elastic constituents are employed. The RVE is, therefore, established by a direct and dependent relationship between stress σ and strain ε. The increment of average stress, $\delta\sigma^{avg}$ or average strain, $\delta\varepsilon^{avg}$, generates a representative constitutive tensor which represents the RVE's macro mechanical properties based on the micromechanical constituents:

$$\delta\sigma^{avg} = C \;:\; \delta\varepsilon^{avg} \quad \rightarrow \quad \sigma_{ij} = C_{ijkl}\varepsilon_{kl} \tag{2.24}$$

As stated by Zohdi, 2002, "the mission of micro-macro mechanics is to determine relationships between the microstructure and the macroscopic response or 'structural property' of a material, using models on the microscale that are as simple as possible."

For linear elasticity cases, the relationship between averages for the stress and strain fields implies the definition of an effective property C* which is not related to material property, but a mean of computing the correlation between different averaged fields:

$$< \sigma >_{V_{RVE}} = C^* < \varepsilon >_{V_{RVE}} \; or \; < \varepsilon >_{V_{RVE}} = C^{*^{-1}} < \sigma >_{V_{RVE}} \tag{2.25}$$

The first to evaluate the microheterogeneities in a solid form was Voigt in 1892, where he assumed the constant strain field within the RVE leading to an expression for C*. The work

of Reuss, 1929, complemented Voigt's development by defining a continuous stress field. These initial papers, led Hill, 1952 to establish the relationship $(< C^{*^{-1}} >_{V_{Reuss}})^{-1} \leq C^{*} \leq < C^{*} >_{V_{Voigt}}$ which assign Voigt and Reuss as the extreme conditions for any well-established microheterogeneous material. Hill also defined what is called Hill's condition that provides a more precise mathematical formulation for the determination of the Representative Volume Element. The equality $< \sigma : \varepsilon >_{V_{RVE}} = < \sigma >_{V_{RVE}} : < \varepsilon >_{V_{RVE}}$ must be fulfilled when a pure linear displacement or traction is applied at the boundaries. The requirement is defined by a comparison of the strain energy density at the volume in the micro and macroscale. In the event of a nonuniform load applied at the boundaries, a well-defined RVE must be large enough to have small variations compared to its size.

"Our requirement that the sample must be large enough to have relatively small boundary field fluctuations relative to its size and small enough relative to the macroscopic engineering structure, forces us to choose boundary conditions that are uniform. This is not optional" [Zohdi, 2002].

Usually, the homogenization process is achieved applying the solution for the boundary value problem. In a plane state, only three linearly independent boundary conditions are necessary to define all the components of the stiffness or compliance matrix, where ζ is the prescribed strain ε^{BC} or stress σ^{BC} at the boundary surface of the RVE:

$$\varepsilon^{BC} or\ \sigma^{BC} = \begin{pmatrix} \zeta_1 & 0 & 0 \\ 0 & 0 & 0 \\ 0 & 0 & 0 \end{pmatrix}, \begin{pmatrix} 0 & \zeta_{12} & 0 \\ \zeta_{12} & 0 & 0 \\ 0 & 0 & 0 \end{pmatrix} and \begin{pmatrix} 0 & 0 & 0 \\ 0 & \zeta_2 & 0 \\ 0 & 0 & 0 \end{pmatrix} \tag{2.26}$$

From the previous form, three different Equations emerge at each one of the three load conditions. Applying these constant boundary conditions in a presumably micro inhomogeneous isotropic material, the effective bulk k^* and shear moduli G^* can be defined as [Zohdi, 2002]:

$$k^* = \frac{1}{3}\frac{< \sigma_{ij} >_{V_{RVE}}}{< \varepsilon_{ij} >_{V_{RVE}}} \ and \ G^* = \frac{1}{2}\sqrt{\frac{< \sigma_{ij}^{dev} >_{V_{RVE}} : < \sigma_{ij}^{dev} >_{V_{RVE}}}{< \varepsilon_{ij}^{dev} >_{V_{RVE}} : < \varepsilon_{ij}^{dev} >_{V_{RVE}}}} \tag{2.27}$$

Once again, a scale factor establishes the feasibility of this proposal, which demands that the RVE must be small enough to account as a material point and large enough to represent the microstructure statistically.

As the material changes from a complete homogeneous into a microheterogeneous medium, one of the forms to account for the perturbations is to separate the strain and stress into a uniform field and into a deviatoric field induced by the defects. This deviation will be called equivalent eigenstrain or eigenstress, allowing us to add the effects of the inclusions into the constitutive properties.

2.3.3 Field Fluctuation at the Boundary Conditions

From the Hill's condition previously reported and applying the divergence theorem and the equilibrium conditions, it is possible to derive Equation 2.28, where, the sum of the fluctuations related to the average is null. Figure 2.11 shows this interpretation where it is clear that to be energetically equivalent, the expression must be fulfilled.

$$\frac{1}{V_{RVE}} \cdot \int_{\partial A_{RVE}} \left(u_i - < \varepsilon_{ij} > x_j\right)\left(\sigma_{ik} - < \sigma_{ik} > x_j\right) n_k dA = 0 \tag{2.28}$$

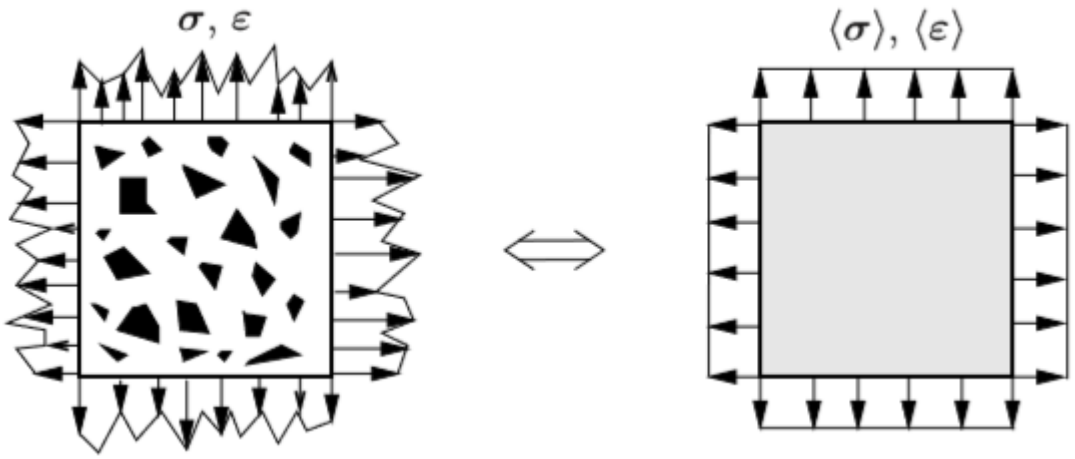

Figure 2.11 – The variations at the boundary conditions in the microscale and the averaged macroscale. The fluctuations between both are a measure of error conceived by the Hill's conditions. [Gross and Seelig, 2006]

2.3.4 Eshelby Solution

Eshelby, 1957 develop the solution for an ellipsoidal inclusion embedded in an infinite medium under a uniform load. A certain eigenstrain region ε^t unconstrained by a surrounded matrix will not yield by itself stress at the body. However, the constraining process will establish a relation among the total strain ε, the elastic strain ε^e and the eigenstrain ε^t. Equation 2.29 and Equation 2.30 present this association and introduce the four-order Eshelby Tensor ${S^e}_{ijkl}$ which relates to the total strain and the eigenstrain. The solutions are valid only for constant strains and for the inner region of the inclusion.

$$\underbrace{\varepsilon_{ij}}_{Tot.strain} = \underbrace{\varepsilon^t_{kl}}_{eigenstrain} + \underbrace{\varepsilon^e_{kl}}_{elast.strain} \rightarrow \sigma_{ij} = C_{ijkl} \cdot \varepsilon^e_{kl} \rightarrow \sigma_{ij} = C_{ijkl} \cdot (\varepsilon_{ij} - \varepsilon^t_{kl}) \tag{2.29}$$

$$\varepsilon_{ij} = {S^e}_{ijkl} \cdot \varepsilon^t_{kl} \quad \rightarrow \quad \sigma_{ij} = C_{ijkl} \cdot ({S^e}_{klmn} - 1_{klmn})\varepsilon^t_{mn} \tag{2.30}$$

When an ellipsoidal inclusion degenerates into a spherical one, the solution for the Eshelby Tensor can be written as in Equation 2.31. Note that the geometry of the sphere is disregarded and the Eshelby Tensor is only dependent on the Poisson's ratio ϑ. For non-spherical geometries, the components of the Eshelby Tensor can be found in Mura, 1983.

$${S^e}_{ijkl} = \frac{1+\vartheta}{3(1-\vartheta)} \cdot \frac{1}{3}\delta_{ij}\delta_{kl} + \frac{2(4-5\vartheta)}{15(1-\vartheta)}\left(I_{ijkl} - \frac{1}{3}\delta_{ij}\delta_{kl}\right) \tag{2.31}$$

The solution presented can be extended to evolve a perturbated field when an external displacement $u(x)$ or traction $t(x)$ is applied at the extreme boundaries $\partial\Omega_o$. The stiffness tensor, considering the linear superposition, can be defined as Equation 2.32 and it is shown graphically in Figure 2.12 for better understanding.

$$C(x)_{ijkl} = C_{0_{ijkl}} + \overline{C(x)}_{ijkl} \tag{2.32}$$

$C_{0_{ijkl}}$: Constant stiffness tensor of the matrix material in Ω_o.

$\overline{C(x)}_{ijkl}$: Piecewise complement owing to the presence of inclusions $\Omega_1, \Omega_2, \Omega_3$ etc. Nonzero value only inside the heterogeneities.

$C(x)_{ijkl}$: Resultant tensor for the whole body being complemented by $\overline{C(x)}_{ijkl}$ inside the inclusion.

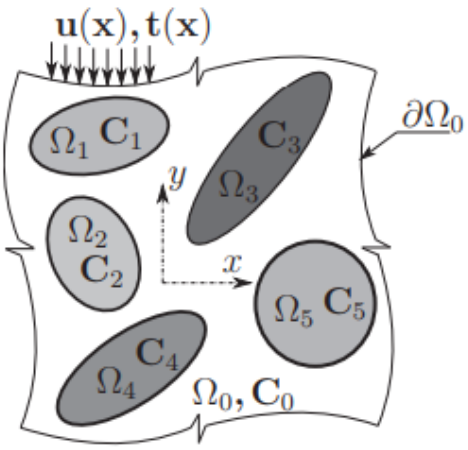

Figure 2.12 - Eshelby ellipsoidal inhomogeneities embedded in an infinity medium under far-fields $u(x)$ and $t(x)$. [Svoboda et al., 2016]

Note that the local fields can also follow the same superposition principle. As a result, strain, displacement and stress can follow the same rule as presented in Equation 2.33.

$$\varepsilon(x)_{ij} = \varepsilon^0{}_{ij} + \overline{\varepsilon(x)}_{ij} \;, \quad \sigma(x)_{ij} = \sigma^0{}_{ij} + \overline{\sigma(x)}_{ij} \quad , \quad u(x)_i = u^0{}_i + \overline{u(x)}_i \tag{2.33}$$

The Eshelby results can be applied only for weakly or non-interacting particles. Therefore, the analysis of just one ellipsoidal particle suffices. The system can be replaced from a heterogeneous problem with two constituents by one equivalent defined by a stress-free eigenstrain ε^t_{ij} replacing the inclusion. From the term $\sigma(x)_{ij}$ in Equation 2.33 and substituting the tensorial terms by the constitutive relations, it becomes easy to derive:

$$\overline{\sigma(x)}_{ij} = C_{0_{ijkl}} \left[\overline{\varepsilon(x)}_{ij} + \underbrace{C_{0_{ijkl}}{}^{-1}\left[C(x)_{klmn} - C_{0_{klmn}}\right]\varepsilon(x)_{ij}}_{-\varepsilon(x)^t{}_{ij}\ (similar\ to\ eigestrain)} \right] = C_{0_{ijkl}} \left[\overline{\varepsilon(x)}_{ij} - \varepsilon(x)^t{}_{ij} \right] \tag{2.34}$$

The definition of the Eshelby Tensor in Equation 2.30 for the region inside the inclusion and the application of Equation 2.34 into 2.33 allows us to substitute the terms and arrive in Equation 2.35. As the general conditions are constants, $C(x)$ becomes the tensor C_1 representing the inhomogeneity at the volume Ω_1 and C_0 defines the constitutive matrix tensor C_M. The

term A_I that relates the total strain ε_{ij} inside the inhomogeneity Ω_1 and the external far-load ${\varepsilon^0}_{kl}$ is called Influence Tensor.

$$\varepsilon_{ij} = \left[1_{ijkl} + {S^e}_{ijmn}\, {C_{M}}_{mnpo}^{-1} \left({C_1}_{pokl} - {C_M}_{pokl}\right)\right]^{-1} {\varepsilon^0}_{kl} = {A_I}_{ijkl}\, {\varepsilon^0}_{kl} \tag{2.35}$$

The application of the relation $\sigma_{ij} = {C_1}_{ijkl}\varepsilon_{kl}$ for the inclusion and ${\sigma^0}_{ij} = {C_M}_{ijkl}{\varepsilon^0}_{kl}$ for the matrix in Equation 2.35 will evolve to a solution for the stress inside the inhomogeneity:

$$\sigma_{ij} = \left[{C_1}_{ijmn} {A_I}_{mnpo}\, {C_M}_{pokl}^{-1}\right] {\sigma^0}_{kl} = {B_I}_{ijkl}\, {\sigma^0}_{kl} \tag{2.36}$$

The solutions here described are only applicable inside the perturbation while the outer fields have an asymptotic behavior. For most of the geometries, besides ellipsoidal inhomogeneities, the solution does not have a closed form. The inclusion also cannot be neighboring each other due to yielding field distortions. Figure 2.13 presents the simplification of the original problem graphically into an eigenstrain problem.

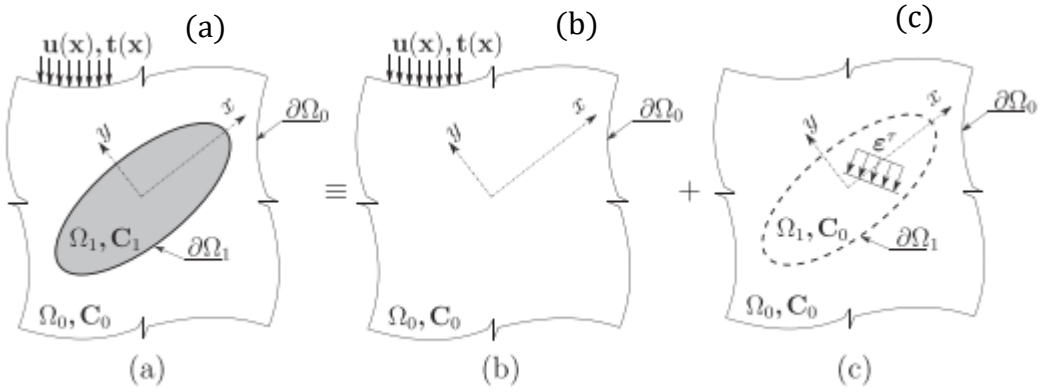

Figure 2.13 – (a) The complete problem with inhomogeneity. (b) The supplement with an external load applied. (c) homogeneous inclusion adding an eigenstrain feature. [Svoboda et al., 2016]

Considering the Hill's condition and that the influence tensors ${B_I}_{ijkl}(x)$ and ${A_I}_{ijkl}(x)$ are equal to unity when the average value of its functions is performed at the domain, a solution for the average stiffness tensor C^* can be obtained [Gross and Seelig, 2006]. Equation 2.37 defines this entity considering a constant strain field (A) or a constant stress field (B) at Ω_o. The equality of C^{*B} and C^{*A} is a way to measure the quality of these averages.

$$C^{*B} =< B^T : C^{-1} : B >^{-1}{}_{V_{RVE}} \; or \; C^{*A} =< A^T : C : A >_{V_{RVE}} \tag{2.37}$$

Most scenarios in micromechanics only consider two phases. The development of Equation 2.37 considering the concentration of the inhomogeneity C_1 inside a matrix C_M will entail two expressions defined by Equation 2.38.

$$C^{*B} = (C_M^{-1} + c_1(C_1^{-1} - C_M^{-1}) : B_I)^{-1} \; or \; C^{*A} = C_M + c_1(C_1 - C_M) : A_I \tag{2.38}$$

2.3.5 Microcracks

Typically, the first thought when dealing with voids in the previously presented approximation, would be to define C_1 as zero. For crack applications, a natural configuration would establish one dimension of the ellipsoidal inclusion much larger than the other two. However, a different approach will be assumed due to the changes in the boundary value problem and the stress-free state at the crack surface.

The divergence theorem, taking into account the average strain field for a RVE, will result in surface integral as presented in Equation 2.39 and Equation 2.40 where n_j is the normal vector related to the cavity/crack and u_j is the displacement of such surface (Figure 2.14).

$$< \varepsilon_{ij} >_c = \frac{1}{V} \cdot \int_v \varepsilon_{ij}(x) \partial v = \frac{1}{2V} \cdot \int_A u_i n_j + u_j n_i \, \partial A \tag{2.39}$$

$$< \sigma_{ij} >_c = \frac{1}{V} \cdot \int_v \sigma_{ij}(x) \partial v = \frac{1}{2V} \cdot \int_A t_i x_j \partial A \tag{2.40}$$

It holds valid approaching a vanishing stiffness as well. The fragmentation of the entire RVE defines a constant that can be used as a weight parameter ($c_n = V_n / V_{RVE}$). c_M is the relative volume of the matrix material, while c_1 is the partial volume of the inclusion number one and c_c is the partial volume of the crack. As the crack has no contribution to the total volume, one can define the overall strain as the matrix strain $< \varepsilon_{ij} >_M$ and c_M equal to one as the fraction of the crack c_c is nearly null. Applying the divergent theorem at the external area of the body ∂V and including the internal surface of the crack $\partial \Omega_c$, the derivation of Equation

2.41 can be made. Observe how Equation 2.42 is similar to Equation 2.29, which is related to the eigenstrain formulation.

$$< \varepsilon_{ij} >= c_M < \varepsilon_{ij} >_M + \frac{1}{2V} \cdot \int_{\partial\Omega_c} u_i n_j + u_j n_i \, \partial A = < \varepsilon_{ij} >_M + \underbrace{< \varepsilon_{ij} >_c}_{crack\ effect} \tag{2.41}$$

$$< \sigma_{ij} > = C_{ijkl}{}_M (< \varepsilon_{kl} >_M + \underbrace{< \varepsilon_{kl} >_c}_{crack\ effect}) \tag{2.42}$$

So far, all the scenarios converge in a transformation from a statistically homogenous material with cracks, voids and other phases into a simplified case where an eigenstrain is imposed to simulate the influence of the micro constituents.

The expressions from Equation 2.38 related to the averaged material properties of the two-phase media cannot be applied directly for the voids and cracks cases. In this case, the crack strain tensor ε_c is related to the average strain field ε^0 by a damage influence tensor defined as D^d. Conversely, the stress path will lead to H^d. Equation 2.43 designates the effective elasticity tensor, where it is clear to visualize the reduction of the matrix stiffness due to the presence of the damages inside the representative volume.

$$C^{*B} = (C_M^{-1} + H^d)^{-1} \; or \; C^{*A} = C_M : (1 - D^d) \tag{2.43}$$

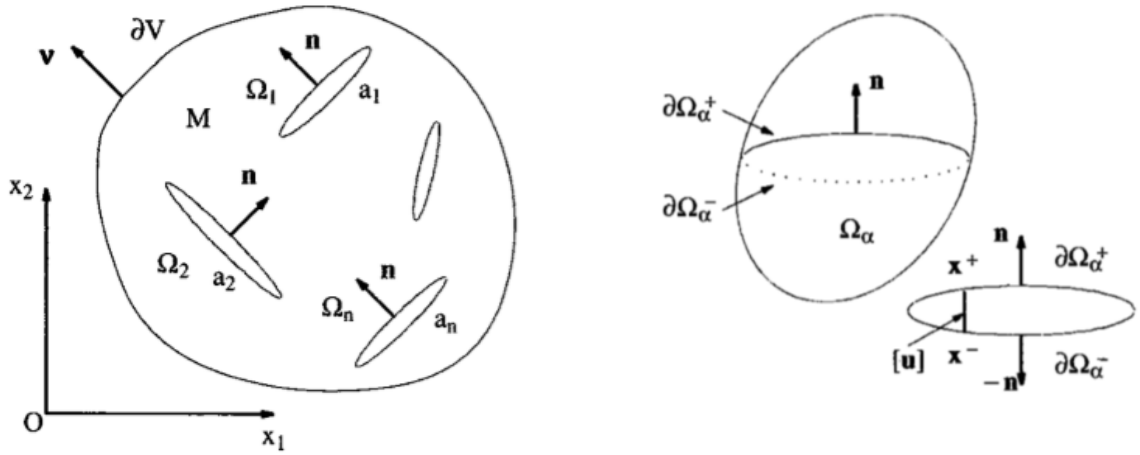

Figure 2.14 – The presence of voids/cracks defines a normal direction of an inner surface $\partial\Omega_c$ adding to the problem a stress-free consideration at the boundaries. [Nemat-Nasser and Hori, 1999]

All the Equations mentioned earlier are applicable for evenly spread cracks, voids and faults and there is no field interference among different inhomogeneities. Henceforth, this type of analysis will be called a Dilute solution.

2.3.6 Dilute Distribution of Cracks

The consideration of a crack placed in a $x_1 - x_2$ plane with a total length of $2a$ ($x_1 = -a\ to\ x_1 = a$) allows defining the displacement vector u_i as a function of crack size, position and stress components. Equation 2.44 provides us with the characterization of u_i for plane strain and plane stress condition, where G is set as the in-plane shear modulus and κ is dependent on the plane strain or plane stress state according to Figure 2.15 orientation. The Equation is valid for $|x_i| \leq a$. $\kappa = 3 - 4\vartheta$ for plane strain and $\kappa = (3 - \vartheta)/(1 - \vartheta)$ for plane stress.

$$\begin{pmatrix} u_1 \\ u_2 \\ u_3 \end{pmatrix} = \sqrt{a^2 - x_1^2} \cdot \frac{4}{E'} \begin{pmatrix} \sigma_{12}^o \\ \sigma_{22}^o \\ 0 \end{pmatrix} \rightarrow E' = \frac{8G}{\kappa + 1} = \begin{cases} \dfrac{E}{1 - \vartheta^2} & plane\ strain \\ E & plane\ stress \end{cases} \tag{2.44}$$

In the hypotheses of alignment of all the cracks with the x_2-axis as presented in Figure 2.15, the changes in the properties will be similar to a uniaxial tension test equal to σ_{22}. Conversely, under compression, the cracks close and no effect will be observed.

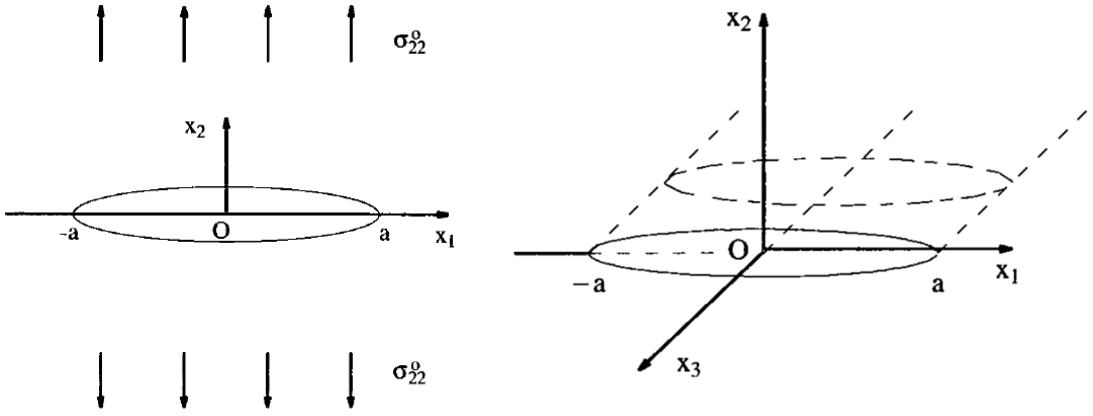

Figure 2.15 – Crack configuration of size $2a$ with uniaxial far-field stress ${\sigma_{22}}^o$. [Nemat-Nasser and Hori, 1999]

Under dilute circumstances and multiple cracks, a definition called crack density parameter f facilitates our approach to the problem. The constant f is defined as the number

of cracks N_f per unit area multiplied by the crack size parameter a^2, i.e., $f = N_f \cdot a^2$ regarding that all cracks have the same size $2a$. From Equation 2.39 and integrating the displacement over the crack length, it will result in Expression 2.45, which relates the induced crack strain and far-field stress over the x_2-axis.

$$\varepsilon_{22}{}^{c} = N_f \cdot a^2 \cdot \frac{1}{a^2} \int_{-a}^{a} u_2 dx_1 = f \frac{2\pi}{E'} \sigma_{22}{}^{o} \tag{2.45}$$

The same analysis can be performed for σ_{12} which allows deriving the matrix form of a new constitutive tensor applying Equations 2.41 and 2.42. The macrostress path will lead to the tensor H^d that will modify the compliance tensor S_M yielding an average compliance tensor S^*. Expression 2.46 presents the formulation for a plane stress state (PSS) and for plane strain state (PSN), while Equation 2.47 presents the same scenario for a macrostrain field. Note that the Expressions are for N_f cracks with size $2a$ aligned according to Figure 2.15 in an isotropic medium. The Equations below is just valid under traction, which imposes the necessity to add the Heaviside step function H to only positive far-field values. This is called a "closed" crack form. If the compressive state behaves similarly to the traction mode, the Heaviside function is not necessary and the process becomes a permanent "open" form independent on the load condition. Section 3.1 will address a clear differentiation between these two schemes (open and close form). For the sake of simplification, the presented formulations will consider only the "open" type.

$$S^* = S_M + H^d = \frac{1}{G} \begin{pmatrix} \frac{\kappa+1}{8} & \frac{\kappa-3}{8} & 0 \\ \frac{\kappa-3}{8} & \frac{\kappa+1}{8} & 0 \\ 0 & 0 & 1 \end{pmatrix} + f \frac{\pi(\kappa+1)}{4G} \begin{pmatrix} 0 & 0 & 0 \\ 0 & 1 & 0 \\ 0 & 0 & 1 \end{pmatrix} \tag{2.46}$$

$$C^* = C_M + C_M : D^d = G \begin{pmatrix} \frac{\kappa+1}{\kappa-1} & -\frac{(\kappa-3)}{(\kappa-1)} & 0 \\ -\frac{(\kappa-3)}{(\kappa-1)} & \frac{\kappa+1}{\kappa-1} & 0 \\ 0 & 0 & 1 \end{pmatrix} + f \frac{\pi(\kappa+1)\mathrm{G}}{4(\kappa-1)^2} \begin{pmatrix} (\kappa-3)^2 & -\frac{(\kappa-3)}{(\kappa+1)} & 0 \\ -\frac{(\kappa-3)}{(\kappa+1)} & (\kappa+1)^2 & 0 \\ 0 & 0 & (\kappa-1)^2 \end{pmatrix} \tag{2.47}$$

The development of Equation 2.46 in macrostress, can evolve to a mathematical expression for an in-plane nominal Young's Modulus $\overline{E_2}$ at the x_2-axis and for an in-plane shear modulus $\overline{G_{12}}$.

$$\overline{E_2} = \frac{E'}{1 + 2\pi f} \quad and \quad \overline{G_{12}} = \frac{G}{1 + f\,\frac{\pi(\kappa+1)}{4}} \tag{2.48}$$

For the x_1-axis, as the alignment was performed perpendicular to it, it is evident that the Young modulus $\overline{E_1}$ will not change:

$$\overline{E_1} = E' \tag{2.49}$$

Similar expressions for $\overline{E_2}$, $\overline{G_{12}}$ and $\overline{E_1}$ can be derived considering a macrostrain field.

However, a more interesting approach for the ongoing study is presented by Horii and Nemat-Nasser, 1983, where a random orientation of the cracks is defined. It means that the orientation angle of each fault is not equal to each other, making it not relevant to the averaging process. Nevertheless, the assumption of "open" cracks must be defined and the influence tensor H^d and $C_M{:}D^d$ must be set as naturally isotropic. Expressions 2.50 and 2.51 present the matrix form for the averaged compliance tensor (macrostress) and for the averaged stiffness tensor (macrostrain), respectively. It is possible to derive the overall properties as a function of the crack density f are shown as in Equation 2.52 for a macrostress scenario. Similar results can be extracted from a macrostrain scheme.

$$S^* = S_M + H^d = \frac{1}{G}\begin{pmatrix} \frac{\kappa+1}{8} & \frac{\kappa-3}{8} & 0 \\ \frac{\kappa-3}{8} & \frac{\kappa+1}{8} & 0 \\ 0 & 0 & 1 \end{pmatrix} + f\,\frac{\pi}{E'}\begin{pmatrix} 1 & 0 & 0 \\ 0 & 1 & 0 \\ 0 & 0 & 2 \end{pmatrix} \tag{2.50}$$

$$C^* = C_M + C_M{:}D^d = C_M + C_M \cdot f\,\frac{\pi(\kappa+1)}{8(\kappa-1)}\begin{pmatrix} \kappa+1 & -(\kappa-3) & 0 \\ -(\kappa-3) & \kappa+1 & 0 \\ 0 & 0 & 2(\kappa+1) \end{pmatrix} \tag{2.51}$$

$$\overline{E_{1\ and\ 2}} = \frac{E'}{1 + \pi f} \ and\ \overline{G_{12}} = \frac{G}{1 + f\,\frac{\pi(\kappa+1)}{4}} \tag{2.52}$$

The exemplified solutions presented above only considers frictionless faults and crack size parameter $f \ll 1$ due to non-interacting fields condition.

2.3.7 Self-Consistent Estimative for Cracks Distribution

The dilute distribution assumes an external far-field ε_o or σ_o and a noninteracting perturbation among the faults, cracks, inclusion or inhomogeneities in general. Mori and Tanaka, 1973 introduced a new form, where an averaged matrix far-field ε_M or σ_M is accounted for each individual inhomogeneity. Still, the system is vastly influenced by position-dependency and the local fluctuations must be neglected. In these two direct approaches, the concentrations and the Eshelby tensors must be averaged over the RVE. The study of the effect caused by a significant second phase concentration can be found in Nemat-Nasser and Hori, 1999, Svoboda et al., 2016 and Gross and Seelig, 2006. It is easily shown that when the concentration c_1 tends to unity, the solution will be similar to the Dilute approximation, which is the case for crack analysis.

When the inclusions interact up to a certain extent, the Self-consistent model is a better approach to the problem. It is an energy averaging method through the equalization of the strain energy stored in the heterogeneous medium and in the equivalent homogeneous medium. There is no need to add field averaging. "A representative fragment of this model contains an inclusion embedded in a concentric layer of the matrix material of the prescribed volume fraction, which in turn is embedded in an infinite medium possessing the unknown effective properties" [Lurie et al., 2018]. The solution will lead to uniform boundary conditions and the description of the fields inside the phases as well as the averaged properties. The application of the Self-consistent method for oriented cracks, as presented in the dilute method, will lead to a cumbersome analysis due to the necessity to evaluate the solution of every single fault in an anisotropic medium. The development of this theory is not treated in this study, and typically can be found in advanced micromechanics books. The solutions presented here are for randomly and equally distributed cracks defining an isotropic behavior.

The Influence tensor in the Self-consistent method $H^{d(SC)}$ can be presented with the fourth-order tensor as in Equation 2.55. However, two new variables $\bar{\kappa}$ and $\bar{G}$ must be solved before using Equations 2.53 and 2.54. The solutions are valid for macrostress and macrostrain approach.

$$\overline{G^{(SC)}} = \frac{G(1 - f\,\pi)}{1 - f\,\frac{\pi\,(\kappa - 3)}{4}} \tag{2.53}$$

$$\overline{\kappa^{(SC)}} = \frac{\kappa\left(1 - f\,\frac{\pi\,(\kappa-3)}{4\kappa}\right)}{\left(1 - f\,\frac{\pi\,(\kappa-3)}{4}\right)} \tag{2.54}$$

$$H_{ijkl}^{d(SC)} = f\frac{\pi\left(\overline{\kappa^{(SC)}} + 1\right)}{16\overline{G^{(SC)}}}\left(\delta_{ik}\delta_{jl} + \delta_{il}\delta_{jk}\right) \tag{2.55}$$

Figure 2.16 presents the changes in the overall shear and Young Moduli according to the increasing crack size factor f [Nemat-Nasser and Hori, 1999]. The DD:Σ represents the Dilute solution using the macrostress approach, while DD:E is the solution according to the strain path. SC is the representation of the Self-consistent method. The Poisson' ratio ϑ was set as 1/3 and a plane stress condition was defined. Observe the divergence as the crack fraction f increases. Even though, for values larger than f >>0.15, neither Self-consistent nor Dilute methods are reliable. This interpretation can also be seen in Gross and Seelig, 2006 for a random distribution of circular faults.

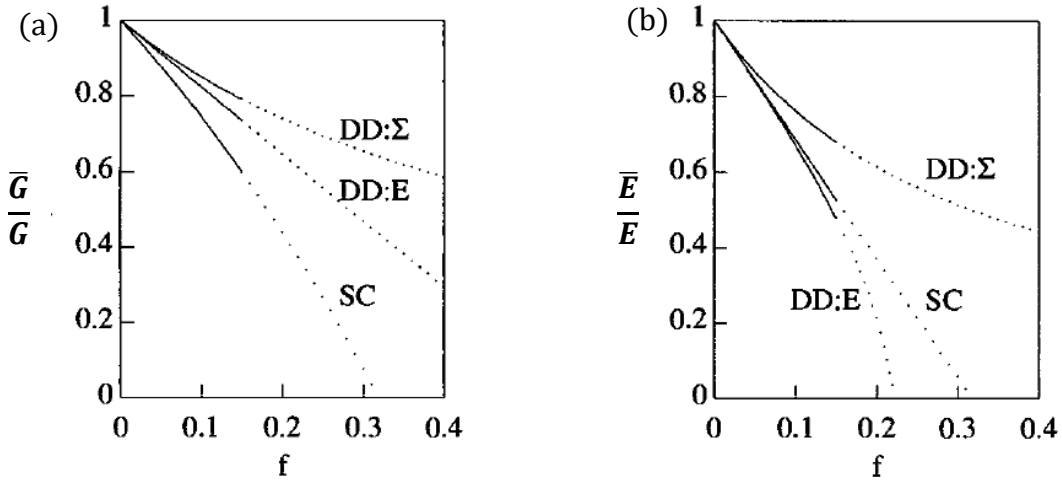

Figure 2.16 - Modification of the overall parameter according to increasing random distributed cracks f with size 2a. DD:Σ the solution for the dilute case with macrostress applied. DD:E is the solution for macrostrain. SC is the solution using Self-consistent method. Poisson's ratio ϑ set as 1/3. Plane stress regime. (a) The evolution of the shear modulus. (b) The evolution of Young's Modulus. [Nemat-Nasser and Hori, 1999]

Direct equations can be obtained, deriving the expression above to calculate the most common isotropic parameters. Table 2.1 shows the Equations for ϑ, E and G applying plane stress (PSS) and plane strain (PSN) and the Self-consistent method. This method takes into

account a certain degree of interaction among the cracks and, therefore, it is considered a more reliable and accurate approach to establish the overall properties of the RVE.

Table 2.1 - Expression for Poisson's ratio, shear and Young Moduli according to the Self-Consistent method. Plane stress (PSS) and Plane strain (PSN) are presented. Isotropic crack distribution.

Plane Stress (PSS)	Plane Strain (PSN)
$\overline{G^{(SC)}} = G(1 - f\pi)\left(1 - f\frac{\pi\vartheta}{1+\vartheta}\right)^{-1}$	$\overline{G^{(SC)}} = G(1 - f\,\pi)(1 - f\,\pi\vartheta)^{-1}$
$\overline{E^{(SC)}} = E'(1 - f\,\pi)$	$\overline{E^{(SC)}} = E'(1 - f\pi)(1 - f\pi\vartheta^2)^{-1}$
$\overline{\vartheta^{(SC)}} = \vartheta(1 - f\pi)$	$\overline{\vartheta^{(SC)}} = \vartheta(1 - f\,\pi)(1 - f\,\pi\vartheta^2)^{-1}$

2.4 Materials Behavior and Damage Models in Lattice Structures

During uniaxial loading and unloading scenarios for pure ductile materials, the elastic slope in the stress-strain plot remains constant, determining a constant elastic modulus independent on the strain extension (Figure 2.17a). Conversely, brittle behavior is associated with nucleation and growth of microcracks without damage accumulation, which leads to the loss of interatomic bonds abruptly (Figure 2.17b). Quasi-brittle materials present the loading curve not necessarily linear due to a progressive accumulation of damage. There is not a bond rupture but instead a bond deterioration which drives to stiffness decrement with loading (Figure 2.17c). Assuming a perfect quasi-brittle material, the absence of bonds sliding conducts its unloading process to the origin. The residual stress is negligible and the loss of stiffness can describe the loading history. Conventional materials are never perfectly brittle or ductile, leading to a mix as plotted in Figure 2.17d. The phenomenon of cleavage in fragile media is related to the atomic decohesion, which is macroscopically characterized by the damage, while dislocation and propagation of the crack tip are associated with the ductile structures [Krajcinovic, 1996].

Additionally, it is advisable to consider in the microstructure a certain degree of randomness in its properties in order to compute and simulate real engineering materials. The statistical models introduce disorder, which varies the characteristics and properties of the continuum. The fact that more and more new composites are under development, characterized

by microstructural heterogeneities and, therefore, with an intrinsic statistical distribution of one or more properties, makes the use of such models suitable or even imperative for the analysis.

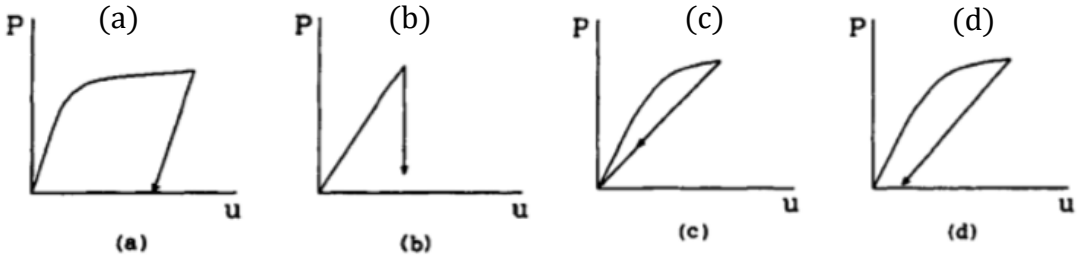

Figure 2.17 - (a) Ductile. (b) perfectly brittle. (c) Quasi-brittle. (d) Ductile-brittle. Uniaxial force P x displacement u. Response according to the material categories. [Krajcinovic, 1996]

The simplest model [Krajcinovic and Silva, 1982 apud Krajcinovic, 1996] to compute damage is a loose bundle of parallel bars. Each bar has a portion of the total stiffness K. Each bar, therefore, has individual stiffness K/N, being N the total representative number of bars. The links differentiate one from another by defining a probability density function for the rupture strength f_{rup}. The increments of force F (Figure 2.18a) or displacement happen considering a quasi-static process. For brittle deformation, when the forces at the weaker link (f_i) exceed the rupture strength f_{rup}, all other bar must withstand the total applied load. The effective number of links n decreases from the initial configuration N yielding a new effective secant stiffness constant K_{sec}^{eff}. The relation n/N can be established as a measure of damage or, due to its intrinsic cumulative characteristic, the integral of the rupture force's probability function $p(f_{rup})$.

Figure 2.18b shows the dotted area relative to the energy released U^d due to damage. The plot represents the overall relation of Force x Displacement where F_m represents the maximum force supported by the strongest link. In a force-controlled system, after that point, the total rupture would occur in an avalanche mode since the domain is unable to carry forces that surpasses F_m.

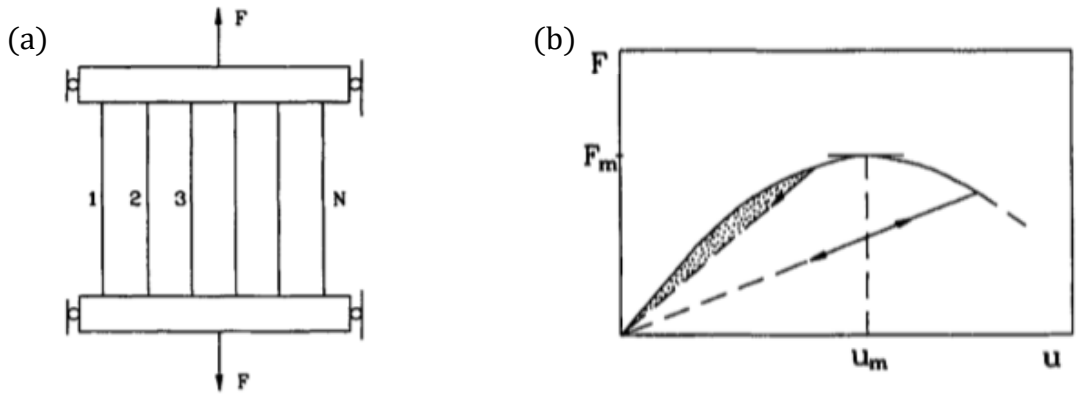

Figure 2.18 - (a) Bundle of parallel bars with random strength distribution. (b) Force x displacement of the overall bundle. The dotted area is the rupture energy and the dashed lines is the unloading process for quasi-brittle materials. [Krajcinovic, 1996]

The description in Equation 2.56 until Equation 2.58 shows the mathematical formulation for this simple system. A uniaxial damage parameter is introduced as aforementioned and adding the probability function according to a natural distribution of properties over the body.

$$F = \sum_{i=1}^{N} f_i = K\left(1 - \frac{n}{N}\right) \cdot u = K(1 - D^d) \cdot u = K_{sec}^{eff} \cdot u \tag{2.56}$$

$$K_{sec}^{eff} = K(1 - D^d) \tag{2.57}$$

$$D^d = \int_{f_{min}}^{ku} p(f_{rup}) df_{rup} \tag{2.58}$$

The probability function choice is crucial to define the material behavior. The failure occurs very abruptly when systems with small variations from the average value took place. The considered response is brittle as no damage accumulation occurs (damage sensitive). For substantial bandwidth rupture strength, the material is microheterogeneous and it is associated with ductile fracture (damage tolerant). The description using one dimension, nevertheless, is not capable of representing the majority of state stress in engineering materials. Lattices formed by links and nodes, therefore, are an appealing approximation form to evaluate the continuum.

As previously discussed in Section 2.3.1, the mathematical considerations for an RVE region must follow Equations 2.59.

$$d_{microconst.} \ll D_{RVE} \ll D_{macro} \quad and \quad \left|\frac{\partial \sigma_o}{\partial x}\right| D_{RVE} \ll \sigma_o \tag{2.59}$$

In the cases of microcracks, their orientation and position in the RVE cannot affect the overall response. Therefore, the cracks are comparable to the size of the microconstituents. The translational invariance can only alter the global properties only through their density function and the interaction among the cracks must be negligible.

An irreversible thermodynamic process defines damage as a decreasing amount of material bonds and an increasing total internal RVE's area. Unfortunately, the direct evaluation of the microcracks evolution is not possible, being necessary to measure it indirectly by the effects on the stiffness tensor. Therefore, damage evolution is a macroscopic manifestation of the net loss of interatomic bonds in the course of the nucleation of new and growth of the existing microcracks [Krajcinovic and Vujosevic, 1998].

The Griffith elastic energy release rate G has an essential role in this evaluation. The crack growth only is possible when at the vicinity of the crack tip, G surpasses the bond thermodynamic force R at a specific stress level. Nevertheless, G and R are very difficult to be defined precisely. The cracks are seldom planar, have an irregular shape and typically are not embedded in an isotropic and homogeneous continuum. The accumulated damage and barriers, like grains contour, also affect greatly R, which implies that these constants are random distribution function over the domain.

A damage tolerant material is when the probability distribution $R(x)$ has a large bandwidth to prevent or hinder the crack from growing. This scenario occurs when a large number of microheterogeneous generates restraints for crack evolution. On the other hand, a damage sensitive material has a narrow $R(x)$ bandwidth, which means a more homogeneous microstructure. This leads to typical unstable circumstances.

As the random nucleation evolves and the number of defects increases, the locals of stress concentrations spread. This fact widens the G probability function and as a result, the probability of the relation between G and R surpassing the unity value increases. From that point on, the balance tilts from microcracks nucleation to defect growth. Figure 2.19 presents the case for damage tolerant and damage sensitive materials. On the right, it shows the damaging effect on the G factor.

$$G\left(\sigma(x_o)\right) \gg R(x_o) \tag{2.60}$$

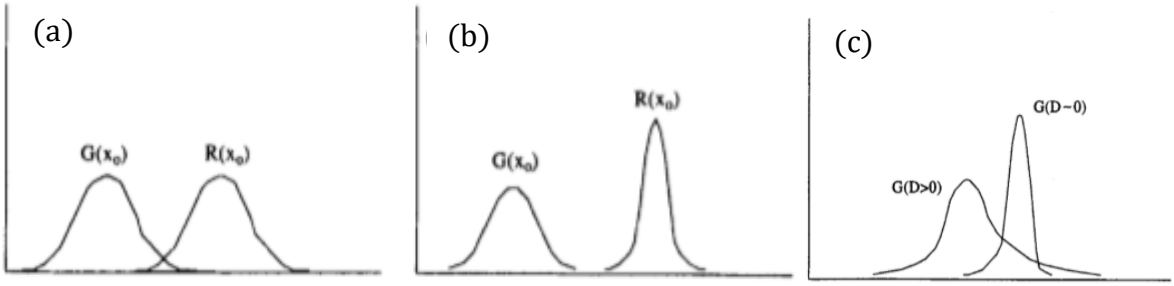

Figure 2.19 - (a) damage tolerant material. (b) damage sensitive material. (c) Changes in parameter G due to damage increment. [Krajcinovic and Vujosevic, 1998]

The nucleation process is a random feature over the domain which secures the homogeneity characterization. The damage density increases over time and the damage clusters start to interact with each other. The strain intensifies and the cooperative effect of the interacting cracks defines a local inhomogeneity. The length of the microcrack approaches the RVE size leading to the collapse of the homogenization hypothesis.

Figure 2.20 shows a 2D lattice with 3535 particles (nodes) connected by Hookean links of equal stiffness simulating a quasi-brittle material. The particular description of the lattice structure type is not presented in this work, but it can be found in Krajcinovic and Vujosevic, 1998. As the loading process increases at the borders of the lattice structure, the concentration of a large strain field which characterizes a band of faults is visualized. Due to the strain-controlled simulation, as a specific fault region prevails, the stresses at the borders are relaxed and other possible new bands are not created.

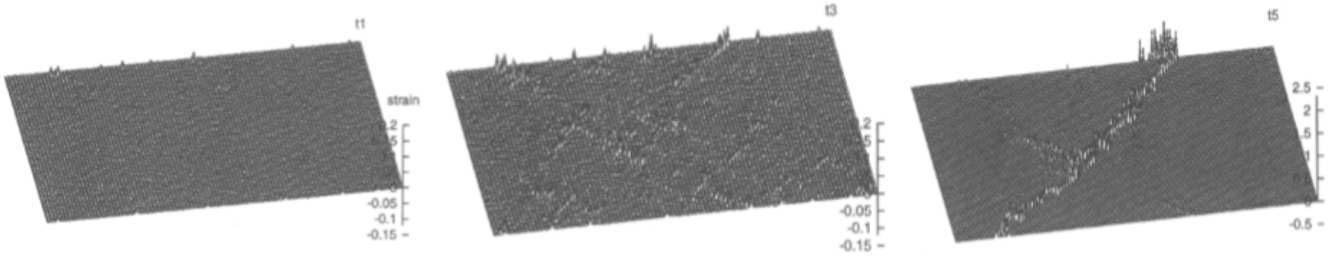

Figure 2.20 - Lattice simulation of quasi-brittle material showing the strain deformation as the damage spread over the plate until a peak is observed in specific regions forming the so-called band fault. [Krajcinovic and Vujosevic, 1998]

The procedure to characterize percolation is by introducing defects (voids or slits) randomly distributed over the domain and, secondly, by externally quasi-static traction to determine the components of the stiffness tensor. The load must be small enough to avoid any type of propagation. These two steps can be continuously repeated. At some moment, the defects will overlap and the formation of clusters will begin. The definition of the onset of percolation is then described as:

$$d_{crack,slit\ or\ damage} \rightarrow D_{macro} \tag{2.61}$$

The damage induced yields the parameter D^d which can be described as the effect of porosity, voids and slits on the constitutive matrix. The Expression in 2.62 is applicable only on the limit of the dilute concentration of defects, which means the condition $d_{microconst.} \ll D_{macro}$ must be sustained.

$$C_{ijkl}^{damaged} = C_{ijkl}^{undamaged} \cdot \left(1_{ijkl} - D_{ijkl}^{d}\right) \tag{2.62}$$

According to Krajcinovic, 1996 the effective secant modulus C_{sec}^{eff}, defined by the unloading process, reduces when the damage density f_d is close to the critical damage density f_{crit}. When the constant r in Expression 2.63 is greater than unity, it means lightly changes in C_{sec}^{eff} occur close to the percolation.

$$C_{sec}^{eff} \propto (f_d - f_{crit})^r \ as\ f_d \rightarrow f_{crit} \tag{2.63}$$

Equation 2.62 is valid for r equal to unity and cannot be used in the vicinity of percolation. Another author, Jasiuk et al., 1994, evaluated the relation between damage concentration and elastic stiffness, introducing an increasing number of voids in a 210 x 210 triangular lattice. The plots in Figure 2.21 show the theoretical agreement of Eshelby solutions (section 3.1) with the simulated lattice with the distribution of random voids. The x-axis represents the fraction area f composed by these discontinuities. Up until f equal to 0.15, the solutions are considerably approximate.

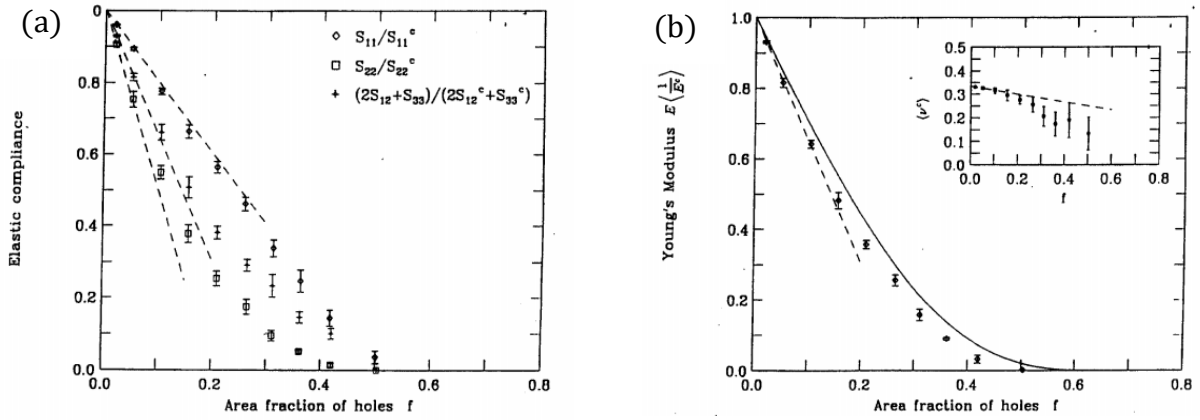

Figure 2.21 - (a) The dashed lines are the theoretical prediction of the dilute solution for ellipsoidal voids. The points are the compliance tensor terms (S) from the lattice simulation with randomly oriented faults. (b) The same scenario, but showing the evolution of Young's Modulus. The x-axis represents the relative fraction area f of the cracks. [Jasiuk et al., 1994]

Rinaldi et al., 2006 also applied the use of a Delaunay lattice to evolve quasi-brittle materials. It describes that the primary microstructural failure associated with these materials is due to the rupture of interfaces caused by an inferior strength or lower fracture energy when compared to the microscale constituents. Therefore, the separation of links defined by stochastic adhesion distribution represents the damage. When a link reaches critical strain, a permanent breach occurs, leading it to null tensile stiffness.

2.5 Constitutive Equations and Anisotropy

A damaged structure usually will induce some property modification in a specific direction. This will change the response of the body to a defined load and, therefore, the value of the constitutive tensor will no longer be as in an undamaged domain.

This section will prompt some aspects of constitutive equations that do not have the same response in every direction, the so-called anisotropic behavior. The goal is to relate the intrinsic anisotropy of materials with an induced anisotropy of cracked structures.

The scope of this work will only deal with a direct relation between strain and stress defined by an independent fourth-order stiffness tensor C_{ijkl} or a fourth-order compliance tensor S_{ijkl}. Due to the symmetry of the second-order stress tensor $\sigma_{ij} \rightarrow \sigma_{ji}$ and of the strain tensor $\varepsilon_{kl} \rightarrow \varepsilon_{lk}$, the stiffness and compliance tensor have a minor symmetry ($C_{ijkl} = C_{jikl} \leftrightarrow$

$C_{ijkl} \rightarrow C_{ijlk}$). Naturally, the eighty-one constants reduce to thirty-six unknowns, but due to requirements for the elastic energy to be wholly defined, a system of twenty-one material constants relates strain and stress completely. A more convenient and visual expression can be set using Voigt notation, reducing the order of the second-order tensor to a vector and a fourth-order to a second-order tensor as presented in Equation 2.64. The inverse of this relation introduces the compliance matrix S.

These materials are called anisotropic due to its directional dependence. Equation 2.64 is the more complex form and it is referred to as Triclinic. There is no plane or axis of dependency.

$$\begin{pmatrix}\sigma_{11}\\ \sigma_{22}\\ \sigma_{33}\\ \sigma_{23}\\ \sigma_{13}\\ \sigma_{12}\end{pmatrix} = \begin{pmatrix} C_{1111} & C_{1122} & C_{1133} & C_{1123} & C_{1131} & C_{1112} \\ & C_{2222} & C_{2233} & C_{2223} & C_{2231} & C_{2212} \\ & & C_{3333} & C_{3323} & C_{3331} & C_{3312} \\ & & & C_{2323} & C_{2331} & C_{2312} \\ & & & & C_{3131} & C_{3112} \\ & & & & & C_{1212} \end{pmatrix} \cdot \begin{pmatrix}\varepsilon_{11}\\ \varepsilon_{22}\\ \varepsilon_{33}\\ 2\varepsilon_{23}\\ 2\varepsilon_{13}\\ 2\varepsilon_{12}\end{pmatrix} \tag{2.64}$$

A plane of symmetry is defined as a plane in which the elastic properties have reflection symmetry. When there is one plane of symmetry at the 1-2 plane, the tensor reduces to thirteen constants. The fact that the 1-3 plane and 2-3 plane are not symmetrical leads to a shear stress relation dependent only on the shear strain at that axis or vice-versa. Some examples of these monoclinic materials are specific types of mineral crystals like the Selenite:

$$C^{mon} = \begin{pmatrix} C_{1111} & C_{1122} & C_{1133} & 0 & 0 & C_{1112} \\ & C_{2222} & C_{2233} & 0 & 0 & C_{2212} \\ & & C_{3333} & 0 & 0 & C_{3312} \\ & & & C_{2323} & C_{2331} & 0 \\ & & & & C_{3131} & 0 \\ & & & & & C_{1212} \end{pmatrix} \tag{2.65}$$

For three planes of symmetry, the material is called Orthotropic (Figure 2.22b). Usually, fiber-reinforced composites are in this class, therefore, of tremendous engineering interest. The tensor reduces to nine constants, as presented in Equation 2.66 for plane stress case. Each axis has its own Poisson's ratio, shear modulus and Young's modulus. In these materials, the shear stresses and shear strain are only dependent on each other:

$$S^{ortho} = \begin{pmatrix} \frac{1}{E_1} & -\frac{\vartheta_{21}}{E_2} & -\frac{\vartheta_{31}}{E_3} & 0 & 0 & 0 \\ -\frac{\vartheta_{12}}{E_1} & \frac{1}{E_2} & -\frac{\vartheta_{32}}{E_3} & 0 & 0 & 0 \\ -\frac{\vartheta_{13}}{E_1} & -\frac{\vartheta_{32}}{E_2} & \frac{1}{E_3} & 0 & 0 & 0 \\ 0 & 0 & 0 & \frac{1}{G_{23}} & 0 & 0 \\ 0 & 0 & 0 & 0 & \frac{1}{G_{13}} & 0 \\ 0 & 0 & 0 & 0 & & \frac{1}{G_{12}} \end{pmatrix}, \quad \begin{matrix} \frac{\vartheta_{32}}{E_2} = \frac{\vartheta_{32}}{E_3} \\ \frac{\vartheta_{21}}{E_2} = \frac{\vartheta_{12}}{E_1} \\ \frac{\vartheta_{13}}{E_1} = \frac{\vartheta_{31}}{E_3} \end{matrix} \tag{2.66}$$

The previous tensor can degenerate into a transversely isotropic material (hexagonal) where one plane, defined by z-axis in Figure 2.22a, has the same properties in all directions. A random distribution of fibers also would lead to in-plane isotropy. The transversely isotropic model has five independent constants, as presented in Equation 2.67 for a plane stress case. Figure 2.22b shows a complete orthotropic material, where the ellipsoidal fibers will induce different behavior in each direction. Distribution and form are not random in this case.

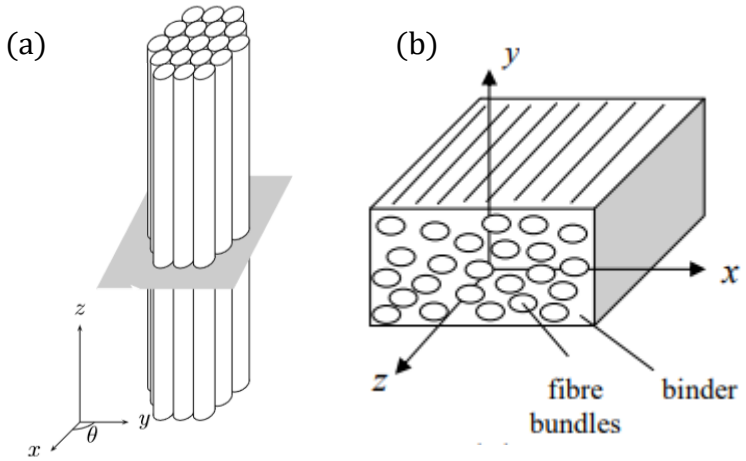

Figure 2.22 – (a) Transversely isotropic material (hexagonal). Circular fibers generating an isotropic behavior at the xy-plane. (b) The ellipsoidal or oval fibers which induces three orthogonal planes of symmetry defining an orthotropic material. [Kelly, 2015]

An essential feature of these orthotropic materials (orthorhombic) is that there is no shear coupling concerning the material axes. Normal stresses yield normal strains and shear stresses produce shear strains only. However, if the material directions 1, 2 and 3 and the loading case

are not aligned, a transformation will lead to a shear coupling case. The stiffness matrix will have to be rotated according to a procedure not presented in this work. Barbero, 2014 offers the systematic to deal with such circumstances.

$$S^{transv.iso} = \begin{pmatrix} \frac{1}{E_1} & -\frac{\vartheta_{12}}{E_1} & -\frac{\vartheta_{31}}{E_3} & 0 & 0 & 0 \\ -\frac{\vartheta_{12}}{E_1} & \frac{1}{E_1} & -\frac{\vartheta_{31}}{E_3} & 0 & 0 & 0 \\ -\frac{\vartheta_{13}}{E_1} & -\frac{\vartheta_{13}}{E_1} & \frac{1}{E_3} & 0 & 0 & 0 \\ 0 & 0 & 0 & \frac{1}{G_{23}} & 0 & 0 \\ 0 & 0 & 0 & 0 & \frac{1}{G_{13}} & 0 \\ 0 & 0 & 0 & 0 & & \frac{1}{G_{12}} \end{pmatrix}, \quad \frac{\vartheta_{13}}{E_1} = \frac{\vartheta_{31}}{E_3} \quad G_{12} = \frac{E_1}{2(1+\vartheta_{12})} \tag{2.67}$$

The isotropic materials are the simplest configuration possible where any plane can be considered a plane of symmetry. The two Lamé constants λ and G are independent and can be related to Poisson's ratio ϑ, Young's modulus E and bulk modulus k. The general expression for the matrix S can be simplified as Equation 2.68 for a plane stress case.

$$S^{iso} = \begin{pmatrix} \frac{1}{E} & -\frac{\vartheta}{E} & -\frac{\vartheta}{E} & 0 & 0 & 0 \\ & \frac{1}{E} & -\frac{\vartheta}{E} & 0 & 0 & 0 \\ & & \frac{1}{E} & 0 & 0 & 0 \\ & & & \frac{1}{G} & 0 & 0 \\ & & & & \frac{1}{G} & 0 \\ & & & & & \frac{1}{G} \end{pmatrix}, \quad G = \frac{E}{2(1+\vartheta)} \quad \lambda = \frac{E\,\vartheta}{(1+\vartheta)(1-2\vartheta)} \quad \mathrm{k} = \frac{E}{3(1-2\vartheta)} \tag{2.68}$$

For any given tensor that is extracted from a material, it possible to decompose the elastic tensor into a sum of orthogonal tensors that are related to different classes of symmetry, such as the ones described previously. This characterization can define the degree of anisotropy of a specific material under investigation. The present work will apply a technique developed in

Matlab® algorithm by Walker and Wookey, 2012. This program breaks the anisotropic tensor into isotropic, hexagonal, tetragonal, orthorhombic, monoclinic and triclinic components.

The MSAT ® code is a Matlab ® Seismic Anisotropy Toolkit developed to study seismic and elastic anisotropy. Geologists use these anisotropy measurements to infer about conditions of the mantle and geophysics characteristics. The propagation of different types of waves allows establishing, per example, the types of rocks and cracks at the Earth's crust. Each type of mineral generally possesses anisotropic characteristics formed by what is called crystal lattice structures. A description of hexagonal, tetragonal and orthorhombic formulation and their application for the analysis of crystals at the Earth crust can be found in Chevrot and Browaeys, 2004. They explain the symmetries of minerals and how the 21-dimensional vectorial space of the elastic tensor is projected into subspaces to break it into specific types of tensors.

For this study, the only concern is to distinguish the isotropic and a non-isotropic part and to establish a percentage value of anisotropy caused by cracks:

$$C_{anisotropic} = C_{isotropic} + \underbrace{C_{hexagonal} + C_{tetragonal} + C_{orthorhombic}}_{C_{non-isotropic}} \tag{2.69}$$

The decomposition, considering a vectorial representation of the tensors as $\vec{X}$, allows extracting the norm $N(\vec{X})$ of each one to compute a related percentage of the material/mineral under analysis, as presented in Equation 2.70. Enstatite and Olivine minerals, e.g., are described 79.3% and 90.8% isotropic, respectively [Chevrot and Browaeys, 2004].

$$100\% = N^{-2}(\vec{X}) \cdot \left[N^2(\overrightarrow{X_{iso}}) + N^2(\overrightarrow{X_{hex}}) + N^2(\overrightarrow{X_{tetra}}) + N^2(\overrightarrow{X_{ortho}})\right] \tag{2.70}$$

2.6 Discretization of the Continuum

According to Krajcinovic, 1996, two large groups of studies can be applied to analyze damage in quasi-fragile materials. One is related to the classical approach, the continuum mechanics; the other is related to statistical models. The former encounter problems regarding scale effect and damage localization while the latter loses versatility, such as the finite element method. However, it solves the localization issue and also accounts for the anisotropic damage more efficiently. The Lattice Discrete Element Method (LDEM) is one of the formulations that

can use statistical formulation. The solid body is described as an interconnected web of uniaxial elements where the masses are located at the nodes. The stiffness of each of these uniaxial elements is correlated directly with the solid material properties. Different approaches than the one applied in this work using LDEM can be found in Krajcinovic and Vujosevic, 1998, Sagar and Prasad, 2009, Nagy et al.,2010, Schalanger,1995 and Rinaldi, 2011. Some interesting results were presented in Chapter 2.4. The line elements yield a force field among the nodes that hold them together, but they are not per se physical. The fracture is characterized in these cases as the result of an extreme reduction of the forces among nodes.

Another approach establishes a discrete particle method where the body is divided into many cells described with individual central nodes. Equations of continuum mechanics are incorporated, where a point x of the body interacts with the surrounding neighbor points x' within a finite distance. Therefore, any point is connected to others by bonds that can be described with peridynamic balance equations proposed by Silling et al., 2007. This assumption extends the formulation for a nonlocal approach, i.e., the mechanical effects at a given point are not only related to zero distance length but within a region limited by a "horizon." A broader view about this matter, and other possible forms to deal with damage/fracture analysis, is addressed in Chapter 2.7 to demonstrate how a specific problem can be deal with. In the following subsection, the chosen Discrete Model is depicted.

2.6.1 Discrete Model Applied in the Present Work

Riera,1984 [apud. Rodrigues, 2015] proposed the lattice model applied as the base in this work. The model was used with great success to determine dynamic responses in concrete plates and shells under impact scenarios [Riera and Iturrioz, 1995, 1998]. Later it was implemented in other studies such as the scale effect in concrete [Rios and Riera, 2004], fracture parameter calculation in dynamic and static problems [Kosteski et al., 2011, 2012] and the studies regarding fragile material resistance at high strain rate [Riera et al., 2011].

The LDEM is based on a cubic arrangement with uniaxial element assuming a truss structure, therefore only with three degrees of freedom. The basic module can be described with twenty bars and nine nodes conceived initially by Nayfeh and Hefzy, 1978 (Figure 2.23). The problems regarding dynamic issues assume the masses concentrated at the nodes where the central node has half of the total mass, while each one of the remaining eight nodes has one-sixteenth of the total mass of the representative cube. They initially used this model to create a

transformation system of the truss-like structure into a continuum media trying to avoid the handling of vast quantities of degrees of freedom such as large periodic panels and shelters.

Hayashi, 1982 introduced a reversed process where the continuum is transformed into a truss structure. The connections among the nodes are through links (bars) under compression and traction only. All the elements have the same Young Modulus, but the length and area of the diagonal and normal bars differ from each other. The normal elements (A_n – blue in Figure 2.23) are defined by six elements connected to the central node and twelve elements at the corners. The diagonal links (A_d – red in Figure 2.23) are defined by eight segments.

Using this configuration, Hayashi, 1982 and Batista, 2007 demonstrated the contribution of each bar for a representative constitutive tensor. If the domain is considered isotropic, the stiffness matrix can be defined as described in Expression 2.71 and 2.72. The diagonal bars with a cross-section A_d, the normal bars with a cross-section A_n along with the cube length L, Poisson's ratio ϑ and the material Young's modulus E, can adequately describe the isotropic stiffness tensor when the Poisson's ratio ϑ is equal to 0.25. Comparing Equation 2.71 with an isotropic stiffness tensor, it will be possible to visualize the difference when the Poisson's ratio changes from 0.25. The diagonal terms no longer support the compatibility between the continuum and the truss-like model.

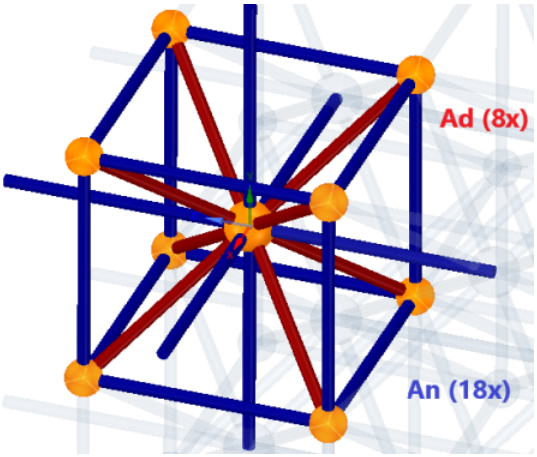

Figure 2.23 - Basic block of the Discrete Element Model applied for the present work. Initially proposed by Nayfeh and Hefzy, 1978.

$$C_{ab} = \frac{2 \cdot E \cdot A_n}{L^2} \begin{pmatrix} 1+\frac{4}{9}\delta & \frac{4}{9}\delta & \frac{4}{9}\delta & 0 & 0 & 0 \\ \frac{4}{9}\delta & 1+\frac{4}{9}\delta & \frac{4}{9}\delta & 0 & 0 & 0 \\ \frac{4}{9}\delta & \frac{4}{9}\delta & 1+\frac{4}{9}\delta & 0 & 0 & 0 \\ 0 & 0 & 0 & \frac{4}{9}\delta & 0 & 0 \\ 0 & 0 & 0 & 0 & \frac{4}{9}\delta & 0 \\ 0 & 0 & 0 & 0 & 0 & \frac{4}{9}\delta \end{pmatrix} \tag{2.71}$$

$$\delta = \frac{9 \cdot \vartheta}{4 - 8 \cdot \vartheta} \qquad A_n = \frac{L^2 \cdot (9 + 8 \cdot \delta)}{2 \cdot (9 + 12 \cdot \delta)} \qquad A_d = \frac{2 \cdot \delta \cdot A_n}{\sqrt{3}} \tag{2.72}$$

Kosteski, 2012 shows the comparison between this LDEM configuration and the continuum applying shear stress. For example, the theoretical and simulated shear modulus G are presented in Figure 2.24. In the scenario of materials with large differences in the Poisson's ratio, the current LDEM configuration is no longer supported and an alternative structure must be considered. However, the Poisson's ratio has typically little influence on the damage and fracture mechanics, considering that in the vicinity of collapse, the isotropy is lost. More comments about this effect can be found in Rinaldi et al., 2008 and Iturrioz, 1995.

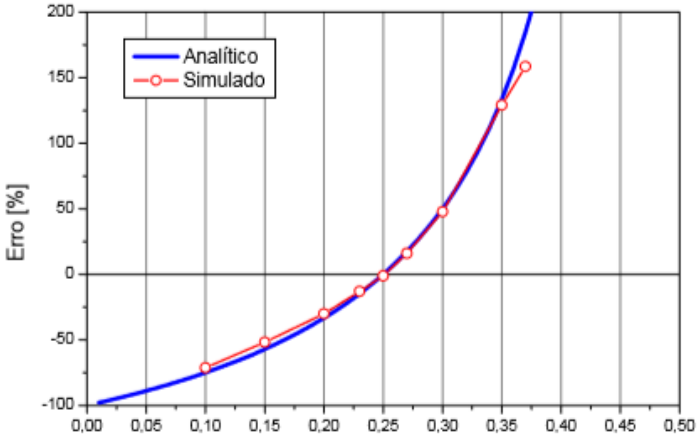

Figure 2.24 - Poisson's ratio ϑ influence on the shear modulus G when the values moves from 0.25. The blue is the analytical solution and the red one is the simulated LDEM under shear load. [Kosteski, 2012]

The expansion and connection of the primary cubic cell presented in Figure 2.23 enable us to achieve the desired geometry. Figure 2.25 shows a set of 4 x 3 x 2 cubic cells with only the first layer highlighted for visualization convenience. Nevertheless, when the total thickness is equal to one, solutions and simulation at plane strain (PSN) or plane stress (PSS) can be performed constraining the displacement of the nodes according to the two-dimensional assumption.

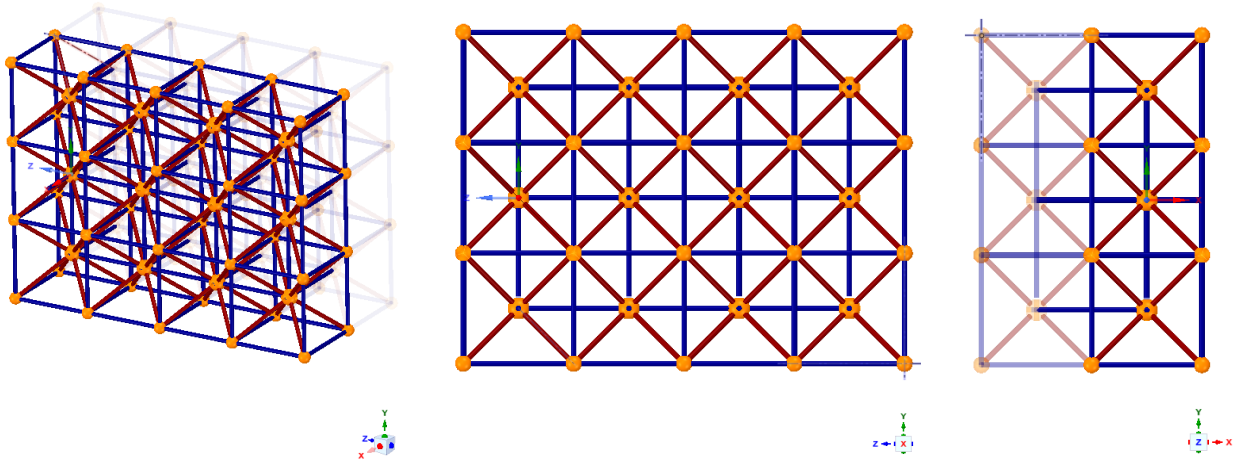

Figure 2.25 - Combination of basic unity cubes to form the desired geometry to simulated the continuum under the discrete distribution of nodes connected by links.

As can be seen, the use of LDEM vastly increases the capacity to reduce the number of degrees of freedom of a body under analysis. This allows us to apply, e.g., the Finite Difference Method to solve an uncoupled system of Differential Motion Equations. The mass matrix M and damping matrix C are typically set diagonal, which makes it possible to integrate the system of n equations over time. However, the damping values are tricky to be defined due to the necessity to account for the numerical stability, the unknown material damping and the constraint of high natural frequencies. Iturrioz, 1995, developed some arguments involving this issue.

Equation 2.73 shows the motion equation in the matrix form, where the right side represents the differences between the internal and external forces at each node. For the integration scheme to converge, the Courant-Friedrichs-Lewy criterion [Bathe, 1996] defines the maximum allowed time increment based on the material density ρ, elastic modulus E and side length L. The system is uncoupled and a central finite differences approach can be applied to integrate the motion equation over the time domain. The nodal coordinates are updated at each time-step, which allows large displacements to be accounted for naturally.

$$\begin{pmatrix} M_1 & \cdots & 0 \\ \vdots & \ddots & \vdots \\ 0 & \cdots & M_n \end{pmatrix} \cdot \frac{d^2}{dt^2} \begin{pmatrix} x_1(t) \\ \vdots \\ x_n(t) \end{pmatrix} + \begin{pmatrix} C_1 & \cdots & 0 \\ \vdots & \ddots & \vdots \\ 0 & \cdots & C_n \end{pmatrix} \cdot \frac{d}{dt} \begin{pmatrix} x_1(t) \\ \vdots \\ x_n(t) \end{pmatrix} = \Delta \begin{pmatrix} f_1(t) \\ \vdots \\ f_n(t) \end{pmatrix}, \Delta t \leq \frac{0.6L}{\sqrt{\frac{E}{\rho}}} \qquad (2.73)$$

Back to the damage considerations, which is the main focus of this work, an association between the damage release energy of the continuum and the LDEM model must be provided. The relation between both approaches must be equal, which means that the energy necessary to divide the representative volume in a specific direction completely must be the same using the continuum mechanics and the LDEM model. The continuum evaluation considers Griffith's parameter G established by the relation $\Gamma = G\ {L_n}^2$. However, for the LDEM model, the energy equation must take into account the area of the bars as presented in the box "Areas" in Figure 2.26. For the diagonal links, the areas are described by the diagonal length L_d and for the normal links L_n.

A factor called C_a is defined to establish the equality between both the aforementioned energy entities ($\Gamma = \Gamma_{LDEM}$). The relation which defines C_a must be equal to 3/22 to guarantee such equality. Due to this weighting coefficient, an equivalent fracture area A^f of each one of the elements of the cube is prescribed relating it with the length L_n. As will be later presented, the fracture area will be used to predict the moment where the rupture will occur according to a certain degree of strain.

Also, a constitutive law must be defined to establish the behavior between stress/force and strain at each bar (F – ε) to introduce these solutions for an appropriate evaluation of the LDEM model.

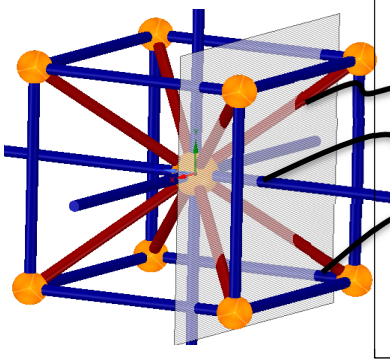

Areas of:

$4\ x\ L_d$

$1\ x\ L_n$

$4\ x\ \left(\frac{1}{4}\right)\ L_n$

Energy balance:

$$\Gamma_{LDEM} = G \cdot \left(\underbrace{4 \cdot \left(\frac{1}{4}\right)}_{1\ x\ L_n} + \underbrace{1}_{1\ x\ L_n} + \underbrace{\left(4 \cdot \frac{1}{\sqrt{3}}\right)^2}_{4\ x\ L_d} \right) {A_n}^f$$

$\Gamma = G\ {L_n}^2$ and $\Gamma_{LDEM} = \Gamma$

Leads to:

$${A_n}^f = \left(\frac{3}{22}\right) {L_n}^2 \quad {A_d}^f = \left(\frac{4}{22}\right) {L_n}^2 \quad C_a = \frac{3}{22}$$

Figure 2.26 – The box "Energy balance" defines the equality between the continuum and the LDEM model ($\Gamma = \Gamma_{LDEM}$). The set of equations inside box "Areas" defines the normal A_n and diagonal areas A_d as a function of the side length L_n.

The definition of the constitutive law for quasi-brittle materials was initially considered by Hillerborg et al., 1976. The crack propagates when the stress at the crack tip assumes a tensile strength f_t according to Figure 2.27a. But, the stress must not fall to zero at once. Instead, it must decrease with increasing crack width w (same as parameter a in other sections). Before reaching the noncritical crack width, the defect, in reality, corresponds to a micro cracked zone with some remaining ligaments for stress transfer. The experiments conducted by Evans and Marathe, 1968 in concrete specimens have shown that a bilinear curve would be a reasonable prediction for quasi-brittle materials (Figure 2.27c).

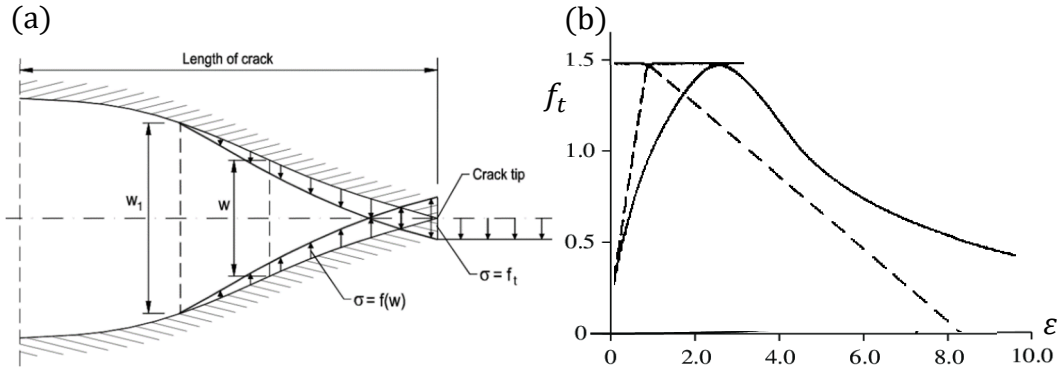

Figure 2.27 – (a) Crack opening considerations used by Hillerborg et al., 1976. (b) There is a decreasing force necessary to open the crack as the energy release rate can be lower as the crack increases. Concrete experiment showing the force x strain relation as the damage builds up. The dotted line is the bilinear simplification. [Evans and Marathe, 1968]

Therefore, it is possible to describe this bilinear behavior based on the critical strain ε_p and collapse strain ε_r. The critical strain ε_p establishes the beginning of the damage process, while the collapse strain ε_r defines the complete loss of stiffness of the normal or diagonal bars. This law also specifies that the damage at each bar only occurs during traction, maintaining the undamaged stiffness during compression. During traction loading increments, a critical load P_{cr} defines a maximum value related to ε_p (Figure 2.28). In a strain-controlled process, when the strain surpasses ε_p, there is a reduction in the maximum load permitted. The unloading process always follows the path of the last load case returning to the origin of the system F – ε. In other words, there is no residual or plastic strain after unloading.

Any strain larger than ε_p will result in a reduction in stiffness and increments in the released energy. When the fracture strain is reached (ε_r) the components no longer maintains any resistance and the damage is complete. At this moment, equality between the area below

the curve and the energy released must be set according to the critical area of the links ($A_n{}^f$ or $A_d{}^f$), as previously shown in Figure 2.26. Equation 2.74 derives the area below the curve where the term i can assume the normal (n) or diagonal (d) bar. Figure 2.28b shows graphically this expression.

$$\int_o^{\varepsilon_r} F(\varepsilon)\, d\varepsilon = \frac{G_c \cdot A_{\mathrm{i}}{}^f}{L_{\mathrm{i}}} \tag{2.74}$$

The quasi-brittle system, in this proposition, disregards the residual strain during unloading, but with a little adjustment, the definition of other constitutive laws can be made according to different material properties. Other constitutive laws, such as a trilinear approach, can be found in Kosteski, 2012. For compression load, the constitutive law considers the maintenance of the initial stiffness due to the characteristic of the quasi-brittle materials to withstand many times the ultimate traction when in compression. The theoretical formulation of this constitutive law is described more precisely in Rocha et al., 1991, Dalguer et al., 2003 and Iturrioz et al., 2009.

The critical fracture energy $\mathrm{G_c}$ is defined by the inelastic zone described in Figure 2.28. The factor k_r is introduced to account for the ratio between ε_r and ε_p leading to a factor that controls the softening process. The relations and formulation are here recovered from chapter 2, as the terms G_c, σ_c, crack size a, K_c and the nondimensional factor dependent on geometry Y.

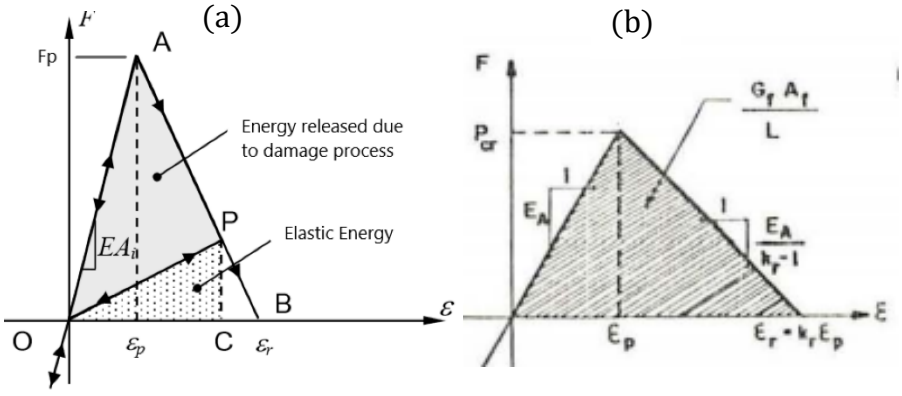

Figure 2.28 - (a) Energy released during damage and Elastic energy recovered after unloading in the path OAB [Iturrioz et al., 2009]. (b) The final energy released after rupture. [Dalguer et al. 2003]

Equation 2.75 and 2.76 leads to a relation between ε_p and G_c. The term R_{ff} is called a failure factor and is associated with the crack size. Maintaining the G_c and E constants, which means the area below the curve in Figure 2.28 must be kept unchanged, the increasing failure factor R_{ff} will increase ε_p. This means a tendency to the fragile behavior as the maximum force F_p increases. Conversely, as R_{ff} tends to zero, a ductile behavior starts to be more distinct. It is also important to realize that the defect is an intrinsic feature and is associated with the material properties through the G_c variations.

$$G_c = \frac{{K_c}^2}{E(1-\vartheta^2)} = \frac{(Y\sigma_c\sqrt{a})^2}{E(1-\vartheta^2)} = \frac{(Y\cdot E\cdot\varepsilon_p\sqrt{a})^2}{E(1-\vartheta^2)} \tag{2.75}$$

$$\varepsilon_p = \frac{1}{Y\sqrt{a}}\sqrt{\frac{G_c}{E(1-\vartheta^2)}} = R_{ff}\sqrt{\frac{G_c}{E(1-\vartheta^2)}} \tag{2.76}$$

The equivalent fracture area ${A_{n\,or\,d}}^f$ and the real area $A_{n\,or\,d}$ can also be related using the energy relation from Equation 2.74. This leads to a definition of the factor k_r by the material and geometric properties. Inverting Equation 2.77, a relationship for a critical length also can be found.

$$k_r = \frac{\varepsilon_r}{\varepsilon_p} = \underbrace{\frac{2\cdot {A_{n\,or\,d}}^f}{L_{n\,or\,d}\cdot A_{n\,or\,d}}}_{geometry}\cdot\underbrace{\frac{G_c}{E\cdot\varepsilon_p^2}}_{material} \tag{2.77}$$

The stability is assumed when the condition $k_r \geq 1$. Using Equation 2.77, the Poisson's ratio of 0.25 and the relations from Figure 2.26, it is possible to derive a critical area in which the damage is complete [Riera and Rocha, 1991].:

$${A_{n\,or\,d}}^f \cong 0.34\cdot A_{n\,or\,d} \tag{2.78}$$

All the Equations outlined a material or geometric properties dependency. The only constants which are purely material properties are G_c and E. The others are dependent on the dimension of the cubic cell or also dependent of the material.

One of the main advantages of the LDEM is the possibility to introduced variability at any parameter, which means properties fluctuations spatially. At any given point of the structure under analysis, a different response will be provided depending on the random function and settings used. This type of procedure tries to mimic the real structures and their intrinsic heterogeneity. The simplest and ingenious form is choosing the parameter G_c due to its relation with the Linear Elastic Fracture Mechanics and the direct association with K_c. The random distribution of G_c will yield an uneven resistance throughout the volume. Rocha, 1989 introduced the simplest form of variation. The probability function of G_c is a two-parameter Weibull function. β and γ are scale and form parameters in Equation 2.79, respectively. The parameter p is the probability density varying between 0 and 1, which can determine the variation of the fracture energy.

$$F(G_c) = 1 - \exp\left[\left(-\frac{{G_c}^{\gamma}}{\beta}\right)\right], \qquad G_c = \beta\,[-\ln(1-p)]^{\frac{1}{\gamma}} \tag{2.79}$$

From these probability function, a definition of an average value $\overline{G_c}$ and its standard deviation σ_{Gc} can be made. Additionally, another probability function called Gama function Γ_{gf} which is not presented in this work [see Rocha, 1989] must be added in order to obtain the coefficient of variation of the critical release energy $CV(G_c)$. Parameter φ, similarly to parameter p, is a random value that defines the deviation from the average by defining two other constants:

$$G_c = \varphi \cdot \overline{G_c} = \frac{\beta \cdot [-\ln(1-p)]^{\frac{1}{\gamma}}}{\beta \cdot \Gamma_{gf}(1+\frac{1}{\gamma})} \cdot \overline{G_c} \tag{2.80}$$

$$CV(G_c) = \frac{\sigma_{Gc}}{\overline{G_c}} = \frac{[\Gamma_{gf}\left(1+\frac{2}{\gamma}\right) - {\Gamma_{gf}}^2\left(1+\frac{1}{\gamma}\right)]^{1/2}}{\Gamma_{gf}(1+\frac{1}{\gamma})} \tag{2.81}$$

It is straightforward to notice this random process observing Figure 2.29. The variation of G_c are based on $\overline{G_c}$ and parameter φ . The effects are shown in Figure 2.29b where p_{cr} and ε_p will be affected by the random distribution of G_c. The impact of the parameter φ in $CV(G_c)$ is also presented in Figure 2.29c as an example of the relation between both entities.

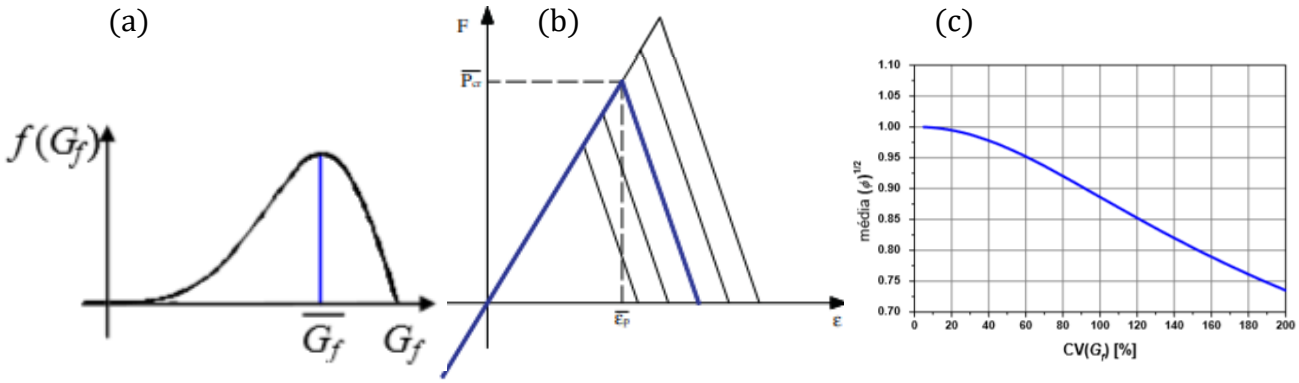

Figure 2.29 – (a) Weibull distribution considering an average value G_c [Kosteski, 2012]. (b) The effects of the coefficient of variation $CV(G_c)$ on the p_{cr} and ε_p adding an aleatory variability of properties at each bar [Iturrioz et al., 2013]. (c) An example of the relation of the chosen φ and $CV(G_c)$. [Kosteski, 2012]

2.7 Last Developments – State of the Art

2.7.1 Damage/Fracture Studies

In this chapter, a few of the latest developments in terms of damage/fracture studies are depicted. The reader interested will find here many possible paths available nowadays to evaluate any given structure. The concepts described in Chapter 2.1 (Fracture Mechanics), Chapter 2.2 (continuum damage mechanics - CDM), Chapter 2.3 (Micromechanics) and Chapter 2.6 (discrete element models – DEM) are the set of essential knowledge for the development of consistent theories capable of reproducing the behavior of real structures. Due to the vast field of application, this overview will focus mainly on the latest studies in fragile/quasi-fragile materials.

The application of Finite Element Analysis (FEA) is one of the most spread numerical tools to study structural resistance when dealing with continuum mechanics. Nowadays, the use of this technique in fragile materials typically considers concepts of CDM and plasticity theories to obtain consistent results between numerical and experimental results. Countless works have been developed in the last decades contributing to the analysis of concretes, fragile and other quasi-fragile materials.

Many of these works base their results on the behavior of concrete specimens studied by Kupter et al., 1969 through biaxial and inelastic deformation experiments. Numerical proposals as the one reviewed by Papanikolau and Kappos, 2007 adds a constitutive model for

concrete in a triaxial compression state. They were capable of describing the material behavior with a non-associated flow rule, but they disregarded the cumulative material properties degradation, i.e., damage parameters are not addressed. Richard et al., 2010, among others, coupled the damage and loss of stiffness and assumed a single scalar entity to represent the plastic behavior. The numerical results fit approximately when compared to cyclic loading experiments. However, irreversible deformation and the volume expansion in compression were not accounted for in those works. Lately, a general and compatible form to deal with damage and plasticity have been developed to meet more diverse experimental outcomes. The works of Wu et al., 2005, Sarikaya et al., 2019 and Richard et al., 2013 can be cited as good numerical plastic-damage models mimicking the concrete behavior in different geometries considering cyclic and monotonic loading conditions.

Another interesting numerical proposal, which formulates an anisotropic continuum damage model, is developed by Brunig and Michalski, 2017. It introduces the damage law and plastification process as separate entities to evaluate the process until the moment before the fracture. The experimental results are reported in Brunig and Michalski, 2019, where specimens of concrete under compression are analyzed. The numerical prediction is based on equivalent damage strains and stress triaxiliaties to evaluate the onset of failure. Figure 2.30 shows the stress/strain state at the onset of fracture for a cubic specimen under compression. Obviously, the crack growth and fracture cannot be simulated, considering only this approach. These features can only be achieved with the addition of numerical techniques and fracture criteria, which limits the application of a pure FEA-based procedure.

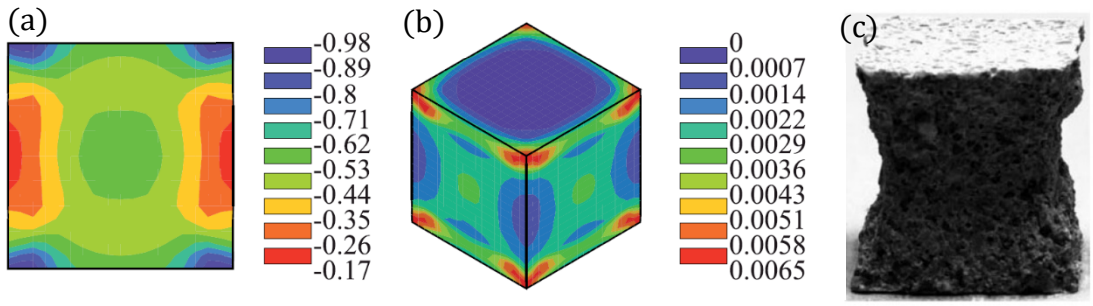

Figure 2.30 - (a) Mid-section stresses triaxiality and (b) isometric damage strain representation at the onset of failure. (c) the cracked block corresponds to regions of max. and min. of stress/strain values. Compression simulation. [Brunig and Michalski, 2019]

We can naturally observe that the description of discontinuities in finite elements is not suitable to represent entities such as cracks. FEA models are based on a piecewise differentiable polynomial, generally causing the collapse of the function at the fracture's tip. An extended

version of the finite element method (X-FEM) was proposed by Belytzscho and Black, 1999, to deal with such a problem. The proposal intended to create a technique to evaluate the fractured region without the need of mesh refinement or the need for a mesh that conforms with the discontinuities. Typically four different types of elements are necessary for the X-FEM scheme: the standard FEA elements (white), the fully split elements (blue), the crack tip elements (red) and the blended element (green) - Figure 2.31a. The formulation addressing the displacement field has different forms according to the element type, but the basic proposal adds the so-called enrichment functions to the standard finite element approximation and deals with the discontinuity applying the Heaviside jump functions. This methodology allows the cracks to propagate autonomously regardless of the mesh topology. However, the numerical integration of the cut elements persists along the crack and at the singularity. Some interesting solutions to mitigate these problems were presented by Ventura, 2006.

The X-FEM method also couple with other methods such as the Level Set Method (LSM - see Osger and Sethian, 1988). The combination X-FEM/LSM was first analyzed for the crack growth in two dimensions by Solarska et al., 2001. Additionally, a specific type of Level Set Method, called Fast Marching Method (FMM), was proposed to deal with three-dimensional problems. The reader interested can find profuse works in this context in Chopp et al., 2003, Sukumar et al., 2003 and 2008. Many other references applying X-FEM analysis can be found in Yazid et al. 2009.

Specifically dealing with quasi-fragile materials, it can be pointed out the works of Bobinski and Tejchman, 2013 and 2016. They analyzed the crack propagation in concrete, applying plastic and isotropic damage model to compare simulation and experimental bidimensional cases. In the case of 3D applications, the models must be much more complex to deal with different problems that arise from the numerical solution. Therefore, generally in these cases, a non-local damage solution must be addressed (see Voyiadjis et al., 2008). Javanmardi et al., 2019 combines 3D modeling, anisotropic damage plasticity, non-associative flow rule and a new directional crack propagation criterion with different material degradation components. In this study, the crack tip only grows element by element, i.e., the crack cannot be placed inside the element. A critical damage level (>0.5) is set to determine the moment where the crack initiates. An example comparing the adjusted numerical solution with experimental ones in given in Figure 2.31b. A shear double-notched test applied in a concrete model with a 10kN load obtaining similar patterns for the crack propagation. Other load values also demonstrate good agreement between numerical and experimental results.

It is essential to point out that the X-FEM methodology always has to add many theories and, intrinsically, complicate the analysis of the problem. The literature shows a vast quantity of models with a different combination of models trying to mimic the crack initiation and growth direction.

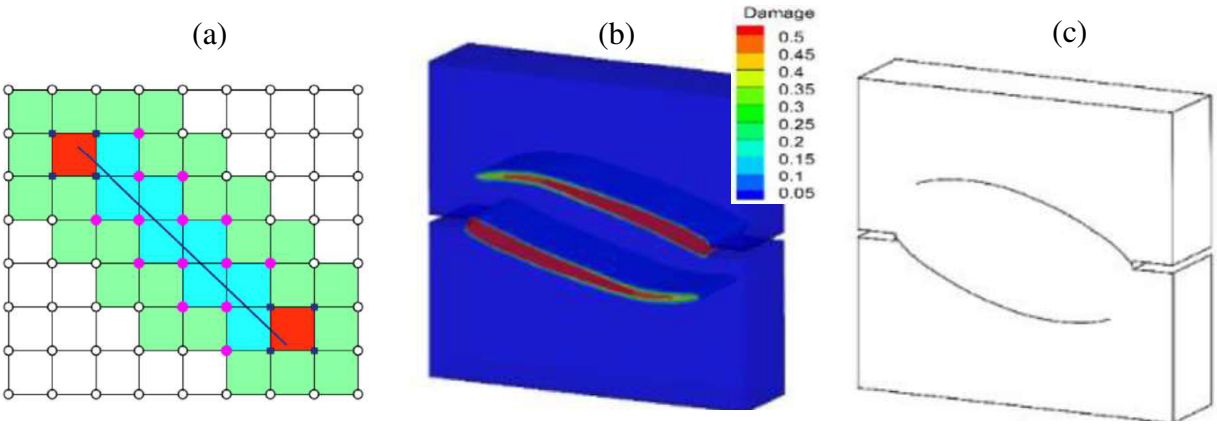

Figure 2.31 – (a) Types of elements in a standard X-FEM model. White: normal FEA element. Blue: Fully split element. Red: crack tip element. Green: Blended element. (b) Damaged elements during a non-local/X-FEM model at the end of the simulation [Javanmardi et al. 2019]. (c) experimental results from similar conditions for 10kN shear load.

Other approaches, as the discrete models commented in Section 2.6, can be more suitable to address the transition damage-fracture. Besides the Lattice model (LDEM) explicitly described in Section 2.6.1, and applied in the present work, other formulations are widely studied nowadays.

An interesting method, develop by Silling, 1999, has shown a form to provide a link between the molecular dynamics and the continuum mechanics. The so-called peridynamic theory replaces equations of the continuum medium, which are spatial displacement derivatives, by an integral form. The formulation is capable of predicting the damage initiation and also the propagation. The peridynamic model (PD) is a nonlocal method, where a specific material point X is bonded with other points around it. A parameter called horizon (δ) prescribes the range at which the forces of the node X affects. Normally the horizon circle H_x is set at $3L_{pd}$, where L_{pd} is the distance between two consecutive nodes around the X point. Figure 2.32a shows the description of these parameters. Each link follows relations between force and strain. Therefore, a limit stretch defines a ruptured bond at which the force between two given points reaches zero and it generates the necessity to redistribute the force to the other links. The simulation is conducted in the time domain with small increments in time-step to observe the loss of stiffness of individual connections and the rearrangements of the force field. A way of establishing the

damage parameter is to define the ratio of bonds loss inside the horizon by the total initial undamaged bonds. The critical stretch is typically computed based on the critical energy release rate G_c, material properties and horizon size [see Madenci et al., 2014]

In the study conducted by Anbarlooie et al., 2019, the microstructure of a dual-phase material (DP), composed of martensite and ferrite, is simulated during a quasi-static loading. The simulations try to mimic the real plane strain conditions of experimental procedures and it is based on real SEM images (scanning electron microscopy), as shown in Figure 2.32b. Therefore, the Control Volume is a heterogeneous medium in the meso-scale. The study considers two separate scenarios. The first analyzes the effect of the number of material points, i.e., the degree of discretization of the domain. Secondly, a study on the impact of the chosen material property at the interface between martensite and ferrite is carried out. Despite different outcomes, in all simulation, the damage necessarily initiates at the boundaries and it always propagates at the soft material (ferrite) as observed experimentally (Figure 2.32c). The microcracks created in different points will eventually coalesce recreating patterns of fracture, which are also found in real materials.

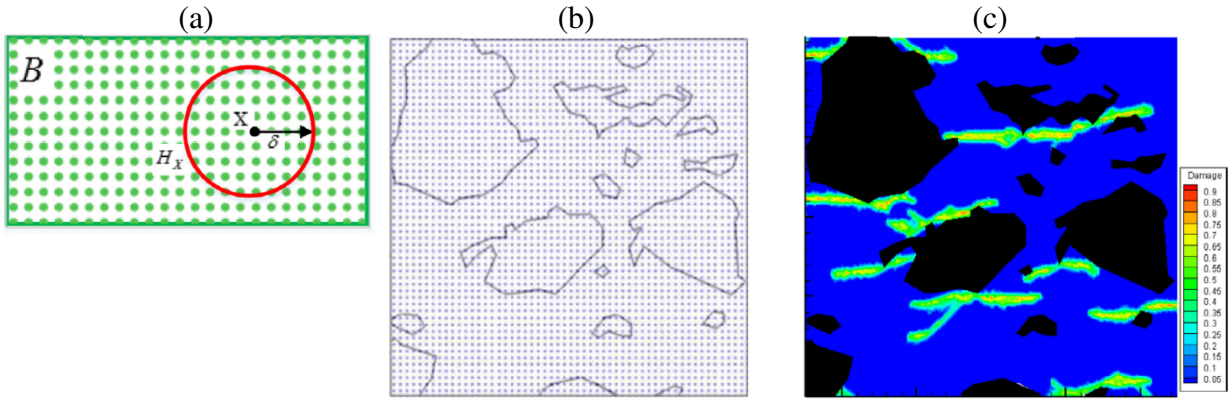

Figure 2.32 - (a) The definition of horizon for the point X in a certain domain. (b)Discretization of the dual-phase structure. (c) An example of the damage level in the simulated domain [Anbarlooie et al., 2019].

Another author, Mehrmashhadi et al., 2019 applied the peridynamic technique to evaluate the transverse fracture behavior of fiber-reinforced composites (FRCs) using an intermediately-homogenized (IH) and a fully-homogenized (FH) formulation according to a non-uniform mesh, where the nodes can represent different sizes of areas, similar to finite element meshing process, where the centroid of the element is defined with the representative node. Therefore, complex geometry can be better represented. The two approaches (FH and IH) have different characterizations for the microstructural description. The FH model

describes all the bonds applying the Halpin-Tsai technique, where an averaging procedure is taken using the properties of the fiber and matrix (resin). On the other side, the IH approach considers three different types of bonds linking matrix-matrix, fiber-fiber and fiber-matrix nodes. In this case, the fiber-matrix links are also defined by an averaging procedure. The bonds for a particular node X assume a stochastic distribution according to the volume fraction of each type of bond. Three-point bending tests (mouth opening displacement – CMOD) were conducted to compare these numerical solutions with experimental ones considering a specific E-glass composite. Figure 2.33 presents the results. In both scenarios, there is a convergence with the horizon size decrement and the results are quite similar to experimental ones, also providing similar crack paths, especially using the IH peridynamic (IH-PD) criterion.

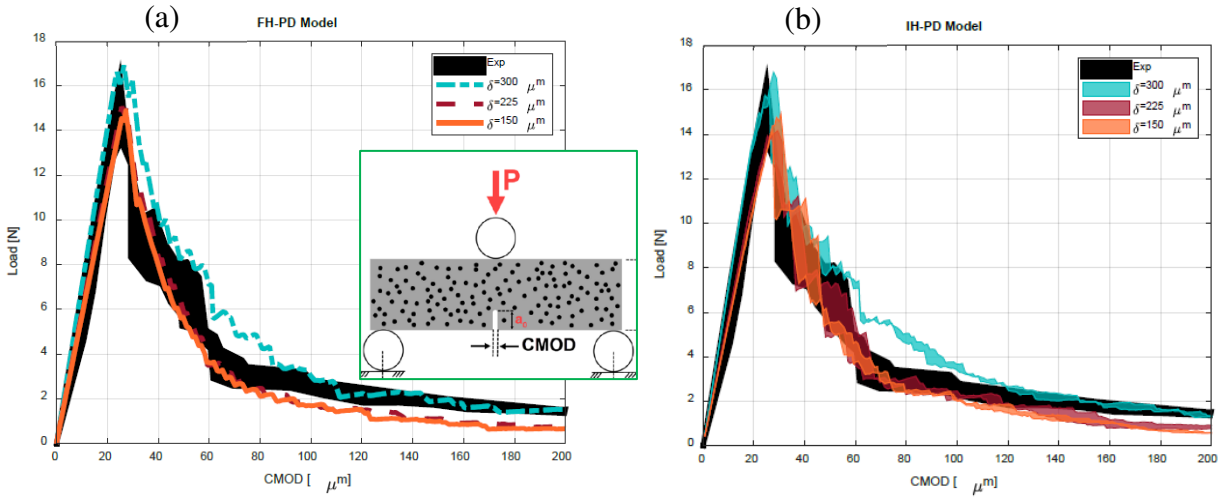

Figure 2.33 – (a) FH case. Experimental (black) and different horizon sizes for the numerical analysis. (b) The same plot for the IH scheme. Three-point bending test evaluating the "mouth" opening (CMOD). [Mehrmashhadi et al, 2019]

It can be pointed out similar studies conducted to compare experimental and numerical concrete structures. The works of Gerstle et al., 2007 and Yaghoobi and Chorzepa, 2017 are examples of how the peridynamic model can provide satisfactory results considering quasi-brittle materials.

Another form to apply a DEM model is viewing it as an aggregate of bonded spherical elements. Packs of spheres are connected to each other through springs and dampers equation, which try to mimic the continuum. Typically, the constant and physical relations have to be adjusted according to experimental observations.

Examples of such types of DEM models are applied continuously in concrete analysis under compression or flexural tensile strength test.

Usually, concrete is formed by mortar (matrix), aggregates (inclusion) and an interfacial transition zone (ITZ) that couples the two regions. The ITZ zones typically are the weakest regions due to the presence of porosities and, owing to this fact, they have a primordial contribution for the crack initiation and growth. Nitka and Tejchman, 2020, studied the effect of the ITZ zone using a DEM model in a meso-scale. This type of discrete model considers Newton and Coulomb Laws to address translational and rotational motions between the spherical bodies and an explicit time-stepping integration is used to describe the increasing damage/fracture. In this context, depending on the framework and material involved, different laws and properties need to be adjusted to represent real observations better. Figure 2.34 shows a three-point bending test for a concrete beam with a meso-scale description. The numerical simulation considers the same structure as the experimental one, varying only the ITZ thickness, grain roughness and porosity. Results for 20% porosity at the ITZ zone are shown, where the crack path between the experimental and numerical simulation is considerably similar. Additionally, it was observed that the Force x CMOD graph has very similar behavior.

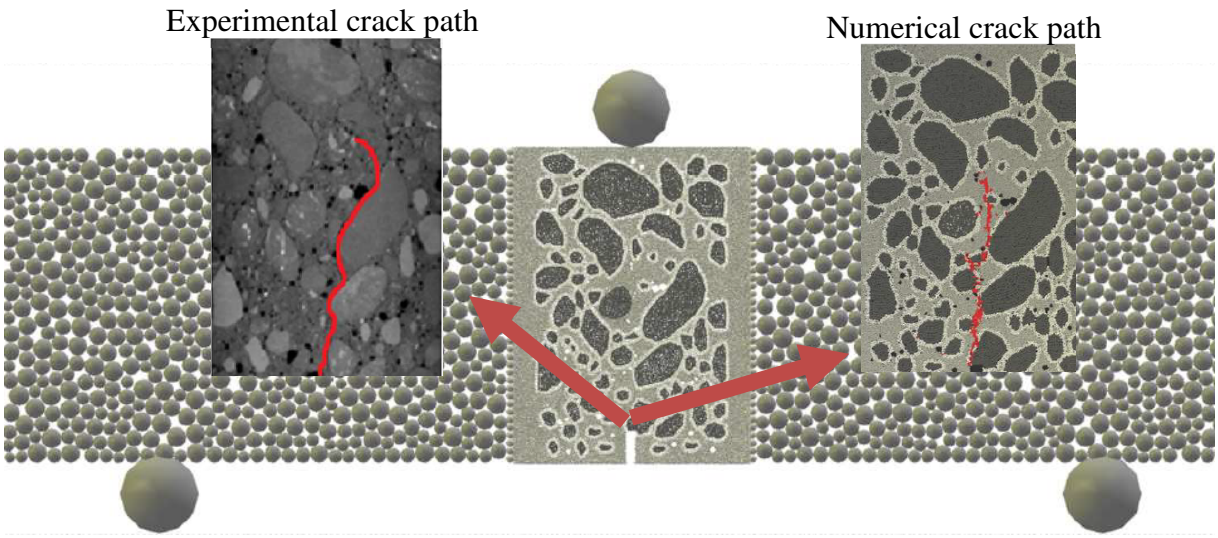

Figure 2.34 – Three-point bending test. Numerical and experimental results. The numerical considers 20% porosity in the ITZ zone. Crack paths are illustrating the similarities between experimental and numerical results. [Nitka and Tejchman, 2020]

Another interesting study conducted by Wang et al., 2020 applies real CT scan images of real concrete aggregates and new displacement-softening law. The influence of the ITZ bond, the aggregate's material properties and the contact law are analyzed for specimens under compression tests obtaining interesting relations between the structure constituents.

Additional to the application in concrete samples, this type of DEM modeling is also ideal for addressing brittle cracks in rocks and minerals. Klichowicz et al. 2018, researched mineral fractures at the grain level while multi-step cracking processes occurred. The author highlights the dependence of the results on many parameters that are difficult to measure, such as the grain bonding strength. These parameters can be adjusted based on observational results, but they are limited by the case under investigation and, therefore, the proposed model does not necessarily will be accurate in other contexts.

Experimental analysis with an in-depth look at the microscale during damage/fracture is needed to support pieces of evidence from numerical ones. Tao et al.,2020 develops an example of such studies., where the effect of the uniaxial and triaxial compressive tests in mafic rocks, observing in-depth the pre-existent microstructural microcracks (intra-granular, inter-granular and multi-granular) and the ones forming during loading After the tests, fragments of the rocks are analyzed applying an image treatment technique based on scanning electron microscope. The process was able to distinguish and the contribution of pre-existing micro-constituents (heterogeneities, crystal lattice boundaries and microcracks). The grain boundaries are the weakest regions where the fracture has a preferential path and, depending on the existing microstructures, the crack propagation will have preferential growth in shear or traction mode (Figure 2.35a and b, respectively). A combination of both modes can be evaluated through scan and image processing observing initiation, propagation, coalescence and rupture of the microstructures. The study managed to define a scalar damage parameter relating these two modes and define the evolution of this entity during the growth of the crack. This type of research is essential to be used as a reference frame during numerical solutions.

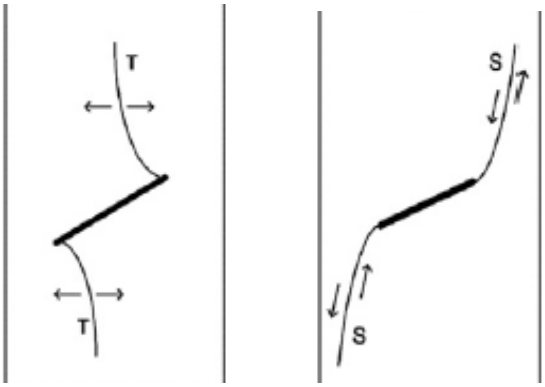

Figure 2.35 - Crack growth of the microstructure. (a) Traction mode. (b) Shear mode. A combination between the modes is possible. The combination of both is possible. [Tao et al., 2020]

2.7.2 RVE-Based Studies

Lately, the implementation of the so-called multi-scale computational modeling has been developed to deal with structures undergoing the nonlinear processes. The aim is to describe the material at several scales, which relates to a macro/microscale or macro/mesoscale problem. Therefore, the internal micro/meso material morphology is replaced by stress/strain constitutive variables at the macroscale. The RVE description arises from this concept and the homogenization has a procedure associated with it. The Hill proposal, discussed and implemented in this work, is the most notorious and conventional form to deal with this multi-scale problem. However, this approach loses consistency typically when the material fails, creating what is called a non-smooth feature embedded at the medium. According to Oliver et al. 2015, the RVE existence can also be questioned in this situation. Many alternatives have been developed in the past decades, posing options for the macro/micro scales analysis. The variational formulation has been widely regarded as a promising approach to this debate. It accounts for a non-smooth behavior at the lower-scale capturing, for example, the crack onset and propagation through a discontinuous micro-displacement field (see Blanco et al., 2014). The entire theory is based on a "physically meaningful" association between macro and micro-scale. Usually, the association between the scales considers high-order continua at macro length, while at the microdomain, a first-order approach is defined. However, besides the solid theoretical grounds of Hill, any attempt to display a well-posed approach to the multi-scale analysis faces uncertainties due to unclear assumptions. The link between the scales is not straightforward and they are also attached to the physical process under investigation.

Blanco et al., 2014, presented an alternative for the multiscale problem through the so-called Method of Multiscale Virtual Power (MMVP). The method keeps the RVE assumption of different scale-order among body, RVE and microscale. One of the main characteristics of the proposed technique is the "kinematical admissibility," which states that the magnitudes of the displacement variables are preserved in the scale transition.

The work of Carazo et al., 2014, is an example of a multiscale approach to evaluate effective macro properties based on digital imaging processing of spherical cast iron micrographs. Applying an averaging technique developed by Giusti et al., 2009, they assessed the impact of the RVE geometry, the graphite fraction, the nodularity and the aspect ratio on the Young's modulus and Poisson's ratio. This approach allowed the author to demonstrate that the geometry of the RVE has little impact on the micromechanical properties. Existing

analytical solutions were compared with the numerical and the viability of such averaging techniques was observed.

2.7.3 Other Methods

The underlying assumptions of the parallel bundle system are depicted in Section 2.4 (Krajcinovic e Silva, 1982) with Equation 2.56, 2.57 and 2.58, introducing the mathematical concepts of this technique. The proposal is based on the Global Sharing Rule (GSR), which means the forces of broken links are shared among the remaining ones. The probability function related to damage in these unidimensional equations can be seen as a microscale disorder that yields a macroscale degradation. The presented formulations are elastic solutions, which means that the global F x d curves are always oriented to the origin of the plot. Rinaldi, 2011 adds to this scenario, components of plasticity to obtain different behavior for more complicated assumptions. A plastic regime with its own dispersion (p_p) adds to the elastic one (p_f). However, as shown in Figure 2.36a, the plastic contribution of the probability function for quasi-fragile materials is dislocated and, therefore, never reached. This interpretation leads to the simplification of the problem avoiding cumbersome issues.

Rinaldi, 2011 shows that the normal evolution from a unidimensional to a 2D/3D model creates a lattice representation that usually applies Delaunay triangularization from a Voronoi approximation of a polycrystalline microstructure. Figure 2.36b shows the process where a Voronoi grain, described as a polygon, is represented by a node (A). The center of each grain is linked to adjacent ones, establishing resistance relationships. The rupture will only be characterized at the borders of the representative Voronoi grain, which solely allows accounting smaller defects through the insertion of random lattice properties. It is important to observe that in this situation, the length of each element has an impact on resistance besides the mechanical properties' variation.

The reader interested in an in-depth look into bundle methods can find profuse material in Hansen et al., 2015. They deepen the study of the variational problem, evaluate the impact of the statistical features and describe methods for predicting failures using classical and advanced bundle models.

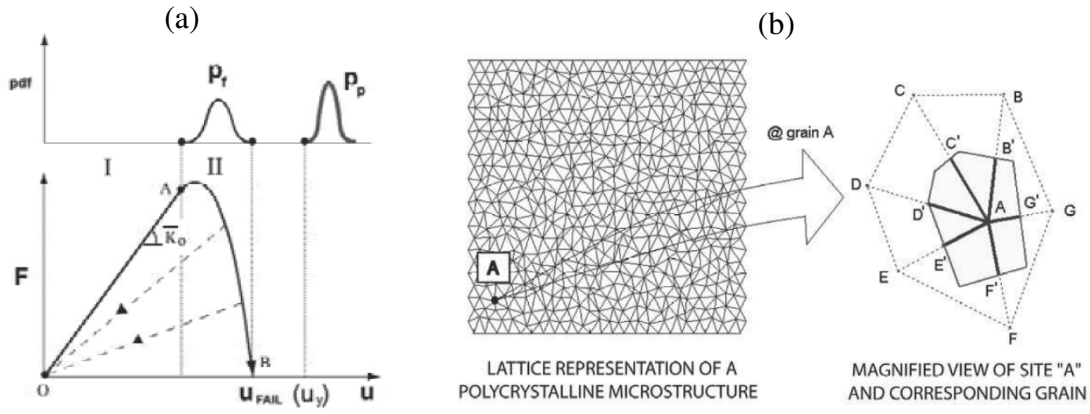

Figure 2.36 – (a) The quasi-brittle materials' failure probability function considering the plastic (p_p) and elastic (p_f) regime. (b) The Delaunay triangularization using the Voronoi grain. Links with different sizes connect the center of different grains (B-G) with grain A. [Rinaldi, 2011]

Another interesting methodology is the so-called "electrical failure analogy of fracture." The electrical phenomenon possesses entities such as voltage, fuse, current, among others, where the variables represent a scalar field, contrary to the mechanical description where the field has a tensorial form. This concept naturally simplifies de material description and avoids many issues regarding tensorial handling. The disorder in the electrical simulation can be modeled as insulators in a conducting material. The embedded nonconducting material modifies the field lines, mimicking the distortion caused by a defect, which is similar to the stress concentration scenario in the mechanical scheme. The current around the crack/nonconducting material will be altered by a certain amount, which is governed by a factor k related to the geometry of the defect. For example, an L x H elliptical form will describe a factor k equals to L/H. This value will affect the local current, which is compared to a critical threshold where the failure starts to evolve. The works of Biswas, 2015 and Chakrabarti and Benguigui, 1997 have a profuse description of how this analogy can be made adding stochastic models to mimic the natural variation of the micro components.

3 DEVELOPMENT

The next Chapters will discuss the methodology and the results of the work into two main parts. The first, called 1st Scenario, will address the comparison between the analytical and numerical responses, while the 2nd Scenario will analyze a cyclic process with no analytical approximation. The following chart links the different sections of the work, guiding the reader for a proper understanding. A paper version (Appendix F) is addressed at the end of this work with the main conclusions and observations. The detailed information is presented in Chapters 3.3 (1st Scenario) and in Chapter 3.4 (2nd Scenario).

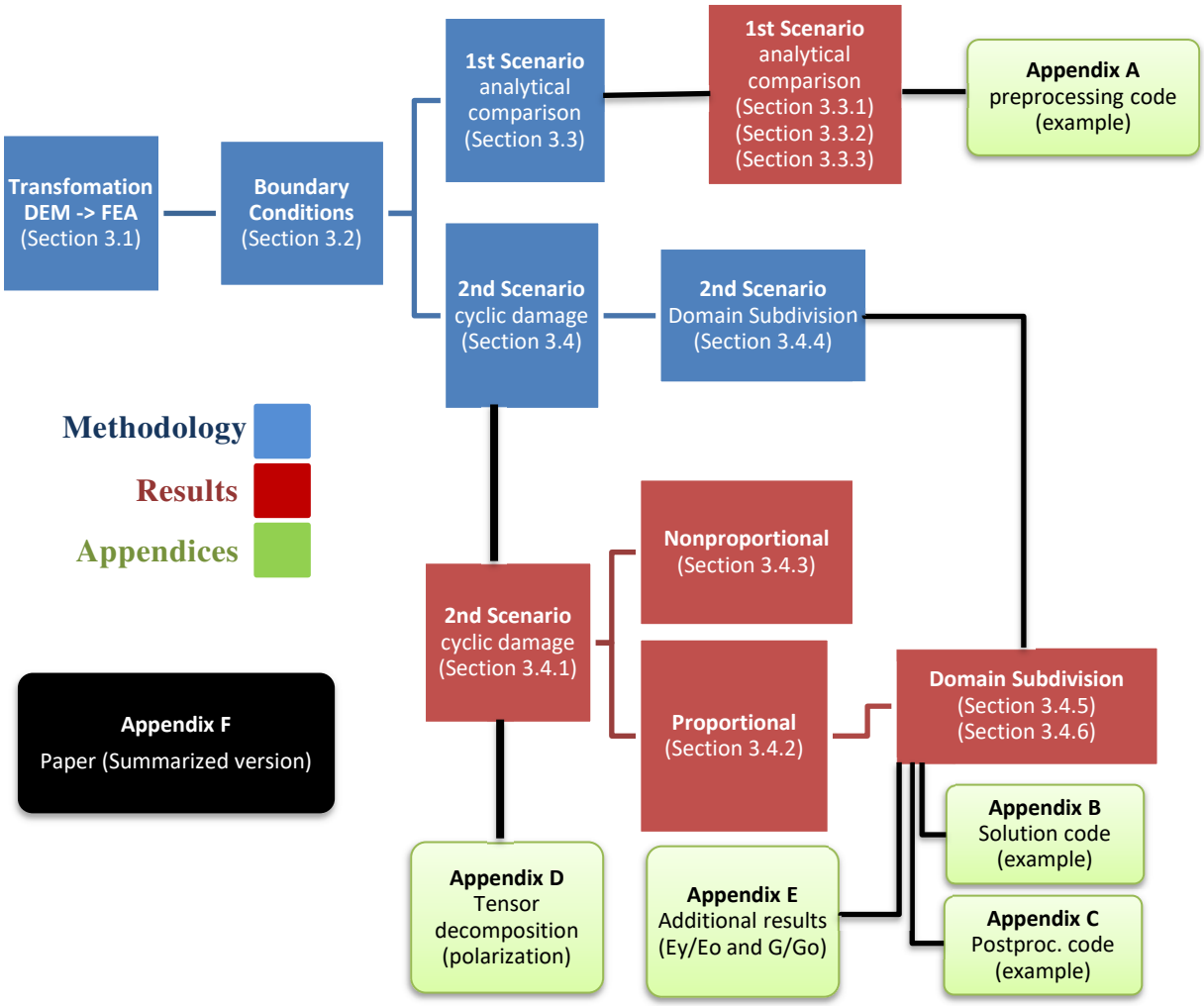

Figure 3.1 – The hierarchy showing the connections between the methodology, results and appendices sections. Appendix F presents the paper summarizing the main information.

The implemented procedure will use as input the extracted data from the damaged LDEM structure to obtain, through a Finite Element Analysis (FEA), the mechanical properties of a particular domain. The study will focus on two main scenarios. At first, the theoretical results are known, and in the second, a more complicated situation is taken, where an initial attempt to analyze the effects of proportional and nonproportional cycling in quasi-brittle material applying the LDEM model is made. Figure 3.2 describes the basic idea of this work, where an LDEM structure already damaged during a Fortran code simulation (input) is transferred into a finite element software for analysis. In this FEA environment, the extraction of material properties using a homogenization procedure is developed. Section 3.1 defines the domain and explains how this transformation is carried out.

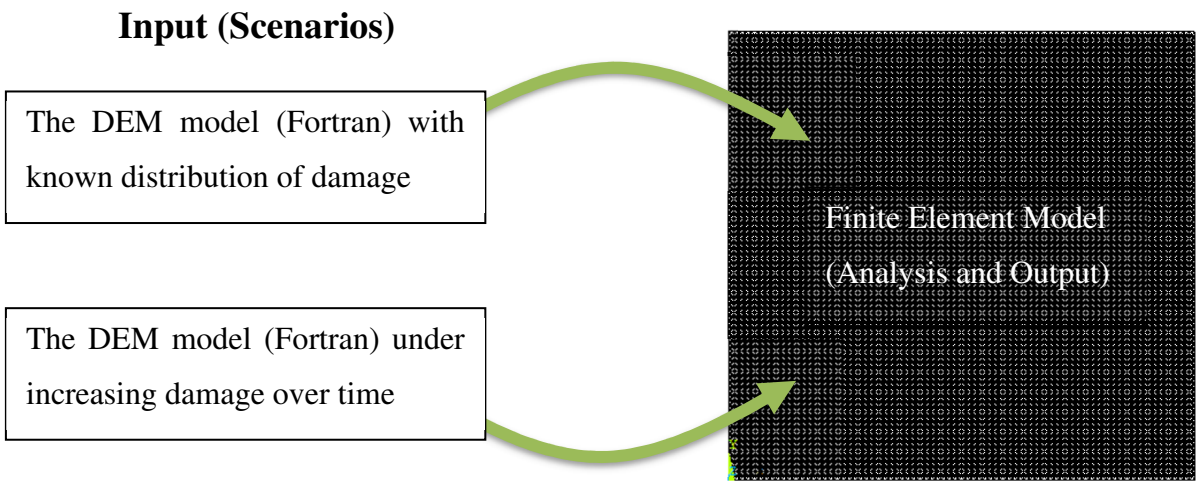

Figure 3.2 - The two scenarios consists on transferring the information of a given moment from the LDEM model (Fortran code) into a Finite Element model (Ansys). This is done to extract the constitutive relationships.

Additionally, it is essential to emphasize that the application of the forthcoming structure of analysis and the designed codes can be expanded with little modifications to any given LDEM problem. The process will consist of recreating a homogeneous continuum using the lattice structure. The damage computed during the LDEM analysis is stored at a given moment. Afterward, the elements' stiffness is imported into the FEA environment where the homogenization procedure can be made. The FEA studies employed the software ANSYS ® V.18.2 and, subsequently, the data treatment was performed using MATLAB ® 2016.

3.1 The Structure/Material Characterization and DEM/FEA Transformation

The overall structure under analysis consists of 79 x 79 x 1 cubic cells. Each cell is defined with the length size L_n equal to $0.0075m$, configuring a plate with $0.351m^2$. Due to the boundary condition, only a plane strain state (PSN) will be considered and the z-axis thickness will not interfere on the analysis despite it be physically modeled with one L_n. The procedure considers no out-of-plane displacement and, therefore, no strain at the Z-axis. A plane stress state (PSS), if required, could be implemented, modifying the boundary conditions. The material properties assume the linear elastic behavior defined by a Young's modulus with 3.5E+10 MPa and a Poisson's ratio of 0.25 as previously explained in section 2.6. Concrete has material properties close to these ones. Figure 3.3a shows the isometric representation where the arrangement of the cubic cells can be seen at the corner of the structure. Figure 3.3b presents the same plate at the x-y plane for a lattice structure with the thickness of one cube. The unitary cell is depicted in Figure 2.23.

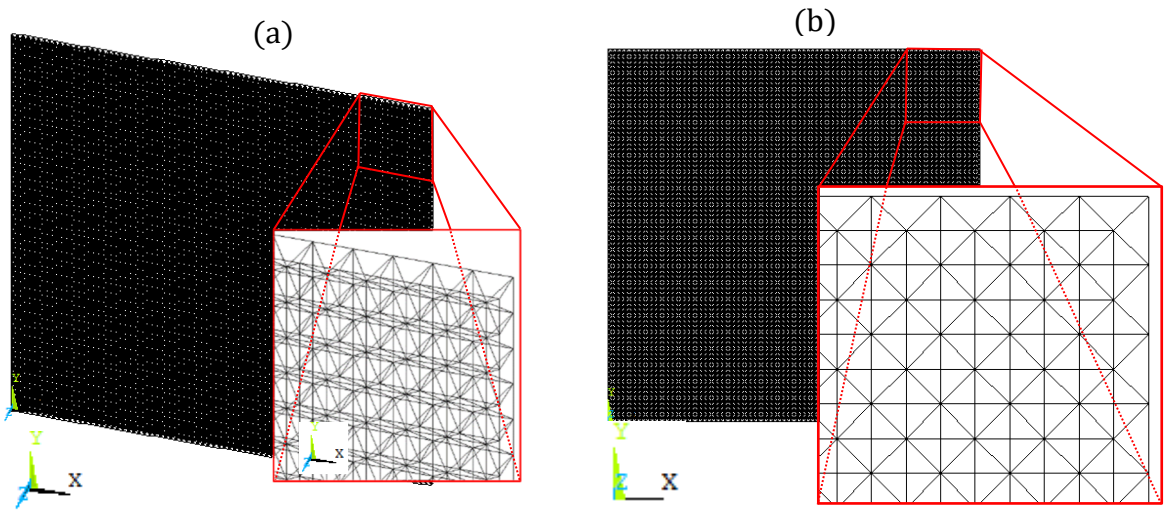

Figure 3.3 - (a) 3D representation of the lattice structure under analysis. (b) 2D representation in the x-y plane for the same body. A closer view is shown at the corner characterizing the periodic cubic elements composed by 79 x L_n by 79 x L_n by 1 x L_n cubic cells.

The structure inside the FEA model is composed of two overlapping pin-joints structures. One is only activated during traction and the other is only activated during compression. The idea behind this concept is to allow different constitutive laws in compression and in traction (Figure 3.4).

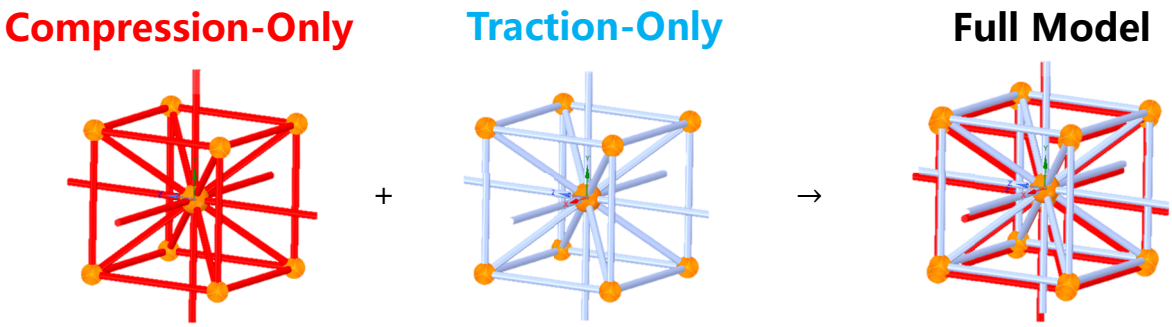

Figure 3.4 – The compression-only and the traction-only structure overlap each other to define a complete truss structure in any condition. The constitutive relations in traction and compression can be different using this technique.

In the context of Ansys 18.2, the element that fulfills these requirements is LINK180, where the links can support tension-only (sectype = 1) or compression-only (sectype = -1). This option turns the numerical solution into a non-linear iterative process. There are two reasons to make this type of structure characterization:

1) *Association with quasi-fragile material's properties:* The material resistance in compression is much higher than in traction. This characteristic does not allow the material to reach its peak resistance in compression and no reduction in stiffness is observed. Therefore, the original material's stiffness is kept as an undamaged structure. On the other hand, when the material is in traction, the bilinear constitutive law is applied and the loss of stiffness must be accounted. This configuration is called a "closed crack" form and it is depicted in Figure 3.5a.

2) *Comparison with the analytical solutions:* The presented outputs of Self-Consistent and Dilute methods consider the same constitutive relations in compression and in traction. Therefore, in order to compare numerical and analytical solutions, the so-called "open crack" form described in Figure 3.5b must be applied when comparing those analytical responses with the extracted numerical ones.

.

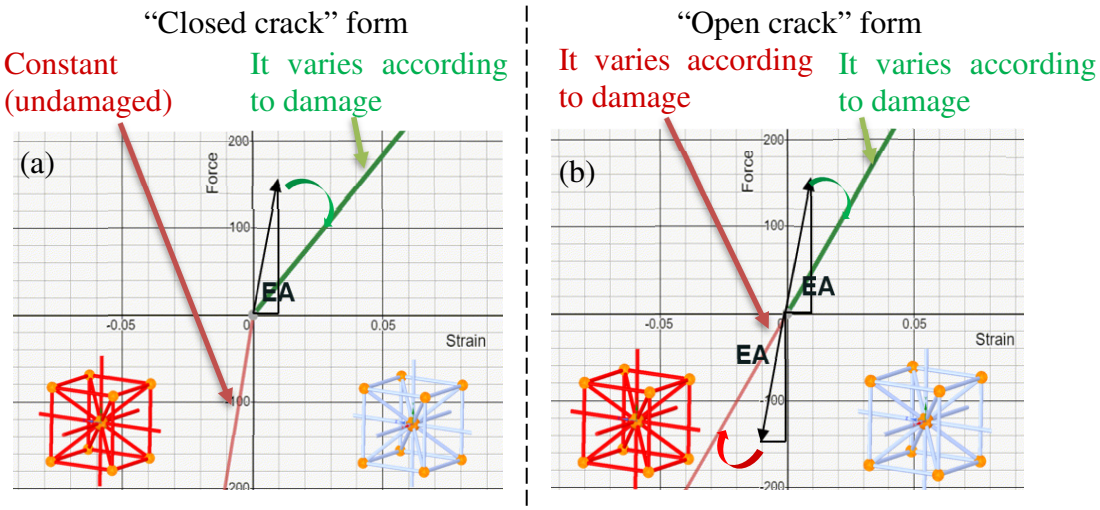

Figure 3.5 – (a) The "closed crack" form considers an undamaged structure under compression. In traction, the stiffness is affected by the damage process. This form mimics the quasi-fragile materials behavior (b) The "open crack" form considers the loss of stiffness in compression and in traction. This form can be compared to analytical solutions.

3.2 Definition of the Boundary Conditions and Properties Extraction

As previously explained in section 2.3.2, the homogenization process must consider three different boundary conditions to define the constitutive tensors when a plane state is established. For convenience, the model presented uses a constant strain condition at the boundaries to perform the analysis. Therefore, the strain tensor is constant ($\varepsilon^0 =< \varepsilon >$) as a displacement profile is defined at the boundaries $\partial\Omega_o$ according to the position x_i. The indices I-III in Equation 3.1 indicates the necessity to apply three boundary conditions in order to define the stiffness or compliance tensor explicitly for a plane state case. The assumptions of micromechanics depicted in Section 2.3 are taken here.

$$u|_{\partial\Omega_o} = {\varepsilon^0}_{ij} \cdot x_j \rightarrow {\varepsilon^{(I-III)}}_{ij} \cdot x_j \tag{3.1}$$

The three load cases are the constant axial deformation in the x-axis, the constant axial deformation in the y-axis and the constant shear deformation considering the xy-plane. The nodes used to define these conditions are the central ones to emulate the same conditions outlined during the DEM model. The load application is quasi-static and under very low strain to produce just small displacement to avoid any second-order regime. Figure 3.6 presents the three conditions imposed on the body. The force reaction at the boundaries is extracted and

averaged in order to obtain the mean stress. The relation between the strain and stress allows us to defined the constitutive tensors according to the damage inside the volume. No individual value inside the volume will be considered, but its implication at the border will promote information about the inner medium. As the structure presents a certain degree of damage, the forces at the boundaries will decrease, meaning that the stiffness will also reduce.

Batista, 2007 presented studies using the forces at each element of the DEM model to define a von mises stress state under constant boundary conditions. He compared it with a FEA model to evaluate mainly the scale effects on the results. It was also demonstrated that there are fluctuations at the border due to the lack of adjacent cells and, as we will see, this will also be an issue in this work.

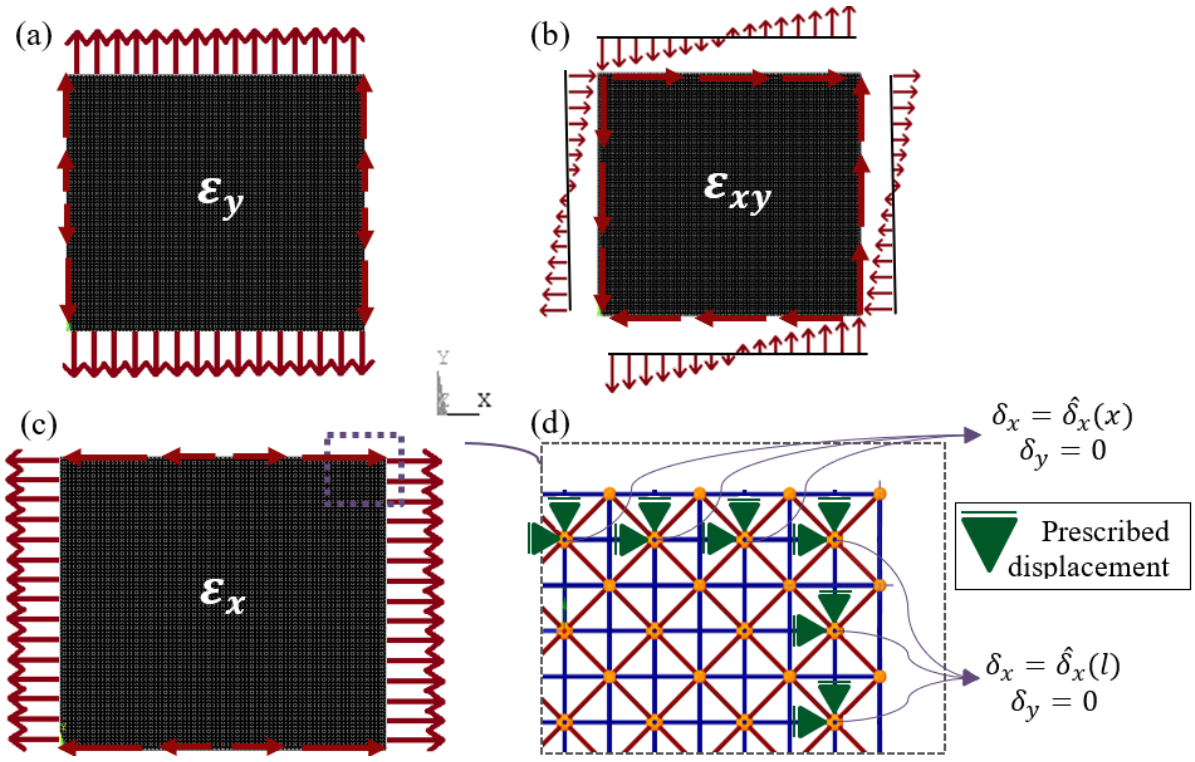

Figure 3.6 - (a) Axial displacement at the border in u_y to generate a constant strain field ε_y. (b) shear displacement in x and y direction to establish a constant strain field ε_{xy}. (c) Axial displacement at the border in u_x to generate a constant strain field ε_x.

The analytical solution will define the reference value and used as a comparison for the loss of stiffness of the structure as the damage grows. The stiffness and compliance tensors in a matrix form are presented in Equation 3.2 and 3.3.

$$\sigma_i = C_{ij}\varepsilon_j \therefore \begin{pmatrix}\sigma_{xx}\\ \sigma_{yy}\\ \sigma_{xy}\end{pmatrix} = \frac{E}{(1+\vartheta)\cdot(1-2\vartheta)}\begin{pmatrix}1-\vartheta & \vartheta & 0\\ \vartheta & 1-\vartheta & 0\\ 0 & 0 & \frac{1-2\vartheta}{2}\end{pmatrix}\cdot\begin{pmatrix}\varepsilon_{xx}\\ \varepsilon_{yy}\\ 2\varepsilon_{xy}\end{pmatrix} \tag{3.2}$$

$$\varepsilon_i = S_{ij}\sigma_j \therefore \begin{pmatrix}\varepsilon_{xx}\\ \varepsilon_{yy}\\ 2\varepsilon_{xy}\end{pmatrix} = \frac{1+\vartheta}{E}\begin{pmatrix}1-\vartheta & -\vartheta & 0\\ -\vartheta & 1-\vartheta & 0\\ 0 & 0 & 2\end{pmatrix}.\begin{pmatrix}\sigma_{xx}\\ \sigma_{yy}\\ \sigma_{xy}\end{pmatrix} \tag{3.3}$$

Applying the materials' properties described in Section 3.1, we will obtain the undamaged properties of the medium as presented in Expressions 3.4 and 3.5. Also, two terms are defined as the directional elastic and shear moduli at the plane strain state in Equation 3.6. The inverse of the diagonal elements of the compliance matrix clarifies what will be called as in-plane Elastic Modulus for a plane strain state at both x and y-axis (E_o) and the in-plane shear modulus G_o. All the results will consider as reference these analytical values to describe how the properties will evolve according to damage. This approach is more attractive when compared to a pure tensorial form, allowing the visualization of familiar entities to the reader.

$$S_{ab} = \begin{pmatrix}S_{11} & S_{12} & 0\\ S_{21} & S_{22} & 0\\ 0 & 0 & S_{33}\end{pmatrix} = \begin{pmatrix}2.6785 & -0.893 & 0\\ -0.893 & 2.6785 & 0\\ 0 & 0 & 7.143\end{pmatrix}10^{-11} \tag{3.4}$$

$$C_{ab} = \begin{pmatrix}C_{11} & C_{12} & 0\\ C_{21} & C_{22} & 0\\ 0 & 0 & C_{33}\end{pmatrix} = \begin{pmatrix}42 & 14 & 0\\ 14 & 42 & 0\\ 0 & 0 & 14\end{pmatrix}10^{+9} \tag{3.5}$$

$$\begin{pmatrix}1/S_{11} & - & -\\ - & 1/S_{22} & -\\ - & - & 1/S_{33}\end{pmatrix} = \begin{pmatrix}E_o & - & -\\ - & E_o & -\\ - & - & G_o\end{pmatrix} = \begin{pmatrix}37.333 & - & -\\ - & 37.333 & -\\ - & - & 14\end{pmatrix}10^{9} \tag{3.6}$$

Based on these analytical values, the DEM structure imported inside the finite element software can be used to analyze the evolution of such properties as the damage increases.

3.3 1st Scenario: Methodology for the Analytical Comparison

One form of confirming the validity of the described discrete model is to compare it to a known analytical and well-established solution. This study will be called as the 1st Scenario

hereon. At the LDEM model previously described, a set of randomly oriented cracks with different sizes, orientation and quantity are used to compute progressive degenerating macro properties. Faults with 4 x L_n, 7 x L_n and 11 x L_n, are spread randomly over the control volume (C.Vol) defined by the plate domain of 79 x L_n of side. A Fortran code is applied to generate voids, similar to cracks, where the stiffness at defined regions are reduced to near zero. Five random distributions, maintaining the number of faults, are created to evaluate the statistical properties.

Additionally, the total number of faults is also increased to verify the effect of the crack density parameter f over the material properties allowing a comparison with the Self-Consistent analytical solution (see Section 2.3.7). Figure 3.7 shows examples for each crack size type with a detailed view around the faults. This scenario does not restrict overlapping among the defects.

The following discrete structures are created and the number underlined are the ones presented in Figure 3.7:

- 4 x L_n case with 0, 10, 20, 30, 40, 50, 60, 70, 80, 100, *120*, 140, 180, 220 cracks (up to $f \approx 0.15$)

- 7 x L_n case with 0, 5, 15, 25, *35*, 45, 55, 65, 75, 85 cracks (up to $f \approx 0.17$)

- 11 x L_n case with 0, 5, 8, 10, *13*, 15, 18, 20, 23 cracks (up to $f \approx 0.12$)

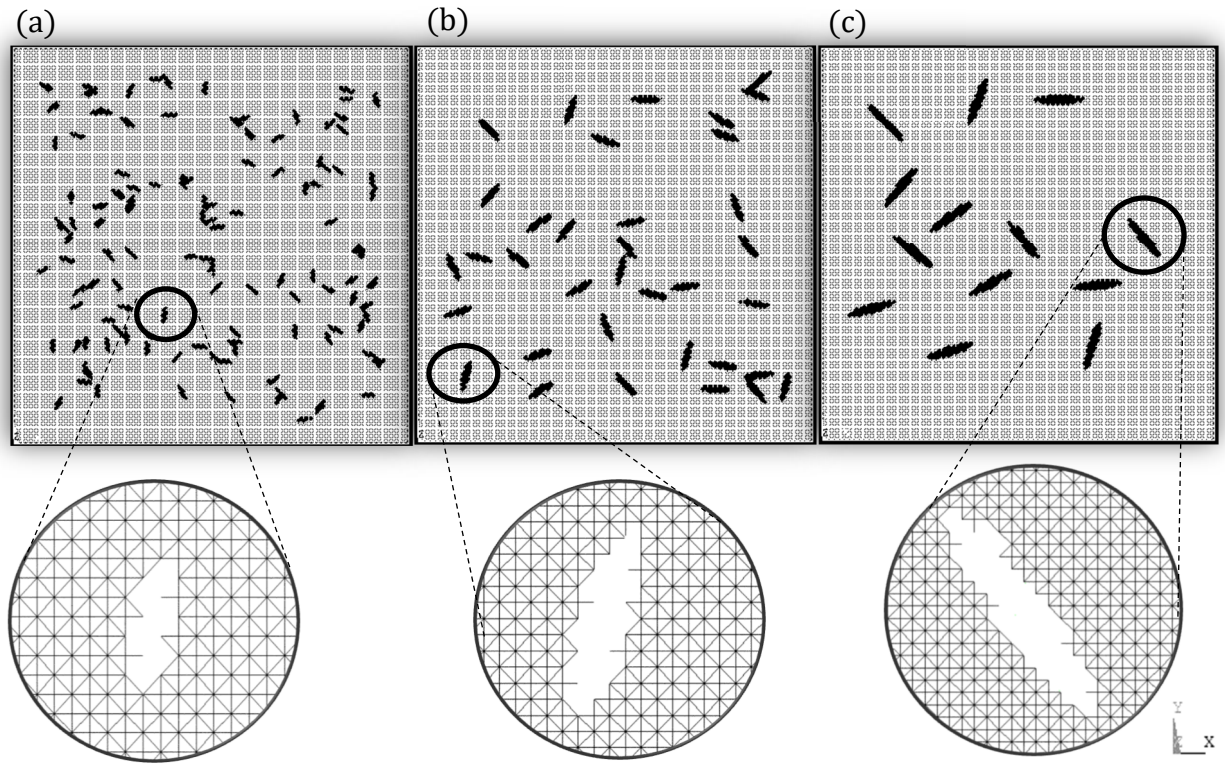

Figure 3.7 - (a) Examples with a random distribution of cracks with 4 x L_n (example with 120 faults) (b) with 7 x L_n (example with 35 faults) and (c) 11 x L_n (example with 13 faults) over a control volume (C.Vol.) with 79 x L_n of side.

3.3.1 Results of the Analytical Comparison

Among the analytical solution presented in Section 2.3.6 and Section 2.3.7 for embedded faults in a medium, the best approximation for interacting cracks is the Self-Consistent model. The theory does not define the terms of "proximity," but it is the best form to account for some analytical approach for the ongoing study. It also simplifies the comparison because the model does not distinguish macrostress from macrostrain. Only the condition of plane strain (PSN) or plane stress (PSS) shown in Table 2.1 must be accounted for. The solutions are only valid for the "open" cracks scheme as the "closed" form is a non-linear solution due to the different behavior in compression and in traction (see Figure 3.5). Nemat-Nasser and Hori, 1999 demonstrate clearly that for the "closed" form, the stress state and the angular position at each individual fault will define a condition of compression or traction on the crack. Therefore, depending on how the load is applied, the void will be "open" or "closed," and this will lead to a different relation between strain and stress. This fact means that different constitutive relationships will be defined depending on the load configuration. Due to these conditions, the study of an "open" crack configuration is more accessible and it is described firstly and compared directly with the theoretical prediction.

As previously mentioned, the in-plane Young's (E_o) and shear (G_o) moduli of an undamaged continuum medium at plane strain state are computed as the reference value for the ongoing study. The LDEM structures with known crack density parameter f are incorporated in the FEA model with domain containing 79 x L_n by 79 x L_n cells.

The three cases, with the sizes of the cracks equal to 4 x L_n, 7 x L_n and 11 x L_n, are investigated individually. It is essential to observe that the implementation of large cracks means that, for the same parameter value f, fewer faults are embedded in the medium. This means that for the same control volume (C.Vol.), the 11 x L_n case will have a higher sensibility to additional faults. On the other hand, an additional defect with 4 x L_n will have little impact on the overall behavior of a structure as the number of cracks is more abundant for the same f.

Figure 3.8a describes the E_x/E_o (○) and E_y/E_o (□) variation for five different damaged structures according to increasing values of the crack density parameter f. In this case, the faults are all equal to 4 x L_n presenting an increasing coefficient of variation as the f grows. The CV_{Ex} reaches almost 4% when $f = 0.14$. It is clear to see that the Self-Consistent (blue line) agrees very closely with the extracted data at small values of f. As the crack density increases, the two approaches start to diverge as the variation also increases.

Additionally, E_x/E_o (○) and E_y/E_o (□) data clearly shows a symmetric relation over a mean value, i.e., when, for example, the value of E_y/E_o changes more significantly, the perpendicular term (E_x/E_o) will always face minor decrements. This was also observed valid when E_x/E_o varies more, establishing a low variance in E_y/E_o. This effect is caused by the random distribution of cracks imposed on the structure, which will have a preferential alignment in a particular direction. A simple example can be given when a few cracks are embedded randomly in the medium. For example, if three cracks are incorporated at the domain, they will align in a preferential direction. This alignment will affect the properties in one axis more than the other. Therefore, the random distribution of faults does not mean isotropic damage and the direct comparison with the Self-consistent method cannot be done appropriately. By increasing the number of random defects, there is a tendency to isotropic behavior naturally. In order to compare the numerical solutions with the analytical ones, an isotropic crack distribution must be provided. This is done averaging E_y/E_o and E_x/E_o as presented in Figure 3.8b. The coefficient of variance becomes lower (<2.5%) compared to individual X-axis and Y-axis values. This effect will be much more evident for 7 x L_n and 11 x L_n cases.

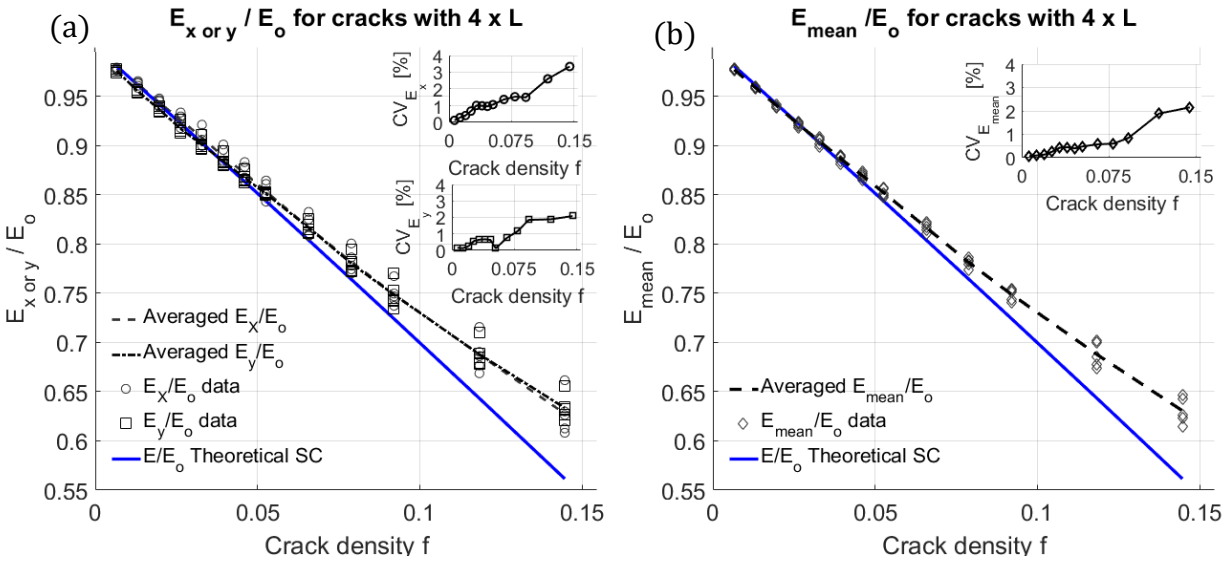

Figure 3.8 - (a) Extracted data from DEM/FEA model compared to analytical solution for the y-axis ($E_y - \square$) and x-axis ($E_x - \circ$). Each one is composed of 5 different simulations. (b) The mean value of E_y and E_x are computed as E_{mean}. Both plots show the coefficient of variation according to the crack density parameter f. Open cracks with 4 x L_n (overlapping allowed).

Figure 3.9a describes the evolution of the same parameters for the 7 x L_n case for five different damaged structures. The dispersion augments with f, reaching CV_{Ex} values of almost 8% when $f = 0.17$. The effect of averaging presented in Figure 3.9b stands out compared to 4 x L_n case. The CV does not surpass 2% at any circumstances, which gives a sense of improvement in the data dispersion.

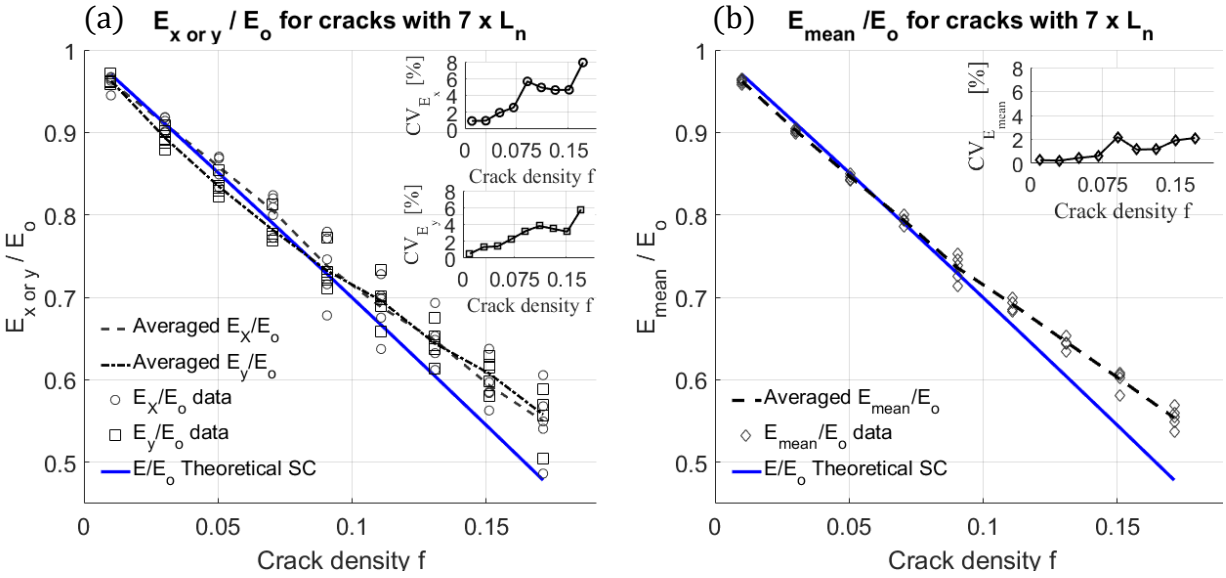

Figure 3.9 - (a) Extracted data from DEM/FEA model compared to analytical solution for the y-axis ($E_y - \square$) and x-axis ($E_x - \circ$). Each one is composed of 5 different simulations. (b) The mean value of E_y and E_x are computed as E_{mean}. Both plots show the coefficient of variation according to the crack density parameter f. Open cracks with 7 x L_n. (overlapping allowed).

Lastly, the 11 x L_n case is presented in Figure 3.10a, b. In general, the fluctuation and dispersion are distinctly greater even for small parameters f. As the size of the faults approaches the C.Vol. size, more significant variation at the border is notable. Cracks with 11 unities certainly do not agree with the RVE assumption of d (dimension of the fault) << D (dimension of the body). Additionally, changes in individual faults' orientation will produce extensive modifications at E_x and E_y due to the necessary to add fewer cracks for the same parameter f. These two distinct factors are responsible for more significant fluctuation in the results. However, the averaging process showed in Figure 3.10b clearly enforces Young's modulus to a well-behaved curve with a coefficient of variance lower than 3.5%.

The Self-Consistent results (blue line) do not take into account the crack size explicitly; therefore, the three cases show the same curve, which decreases at a higher rate compared to the extracted results from the DEM/FEA model (black lines).

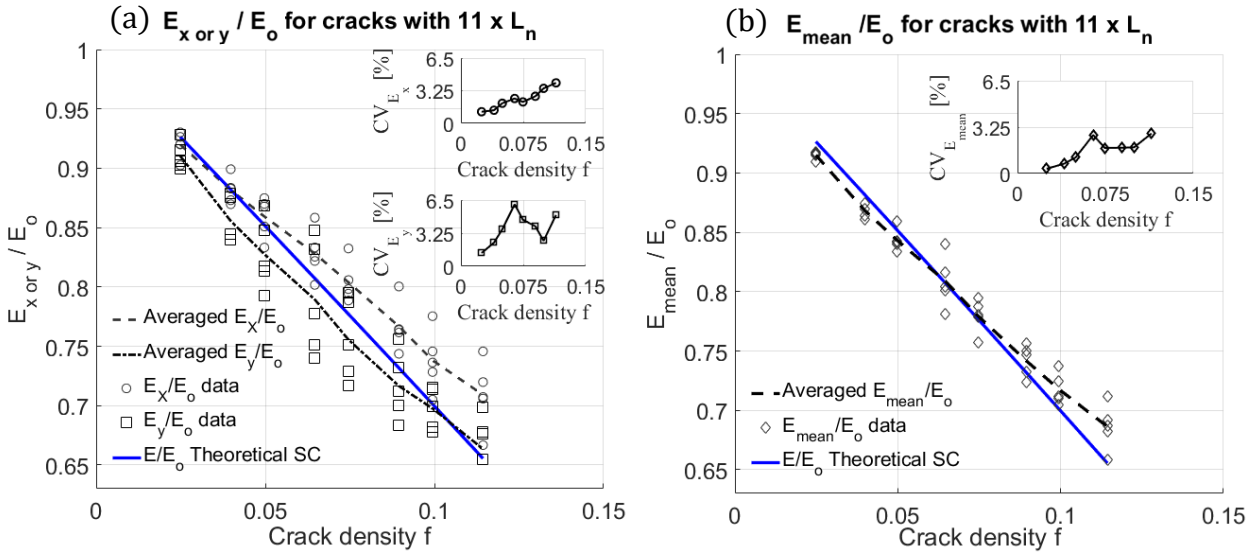

Figure 3.10 - (a) Extracted data from DEM/FEA model compared to analytical solution for the y-axis ($E_y - \square$) and x-axis ($E_x - \circ$). Each one is composed of 5 different simulations. (b) The mean value of E_y and E_x are computed as E_{mean}. Both plots show the coefficient of variation according to the crack density parameter f. Open cracks with 11 x L_n (overlapping allowed).

The same study was mode considering the "closed" cracks scheme to evaluate the differences related to the "open" crack configuration. However, a positive strain-controlled system will always open the faults. Thus, E_y and E_x must be the same as presented in Figure 3.10, Figure 3.9 and Figure 3.8. Adjusting the properties of each link in compression to behave as an undamaged connection and following the same numerical simulation procedure has generated the same output as expected. It is important to emphasize that the similarity just occurred due to the outward strain. If a constant, but negative strain, were imposed on the domain, the extracted values would be equal to an undamaged body. The constitutive/compliance tensor in a "closed" crack form is indeed a load-dependent entity.

On the other hand, the results for shear strain will not be the same for the "open" and "closed" crack scenarios. Figure 3.11a, b and c present the shear modulus G variation according to the crack density for an "open," "closed" and Self-Consistent models. The "open" and SC data are similar and particularly suitable for small crack size (4 x L_n). The coefficient of variation increases as the crack size grows as it has happened for the Young's modulus study.

But, the "closed" crack simulations presented a different and interesting output. The reduction of the shear modulus G, in this case, is about half of the theoretical value of the "open" crack scheme. Apparently, this observation is easy to comprehend if one considers a random distribution of defects. Statistically, for an isotropic distribution, half of the overall voids will be aligned at an angle that will induce a compression state on the bars, closing the defect and activating a non-damaged constitutive law. The other half will be in traction mode, which enables a negligible stiffness state at the bars allowing them to open. It is quite interesting to note that this phenomenon was capture naturally without imposing any condition to the structure or to the LDEM model. Observing the coefficient of variance of each case, it is also remarkable that the lower fluctuation in the closed form. A factor that possibly helps to minimize the variation is related to lower distortion imposed by a smaller quantity of active cracks and their interacting fields, which will also decrease the perturbation on the boundary surfaces.

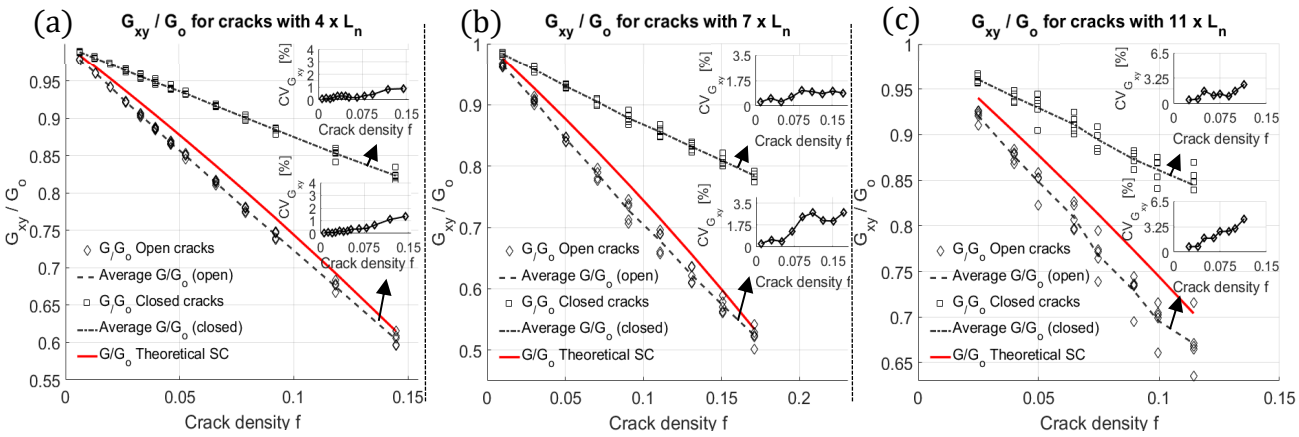

Figure 3.11 – (a) Shear modulus G/G_o variation for 4 x L_n, (b) 7 x L_n and (c) 11 x L_n cases. The dispersion also increases with crack size. The reduction in the values for "closed" scheme are about half of the values for an "open" scenario.

3.3.2 A Brief Study for Nonoverlapping Faults

All the described results have in common a random distribution of cracks generated by a code, where the faults are allowed to overlap each other. The Fortran code permits, to a small extent, to establish voids without superposition up to a crack density of 0.04. The 11 x L_n case is studied at three crack density values to evaluate whether the solutions show any difference from the overlapping one. Figure 3.12a introduces all the data and Figure 3.12b presents the same averaging process previously described for "overlapping" and "no overlapping"

circumstances. The averaging process narrows the dispersions and the standard deviation is not larger than 0.01 for both cases. Their averaged curves are consistently close up until the limitation of $f = 0.04$. Unfortunately, it is not possible to establish the behavior for larger values with the applied crack generator code, but one can observe that the overlapping does not induce the dispersion of the results significantly. The other issues previously commented as the strain/stress field interaction and the perturbations on the boundaries are probably the primary sources of variance.

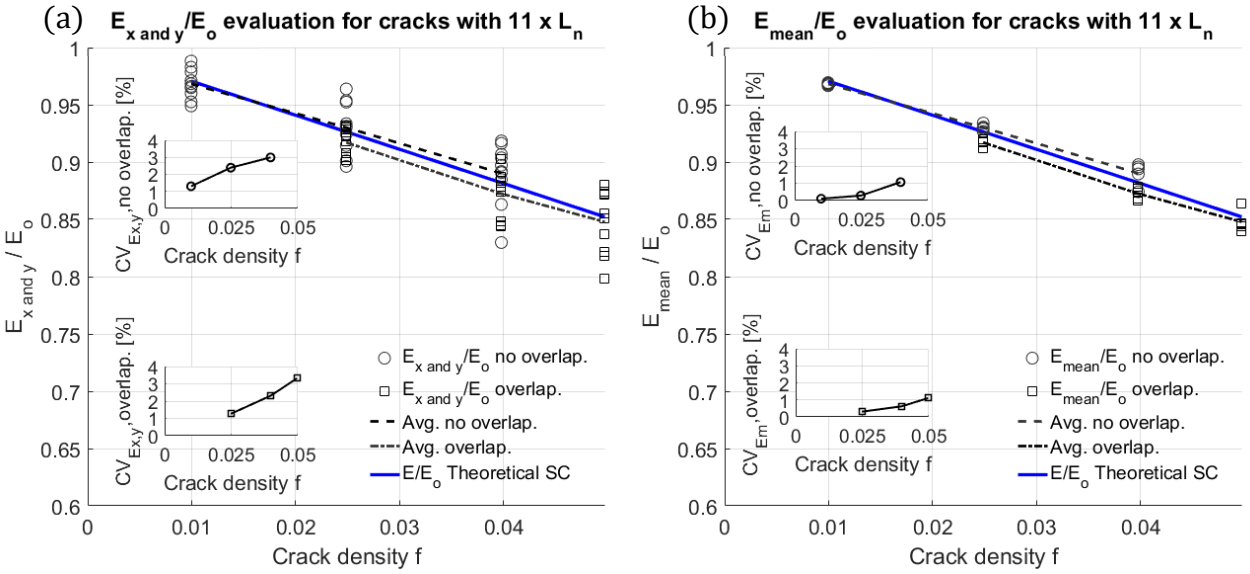

Figure 3.12 - (a) Original data for cracks with 11 x L_n with overlapping allowed and no overlapping allowed. (b) The same study, but with the mean value E_{mean}. The maximum density parameter f permitted by the crack generator code is 0.04.

3.3.3 Self-Consistent x Averaged Data

An additional plot summarizing the deviation from the analytical Self-consistent model for "open" cracks is presented in Figure 3.13. The dispersion and the diverging process of the three scenarios are shown for the scale $0 < f < 0.2$. In these plots, it is clear to observe that the averaged E_{SC}/E_{mean} has a difference below 4% for $f < 0.1$, diverging progressively as the crack density increases.

The self-consistent results start to reduce at a higher rate, while the extracted data reduces at a slower rate leading to divergence at the plots. However, it is a considerably good agreement taking into consideration the completely different approaches that both procedures are based on. On the other hand, the G_{SC}/G relation presented in Figure 3.13b has an "arc" form due to an explicit linear behavior of the extracted data (see Figure 3.11), while the Self-Consistent

model decreases exponentially. However, considering an averaged value, the differences do not surpass 5% at $f = 0.1$, which is also an interesting result considering all the possible sources of error.

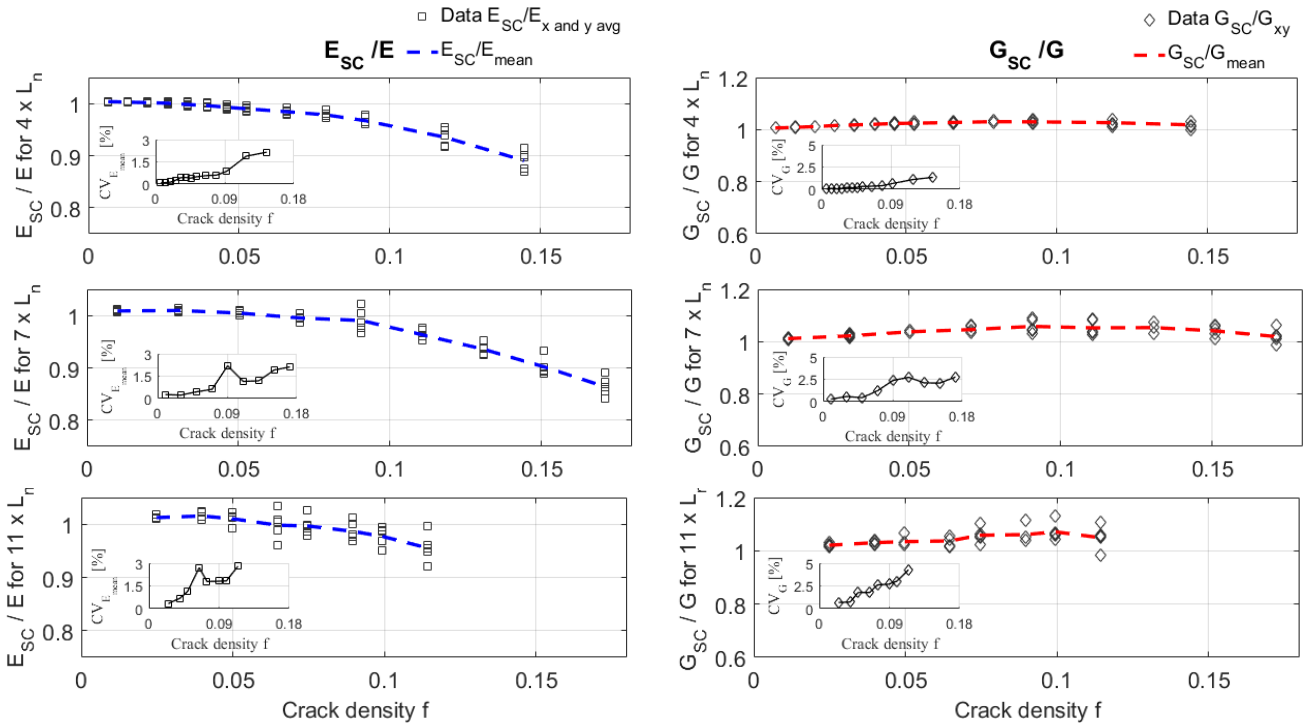

Figure 3.13 - Relation E_{SC}/E_{mean} and G_{SC}/G for "open" crack scheme at the three scenarios under analysis (4 x L_n, 7 x L_n, 11 x L_n). As the crack density parameter increases the dispersion of the results augments.

The displayed results confirm that the application of the LDEM/FEA methodology agrees closely with theoretical predictions. A step forward is to apply the method to any other LDEM study to observe if the application of such procedure provides additional insights about the structure under analysis. The chosen one is related to a cyclic loading model covered as the 2nd Scenario.

3.4 2nd Scenario: Cyclic Loading Case

This Chapter holds the description of Section 3.1 and 3.2. The specific methodology (Section 3.4.1) and the results (Section 3.4.2 and 3.4.3) for a case where the response is not known are discussed. Section 3.4.4 presents a method that considers the subdivision of the structure into smaller parts for an undamaged domain. The results are treated in Section 3.4.5. The specific case where the cyclic loading is applied is described in Section 3.4.6.

3.4.1 Methodology for the Complete Domain with Cyclic Loading

After the application of the homogenization process in a known domain, a case where the process causes damage and the output is not controlled is studied. The chosen case is characterized by oscillating loads applied in an LDEM model due to sinusoidal force variation [Soares, 2019]. This process is time-dependent, which means that the FEA analysis needs to be placed at specific time-steps of the total lifespan of the structure (Figure 3.14). The LDEM structure suffers the loss of stiffness in the time domain. At specific frames of the simulations, the data of the structure is stored with the stiffness of each bar after some cycles. This is done inside the Fortran environment from an initial undamaged condition up until moments before percolation.

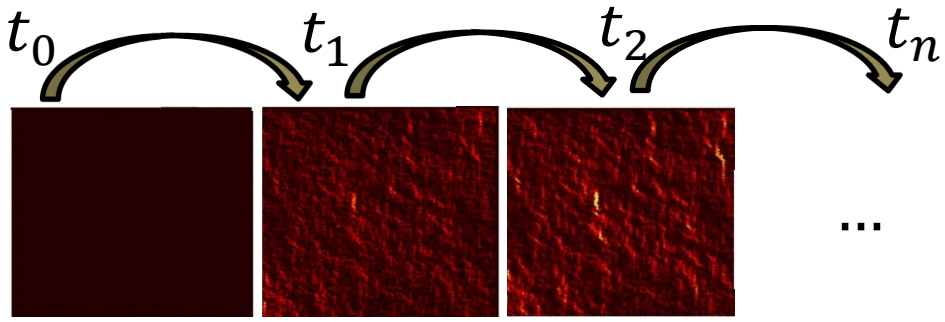

Figure 3.14 – Concept of analysis in the time domain. The damage/stiffness of individual links are stored in defined moment of an LDEM analysis (Fortran). Then, the FEA model (Ansys) studies the loss of stiffness at these given moments.

Soares, 2019 developed two primary schemes for the analysis of multiaxial cycling using DEM models. The first is a proportional loading process where shear stresses τ_{xy} and normal stresses σ_x are applied in-phase. The second one is a 90º out-of-phase nonproportional loading.

In both cases studied, the amplitude of the normal and shear stresses is the same differing only by the out-of-phase scheme used at the nonproportional loading. Figure 3.15 presents an example of how the shear and normal stresses behave in these conditions. The stress amplitudes of the proportional case are described by a magnitude of 206 MPa and set with a stress ratio of zero ($R = 0$). Soares, 2019 developed the two scenarios for the analysis of multiaxial cyclic loadings using DEM models with the constant lifespan defined at 100 cycles, which lead to amplitudes and mean values 13% larger for the nonproportional simulation. The coefficient of variation $CV(G_c)$ was defined with 70% at which the energy release rate $\overline{G_c}$ was established at

16000 N/m in Soares' work (see Figure 2.29). The concepts of these entities were discussed in Section 2.6.

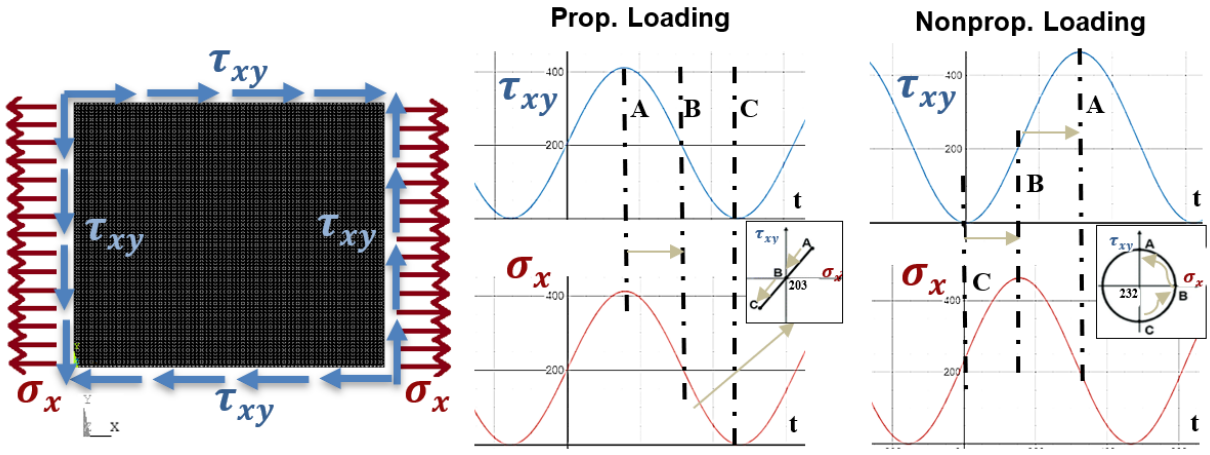

Figure 3.15 -The proportional and nonproportional σ_x and τ_{xy} sinusoidal stress application at the domain's borders applied for the cyclic cases using DEM. Stress ratio R = 0.

The load will affect the elements initially with lower maximum resistance, reducing the stiffness and inducing a damage energy release that can be traced back to specific locations. Therefore, the damaged links will not sustain a significant part of the load anymore that will increase the stresses at surrounding components, leading them to mechanical properties reduction as well. The periodic forces will naturally cause a chain reaction that eventually will cause the percolation. Figure 3.16 presents the results from Soares, 2019, where a scale of energy released during the process of damaging is shown at specific time-steps. In this case, the domain is defined by only 70 x L_n by 70 x L_n, i.e., the Control Volume (C.Vol.) disregards some external elements due to conditions imposed at the borders. Some moments during the entire life of the structure were stored in order to evaluate the modification at the material properties. Instead of using the number of cycles, a relative parameter considering the total number of numerical iterations up until percolation is defined as a percentage of the lifespan of the structure. The total number of numerical iterations reached 490000 (100% lifespan):

-0% lifespan (number of numerical iterations 100 – no damage)
-3.5% lifespan (number of numerical iterations 17000)
-5.2% lifespan (number of numerical iterations 25340)
-7% lifespan (number of numerical iterations 34000)
-8.5% lifespan (number of numerical iterations 41500)
-10.5% lifespan (number of numerical iterations 51000)
-40% lifespan (number of numerical iterations 200000) …

Figure 3.16 shows three moments as the cycling process occurs. The proportional case is characterized by a quicker process where most of the damage happens before the 3.5% lifespan. As can be seen at a 40% lifespan, the characterization does not change a lot. It was noted that at just 99% of the cycling, a percolation process occurs at the top left side of the structure.

On the other hand, the nonproportional case has a slower energy release process, as observed in Figure 3.16b. Additionally, the formation of clusters is more severe and spread over the body. An interesting aspect of this type of material representation is the way that the damage is evenly distributed throughout the body, similarly to the studies presented in Section 2.4.

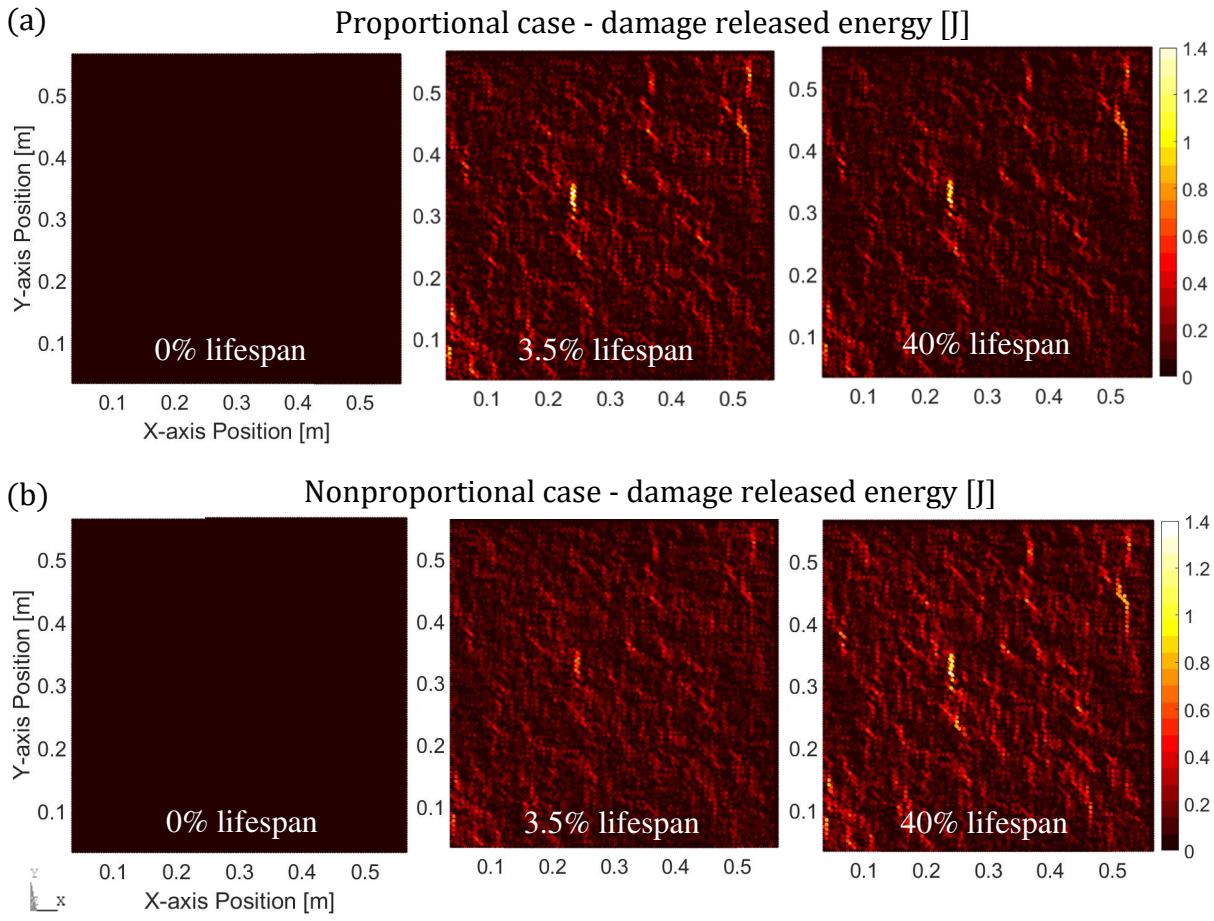

Figure 3.16 - (a) Proportional load case where the damage released energy is presented at 0%, 3.5% and 40% of the lifespan. (b) The same for the nonproportional load. 100% lifespan means percolation. [Soares, 2019]

The energetic consideration are not discussed here, but the properties' modifications caused by a combination of axial σ_x and shear τ_{xy} stresses applied at the boundaries of the 70 x L_n by 70 x L_n plate, causing increasing damage over time. The decrement in stiffness will produce more significant strain on the bars if a constant strain is applied at the boundaries.

Figure 3.17 is an example of individual links' deformation at the 3.5% of their lifespan under proportional loading. The representation indicates just three strain scales (white, black and grey colors) to be able to distinguish damaged and undamaged links for an induced macrostrain ε_{xx} (a), ε_{yy} (b) and ε_{xy} (c). It is possible to visualize at Figure 3.17a, b and c the maximum strain indicated by (MX), which represents the same position as the maximum damage released energy (see Figure 3.16a).

Figure 3.17a shows an example in a given time during the cyclic loading. The elements aligned with the X-axis are the ones in which the stiffness is more degenerated. While the diagonal elements (L_d), which are represented in Figure 3.17c, are activated by the shear process and less damaged compared to the X-axis element L_n. On the other side, the Y-axis links do not weaken by a significant amount (Figure 3.17b).

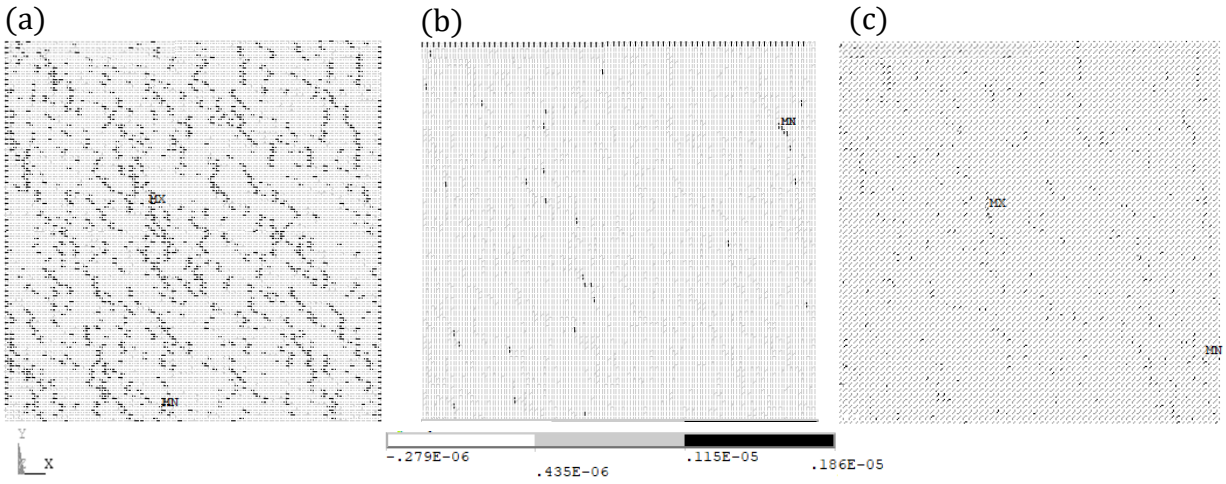

Figure 3.17 – The three plots show a scale of deformation for a damaged domain when applying constant (a) ε_{xx} (b) ε_{yy} and (c) ε_{xy}. The black lines represent the increased strains at damaged elements at each direction. It is clearly the preferential disturbance in X-axis. The case is for a 3.5% lifespan under proportional loading.

It is possible, as a first approach, to evaluate the stiffness tensor's components according to cumulative effects. As expected, the results displayed the loss of stiffness due to the increasing damage. At an initial state, the components C_{11} and C_{22}, related to the in-plane E_x and E_y, respectively, presented an error compared to the analytical solution lower than 0.4%. Some fluctuation can happen here, possibly due to the combination of the nonlinear solution and corner fluctuations already mentioned previously. The C_{33} term, also known as the shear modulus G, returned the same value as predicted by the continuum mechanics formulation (0% error). However, as the links lose rigidity, their properties decrease very fast for the cyclic case

studied. Figure 3.18 shows that the body is primarily under the damaging process between time-steps 0 (undamaged) until time-step 0.035 (3,5% of the total lifespan) changing slightly after this point. The simulations run just until time-step 0.105 due to the small variation of the overall properties after that point. Soares, 2019 also concluded that the released energy follows a similar path showing that the formation of new clusters does not occur after the initial cycles. The local damage progresses only at the finals interactions, where a percolation process occurs abruptly. The smaller variation due to damage happens to C_{22} term, while the largest changes are due to the x-axis loading as can be seen in C_{11}curve, dropping up to 88% of its original value for the plane strain state condition. The shear modulus G also presents significant reduction owing to the damage at the diagonal elements caused by the shear stresses τ_{xy}. Nevertheless, it must be observed that these results consider the same approach as a "closed" crack system, i.e., the links keep their undamaged properties in compression.

Another interesting aspect shown in Figure 3.18 are the terms C_{12} and C_{21}. Due to the symmetric condition of the tensor, they should be equal, but as the damage grows, their values diverge by a small difference of 1% when using the homogenization procedure for the lattice structure. Table 5.1 presents the stiffness matrices, where it can be seen that the difference between the symmetrical terms is minimal.

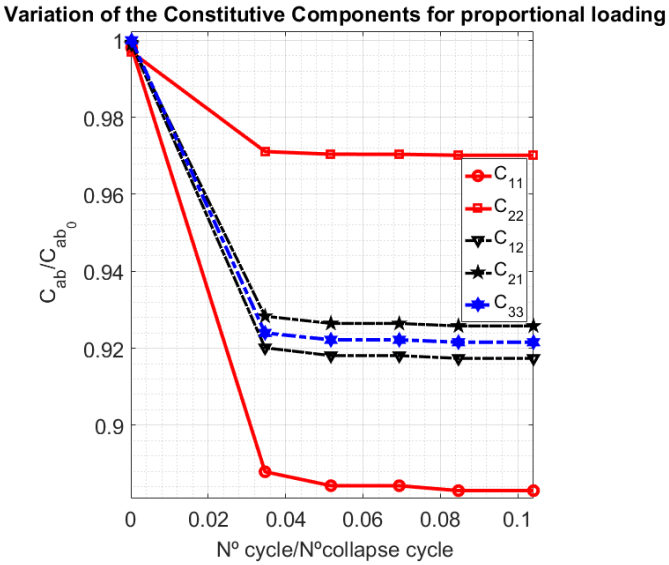

Figure 3.18 - The changes in constitutive terms due to increasing damage up until 10% of the lifespan. The values are compared with the analytical solution of an undamaged isotropic structure. Proportional loading in plane strain state (PSN). "Closed" crack approach.

All the results consider a structure with the "closed" crack approach. Therefore, the tensor in load-dependent, as discussed previously. If the loads were applied in compression per

example, the values would differ from the one presented here. In these circumstances, the positive (outward) strain enforces the fractures to open, which defines the worst condition for the media to withstand.

Table 3.1 – Plane strain stiffness tensor for each time-step under analysis. Proportional loading.

Second-order Stiffness Tensor during the damaging process (Pa)	Lifespan
$\begin{pmatrix} 41.920 & 13.986 & 0 \\ 13.986 & 41.871 & 0 \\ 0 & 0 & 14.000 \end{pmatrix} 10^9$	0%
$\begin{pmatrix} 37.292 & 12.882 & 0 \\ 12.997 & 40.786 & 0 \\ 0 & 0 & 12.936 \end{pmatrix} 10^9$	3.5%
$\begin{pmatrix} 37.140 & 12.853 & 0 \\ 12.970 & 40.757 & 0 \\ 0 & 0 & 12.911 \end{pmatrix} 10^9$	5.2%
$\begin{pmatrix} 37.140 & 12.853 & 0 \\ 12.970 & 40.756 & 0 \\ 0 & 0 & 12.911 \end{pmatrix} 10^9$	7%
$\begin{pmatrix} 37.086 & 12.843 & 0 \\ 12.961 & 40.746 & 0 \\ 0 & 0 & 12.902 \end{pmatrix} 10^9$	8.5%
$\begin{pmatrix} 36.269 & 12.370 & 0 \\ 12.402 & 40.430 & 0 \\ 0 & 0 & 12.654 \end{pmatrix} 10^9$	10%

As can be seen, the damaged evolution changes the isotropic behavior of the structure into an orthotropic-like material.

3.4.3 Results with Nonproportional Loading Case

The same procedure was applied for the nonproportional loading conducted by Soares, 2019, in his studies using DEM. In Figure 3.16b, the damage released energy follows a slower increment as the cyclic process occurs compared to the proportional case. To observe how the two schemes differ from each other, the plot in Figure 3.19 describes the evolution of the Young's moduli and shear moduli. The time range was expanded up until 40.8% due to the increasing changes in the properties for the nonproportional case. After this point, the modification is not relevant. As observed in Figure 3.16, the nonproportional loading has a

more substantial impact on damaging the elements than the proportional one. This fact will lead to higher modifications to the properties, as presented below.

At the mark of 0.4, the difference is around 4.5% between the E_x cases. E_y and G are also more influenced by the nonproportional scenario, but by a small amount. It is important to emphasize that this analysis cannot be directly compared to Figure 3.8 or Figure 3.11, for example. Those graphs are only for isotropic damages where the faults are randomly oriented over the body in what is called "isotropic damage." The different terms in the X and Y-axis demonstrate a preferential damage direction forming an orthotropic constitutive tensor and a correspondent damage influence tensor D for the control volume (C.Vol.).

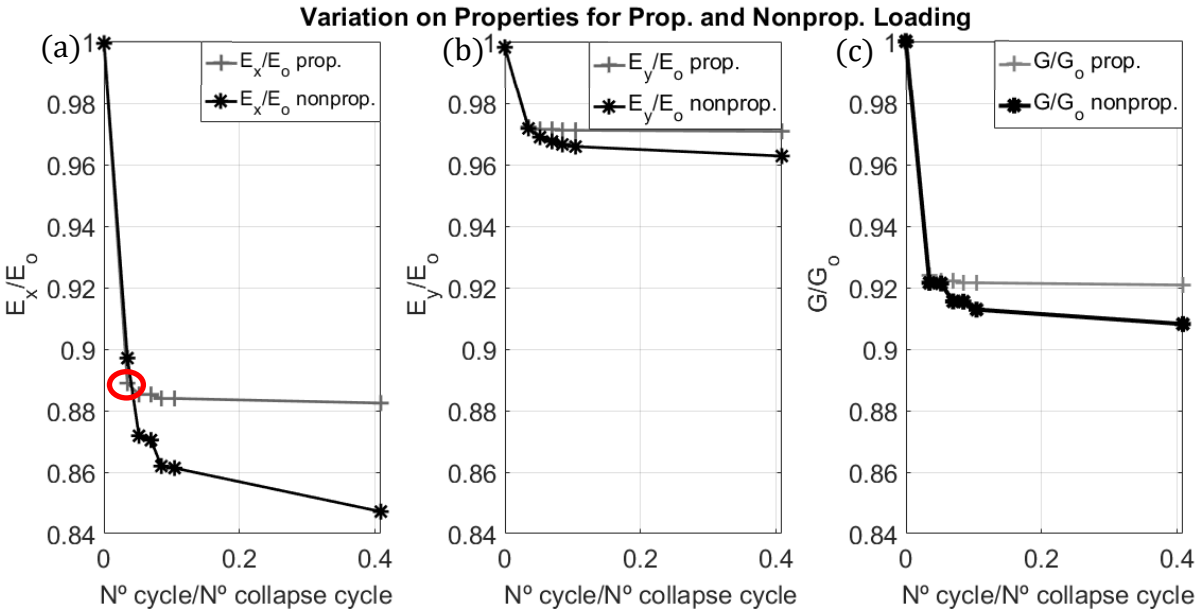

Figure 3.19 – In-plane (a) X-axis Young's moduli, (b) Y-axis Young's moduli and (c) shear moduli variation according to the relative number of cycles. Plane strain state. Comparison between the prop. and nonproportional cyclic loading. The lifespan was expanded up to 40%.

In Section 2.5, an introduction about the polarization process of constitutive tensors was displayed. The interested reader can visualize the results of the application of the MSAT ® code in Appendix D using the extracted tensors.

3.4.4 Methodology for the Domain Subdivision with Cyclic Loading

An additional study related to the 2nd Scenario was performed considering the subdivision of the structure into smaller parts. The analysis is focused on regions with fewer cubic cells to

magnify the damage localization and the changes in the properties that this causes. The report considered the following situations:

-35 x L_n by 35 x L_n: The overall domain is broken into 4 equal surfaces.
-14 x L_n by 14 x L_n: The overall domain is broken into 25 equal surfaces.
-5 x L_n by 5 x L_n: The overall domain is broken into 196 equal surfaces.

Each one of the volumes is loaded with the three previous prescribed displacement defined by a homogenous strain at the surface as implemented for the whole body. Therefore, for example, for the control volumes (C.Vols.) with 35 x L_n by 35 x L_n, 12 simulations will be necessary, while for the control volumes (C.Vols.) of 5 x L_n by 5 x L_n case, it will be implemented 588 simulations. Each C.Vol. will have its own stiffness and compliance tensor.

The area outside the volume under consideration (grey color) is neglected by reducing the stiffness of those elements to nearly zero. Figure 3.20a exemplifies the 14 x L_n by 14 x L_n case containing 25 C.Vol., while Figure 3.20b shows the 35 x L_n by 35 x L_n case defining the subdivision of the body in 4 C.Vols. It is also added the reaction forces for a prescribed displacement yielding a constant strain ε_y.

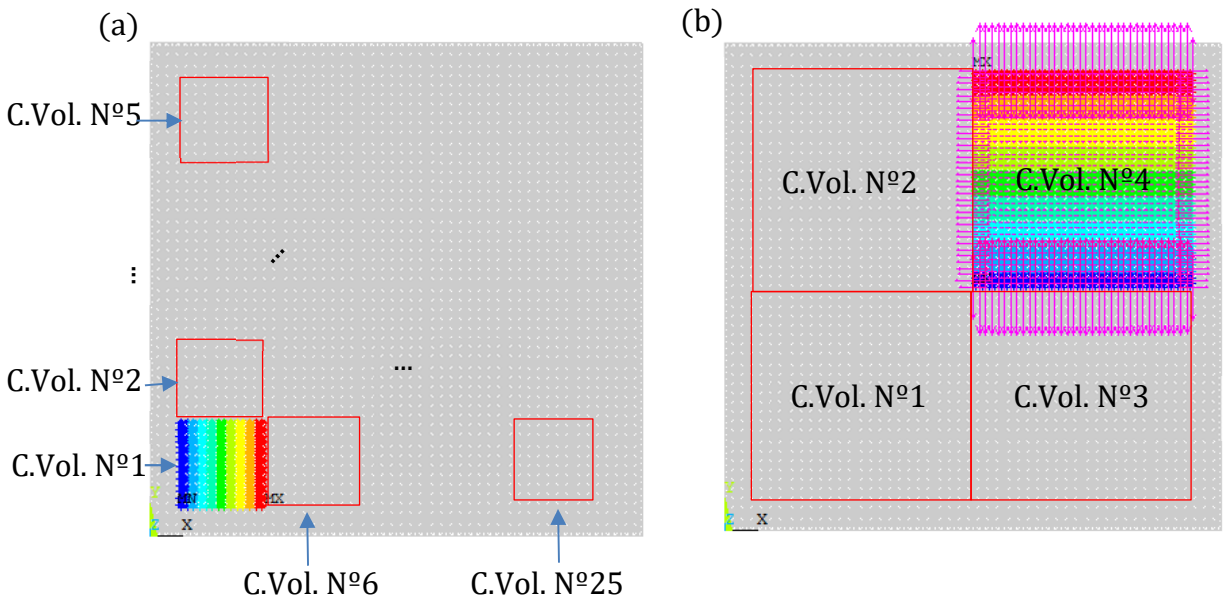

Figure 3.20 - (a) A system with 14 x L_n by 14 x L_n (25 C.Vol.). It is presented how the discretization of the total domain is performed to evaluate the properties at each volume. (b) A system with 35 x L_n by 35 x L_n (4 C.Vol.) is displayed with the force reactions at the nodes with prescribed displacement. Additional to (a) and (b), the domain is divided also with 5 x L_n by 5 x L_n (196 C.Vol.) for the cyclic loading study.

3.4.5 Results for Undamaged Subdomains

Reducing the size of the Control Volume (C.Vol.) using a DEM model has consequences. The applied boundary conditions use the central node to enforce the prescribed displacement. As the C.Vol. becomes smaller, the force fluctuations at the borders have an increasing impact on the overall results. The quantity of unitary cells decreases, meaning that the forces at the corners will have broader relevance on the averaging process. Figure 3.21a shows the case for a domain with 70 x L_n by 70 x L_n where can be clearly seen the mentioned fluctuation at each one of the four corners. Owing to these characteristics, an analysis was conducted simulation the effect of the C.Vol. size at the component $E_{x\ or\ y}$ in an undamaged structure. The evaluation considered twenty-one domains ranging from 2 x L_n by 2 x L_n up to 70 x L_n by 70 x L_n. The results are presented in Figure 3.21b. A domain with 2 x L_n by 2 x L_n will differ 5.5% from the analytical solution. However, as the C.Vol. increases, the divergence goes below 1% approaching sizes of 25 x L_n by 25 x L_n. On the other hand, the analysis of the C_{33} term, equivalent to the shear modulus G, has displayed no fluctuation at the border, leading to outputs equal to the analytical solution.

These results demonstrate that the domain size, defined by the number of unitary cells with side length L_n, establishes some inherent characteristics to the output regardless of the damage configuration. Keeping this source of error in mind, it is still possible to conduct tests reducing the C.Vol. and evaluating the impact on decreasing regions' properties.

The red arrows in Figure 3.21b indicate the Control Volumes with 5 x L_n by 5 x L_n, 14 x L_n by 14 x L_n, 35 x L_n by 35 x L_n and 70 x L_n by 70 x L_n. These are the domain sizes that will be analyzed in the next Section.

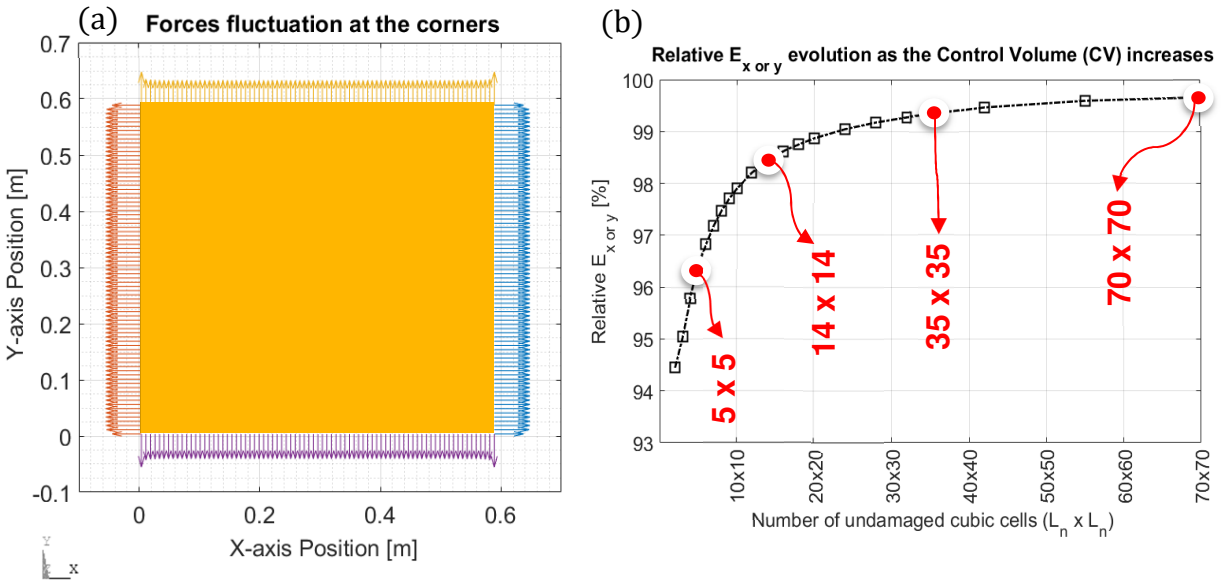

Figure 3.21 – (a) The forces fluctuations at the corner are presented. As the C.Vol. decreases in size, these perturbations affect more the constitutive terms. (b) Relative $E_{x\ or\ y}$ compared to the analytical solution for an undamaged structure according to the increasing number of C.Vols. cubic cells. Application of controlled displacements at the central node is used as load method.

3.4.6 Results for the Subdomain Study with Cyclic Loading

The total domain is subdivided into 4, 25 and 196 equal square parts that will be evaluated individually. An example for the division into four parts composed of 35 x L_n by 35 x L_n is displayed in Figure 3.22. The figures present an isometric visualization for the E_x/E_o and E_y/E_o and G/G_o in plane strain state at three different time-steps during the proportional cycling (0%, 8.5% and 99% lifespan). The X and Y-axis describe the global position, while the Z-axis represents the variation on the local properties. The proportional case was extended up until moments before the percolation (99% lifespan) to observe if the subdivision of the domain would supply more information about cluster localization and possible regions of propagation.

The loss of stiffness ceases to be a global proposition and begins to describe the local variations characterizing regions where the damage is causing a more substantial impact. This is clearer observing position (0.5, 0.5) for E_x/E_o. At that subdivision/position, the damage increases more than the others and; on the other hand, the terms E_y/E_o and G/G_o did not present considerable modification even close to the final cycles.

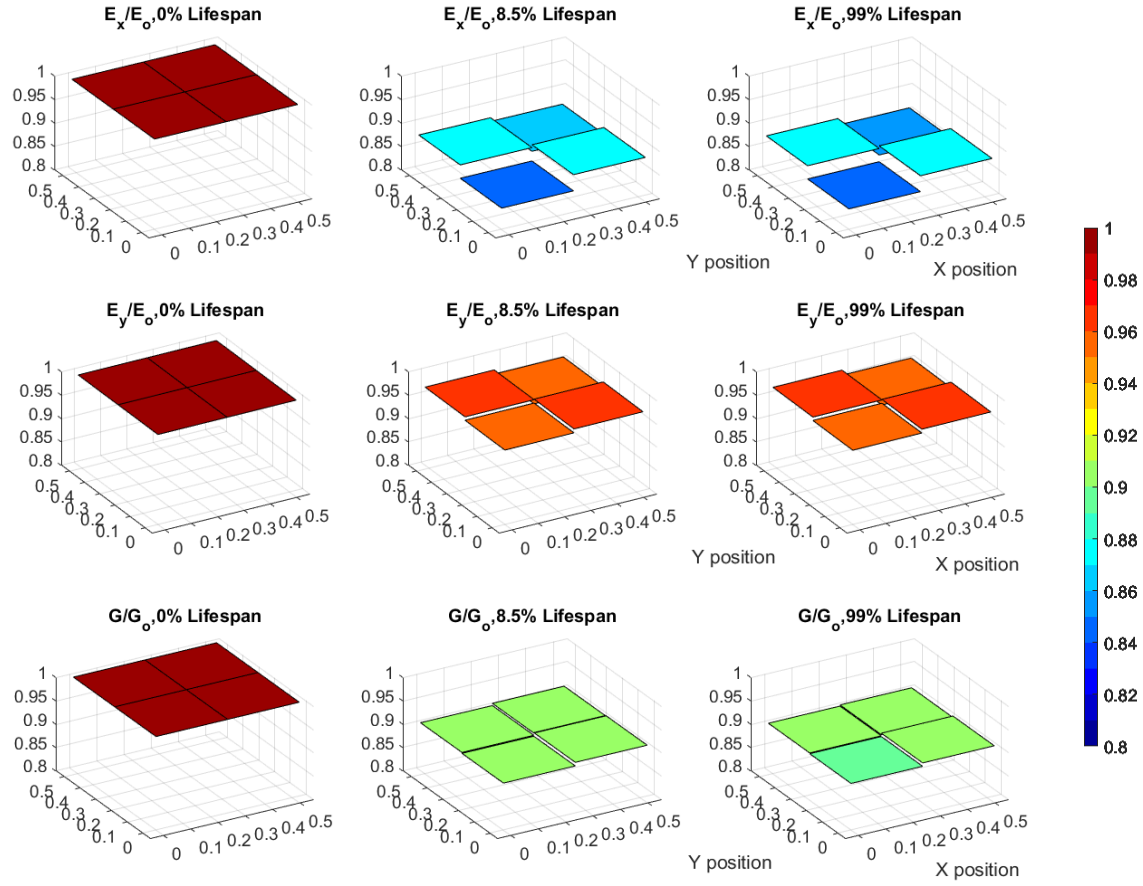

Figure 3.22 – Example of total domain subdivision. The variation at three time-steps for the properties using four subdivision. The proportional case at 0%, 8.5% and 99% of the lifespan.

A clever form to demonstrate the localization process and the loss of homogeneity is displayed in Figure 3.23. The energy release at (a) is shown along with E_x/E_o defined by different subdivisions:

(b) 1 subdivision - 70 x L_n by 70 x L_n

(c) 4 subdivisions - 35 x L_n by 35 x L_n

(d) 25 subdivisions - 14 x L_n by 14 x L_n

(e) 196 subdivisions – 5 x L_n by 5 x L_n

The time-step exemplified is at 3.5% of the lifespan indicated with a red circle in Figure 3.19.

As the discretization of the medium increases, the mechanical properties, especially in the X-axis, change accordingly with the region of faults cluster formation. At the sectors (0.1,0.1) and (0.25, 0.3) clearly E_x/E_o suffers the maximum reductions, reaching values of 0.74.

Appendix E shows the same plots for E_y/E_o and G/G_o where it can be seen that the maximum reduction reaches values of 0.88 and 0.85, respectively. Therefore, the largest damage is obviously oriented according to the X-axis sinusoidal forces, while the shear load causes much less damage in the Y-axis and in the diagonal links. Despite Figure 3.23 displaying the case for a lifespan of 3.5%, very similar plots would have been presented if the time-steps were at 5.2%, 7%, 8.5%, 10.5%, 40% or 71%. Only tiny local modifications in stiffness are observed at specific locations as the cycling grows.

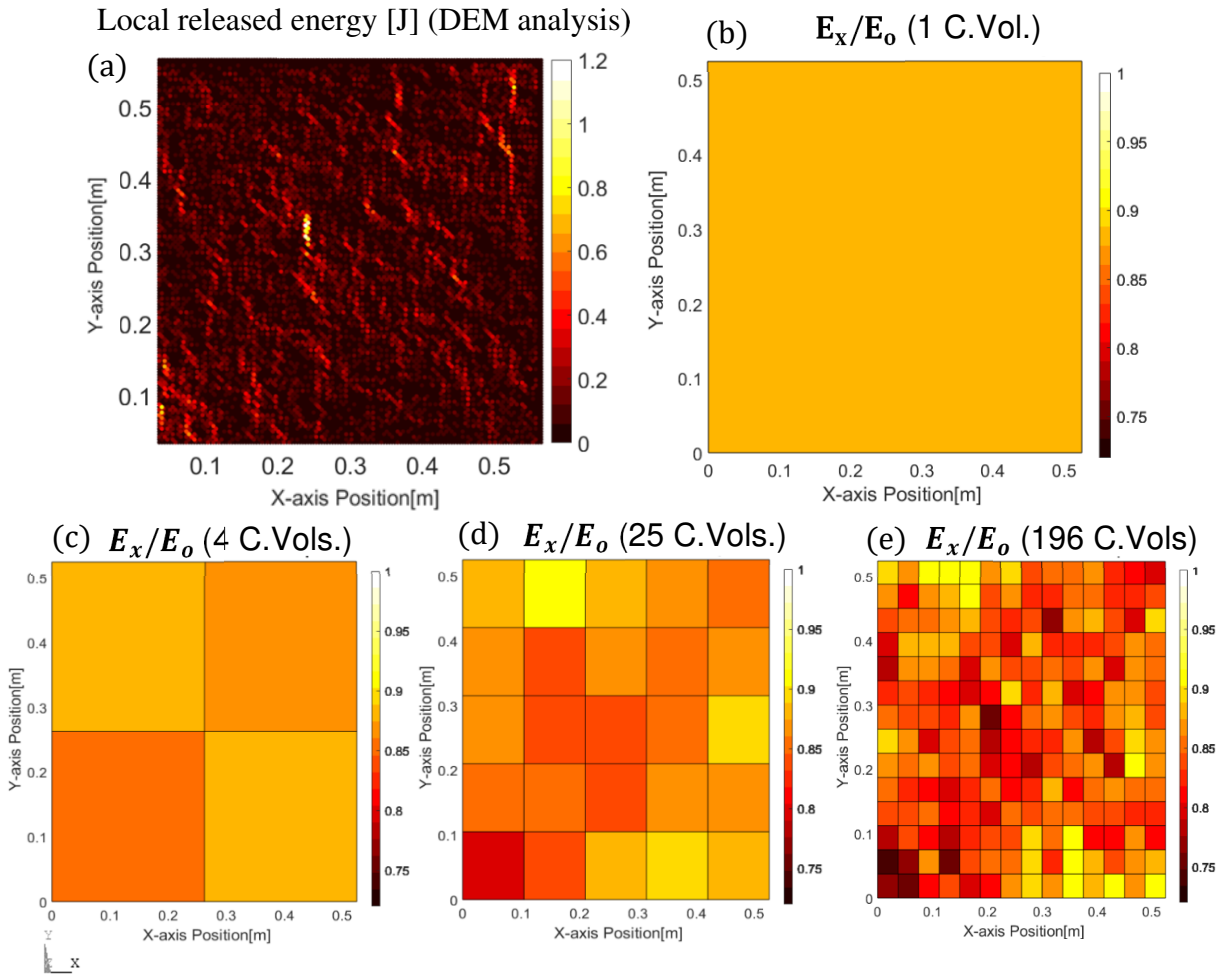

Figure 3.23 - (a) The released energy showing clusters of crack formation. (b) Plate's discretization in 1 C.Vol. (70 x L_n by 70 x L_n), (c) in 4 C.Vols. (35 x L_n by 35 x L_n), (d) in 25 C.Vols. (14 x L_n by 14 x L_n) and in 196 C.Vols. (5 x L_n by 5 x L_n). Case at 3.5% lifespan observing E_x/E_o for the proportional cyclic loading.

Another form to visualize the properties dispersion throughout the plate without considering the local variation is displayed in Figure 3.24, where the distribution of the results is presented. It is interesting to observe the averaged values for the relative E_x and E_y. Their curves are dislocated by a constant factor from the undamaged cases (blue line). This becomes

clearer for G, where the undamaged curve (red line) is not affected by the domain size as occurred for E_o. Therefore, the error associated with the method influences by a constant factor the damaged subdomains according to the size of the C.Vol.. The max. – min. difference is presented at the bottom, showing the increasing dispersion as the quantity of subdomains augments. These graphs are an additional tool to define a suitable RVE demonstrating the convergence of properties as the size of the domain reaches 70 x L_n by 70 x L_n.

As commented previously, the additional steps 5.2%, 7%, 8.5%, 10.5% or 40% present similar behavior, with the average value shifting downward by a small percentage from the one shown in the figure.

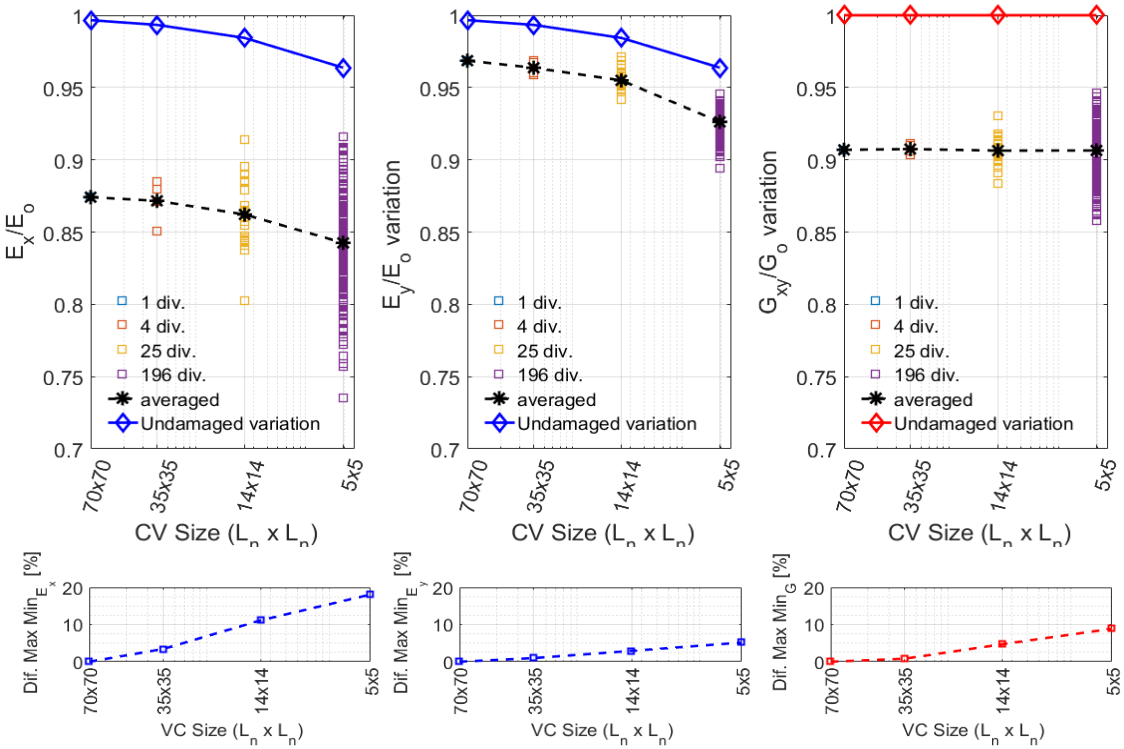

Figure 3.24 - E_x/E_o, E_y/E_o and G/G_o variation decreasing the control volume (C.Vol.) size.

The difference between max. and min. at each plot shows how the subdivision of the damaged body into smaller domains causes the dispersion of the properties caused by clusters of cracks. Case at 3.5% lifespan.

A further investigation close to the percolation, review an interesting fact about the region where the damage grows uncontrolled. Additional to changes to the relative E_x, more substantial reductions on the relative E_y and G start to appear in the northwest region of the plate. The other locations where E_x reduces does not present significant changes in E_y and G and the process of percolation is avoided in all of those regions. It seems, from the averaged

properties' point-of-view, that percolation is associated with the DEM model when the diagonal and longitudinal stiffness in X and Y-axis drop to a certain point where the resistance reaches a critical value.

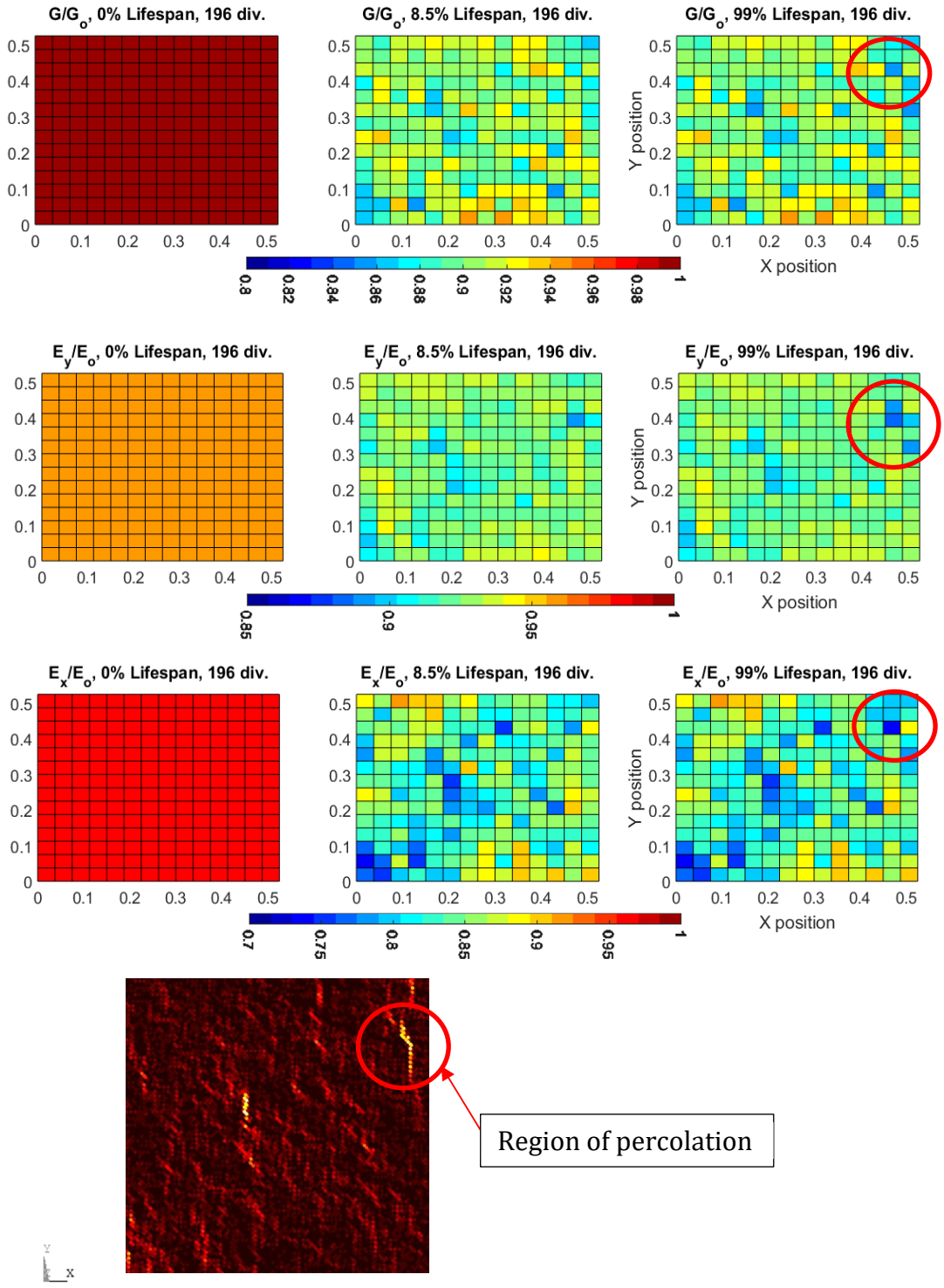

Figure 3.25 – Properties evolution up to 99% of the lifespan with the domain subdivided into 196 parts (5 x L_n by 5 x L_n). The identification of the region where percolation starts is presented with the indication that E_x, E_y and G are only evolving in that region.

All the presented data are considering that the homogenization procedure is valid under the formation of clusters and uneven distribution of cracks. This is certainly not the case when the decreasing size of the Control Volume (C.Vol.) approaches the dimension of the damaged regions, where fluctuation in stiffness mimics the crack behavior. When applying this technique, we are exchanging an approximation of the Representative Volume (RVE) for a localization procedure. The relative E or G, at some point in the subdivision process, ceases to be a valid value due to the broken homogenization hypotheses, but an additional technique to validate a consistent RVE in a damaged lattice structure is demonstrated.

3.5 Transfer from DEM to a FEA Model

Examples of conversion from DEM into the FEA model are displayed in Appendices A, B and C for a strain-controlled scenario:

Appendix A: Preprocessing – Example introducing the nodes and stiffness relation at each element. It defines the 3D structure and resulting damage at individual components for the 1st Scenario with the size of the cracks equal to 4 x L_n. Modifications to this code must be provided to adapt to the 2nd Scenario scheme. This code is written for multiply structures analysis at once.

Appendix B: Solution – Generates the solution for the subdivision process implemented in the 2nd Scenario. Parameters are set to define the size of the Control Volume (C.Vol.) and properties extraction.

Appendix C: Postprocessing – Forces at each face are stored and a file containing them is created. Later, these data will be used in Matlab ® codes to determine damage and other features.

The strain-controlled simulations were all set with a small constant strain of 1E-06 to avoid any problem regarding large deformation

4 CONCLUSIONS

The main objective of the work was to explore the connection between the discrete element results in a damaged media and the continuum mechanics parameters. Two applications were tested. The first, domains with a known isotropic distribution of defects were simulated and compared to analytical solutions. The second, a cyclically loaded structure was analyzed to observe the loss of stiffness as the damaging process grows. The following main conclusion could be extracted from these Scenarios:

-The application of such method in a structure with known crack density parameter, established a good agreement with the Self-Consistent method up to crack densities close to 0.1, despite the entirely different approaches to the problem. It was an interesting result as both methods have no relation to each other. Additionally, the numerical study of random distribution of cracks allowed the interaction of the strain/stress fields, while the analytical approach takes the assumption of considerable distancing among the faults.

-The analysis of several different random distributions with varying sizes of crack provided insights about the fluctuation that specific parameters have on the results. The length of the faults, when augmented, produced significant variations of the forces at the domain's borders, diverging the output from homogenization requirements. Contrarily, as the size of the crack decreases, the forces have little fluctuations and the dispersion tends to decrease. This is an observation that agrees with assumptions from micromechanics.

-For the same crack density parameter, small defects lead to an isotropic damage tensor when randomly spread. This happened because a large quantity of faults tends to align them equally in the X-axis and Y-axis. This fact induced similar damage in both axes. On the other side, large cracks embedded fewer cracks and, therefore, they aligned presumably in one preferential axis. That is also a reason for the higher coefficient of variance (CV) related to larger cracks compared to small ones.

-The scripts that transform the LDEM model into an FEA model permitted to evaluate the constitutive relationships naturally when studying "open" and "closed" forms without enforcing any additional or complicated method/theory. The evaluation of the term G/G_o

displayed the divergences in both schemes. The G/G_o reduction value for the "open" crack schemes was twice the "closed" one due to the different constitutive laws during compression. On the other side, the terms E/E_o, in both schemes, provided the same output for a controlled strain oriented outwards. This form of damage evaluation is highly dependent on the load applied since the relation between strain and stress can switch abruptly when the direction of the load changes. The Analyst must observe that the constitutive relations are load-dependent for the "closed" scheme.

-The model itself showed associated errors when employing the described methodology. This fact generated inconsistent results between FEA and analytical evaluations as the size of the Control Volume got smaller. The error is associated with the loading method at the border, which used the central node to apply the prescribed displacements. Additionally, the fluctuations at the corners contributed to this behavior. For example, Control Volumes with 5 x L_n by 5 x L_n displayed a deviation of around 5% for an undamaged domain. As the damage reduces the material properties by a range of 5% to 30%, these associated errors must be accounted to interpret the results.

-Despite the error associated with the size of the domain, the method was applied to analyze the study of Soares, 2019 (2nd Scenario). A proportional and nonproportional cycling process was analyzed at specific time-steps. It allowed us to investigate the impact of the faults on each direction, obtaining new stiffness or compliance tensors when a constant strain was applied outward. The "closed" crack form is selected due to the quasi-fragile material properties in compression. The results demonstrated that after initial damage, the overall properties do not change significantly on a global scale. Nevertheless, the nonproportional case has clearly caused a more significant impact on structural properties. The X-axis lost more of its stiffness and, due to this characteristic, the initial isotropic became an orthotropic medium, which is a result consistent with the energy approach detailed by Soares.

-The subdivision of the total domain into smaller subdomains lead to a localization procedure, i.e., individual subregions of the global structure were assigned with different constitutive relations. The analysis was made only for the proportional case at 3.5% of the total lifespan. The relative terms E/E_o and G/G_o were used to evaluate the discrepancies between the subdomains. It was demonstrated that as the area of the subregions reduced, the gaps in the material properties' values increased. Naturally, the RVE assumption weakens in this case and

an inverse relationship between the localization of the clusters and the definition of a consistent RVE is presented. For example, the subdivision of the structure into four subdomains (35 x L_n by 35 x L_n) showed a maximum variation for E_x/E_o of about 3% and an intrinsic error of the method of less than 1%. If an error of 4% is acceptable, it is conceivable to define each of these four subdomains as RVEs. The plot in Figure 3.24 showed that the maximum properties variation over the total domain decreases steadily as the domain increases from 5 x L_n by 5 x L_n (196 subregions) up to 35 x L_n by 35 x L_n (4 subregions). Expanding the converging curve for the three properties, it is natural to conclude that the 70 x L_n by 70 x L_n (1 subregion) case is likely to represent a consistent RVE for the domain under analysis. This type of study with multiple subdomains describes a methodology to establish an RVE for any LDEM model of interest.

-Despite the application in a varying load scenario, the ultimate goal of this technique is to be suitable to any LDEM structure at almost any damage process, e.g., fatigue, impact or load-varying cases. Some are directly applicable, while for other schemes, small changes at the codes would be required for practical implementation.

4.1 Suggestions for Future Works

All the observations above and flaws allow us to indicate some possible works to enhance or modify the present work:

-The codes presented in the Appendices can be changed to enable a study where the domain size is increased from a particular point. The idea is to define a specific point of the damaged body and to alter the size of the C.Vol. around it. The work in this dissertation presented a mapping process of the domain into smaller subdomains; therefore, this new idea would be an additional form to describe an RVE and a much quicker form to implemented due to the necessity to simulated fewer cases. The evaluation of the properties should also converge as the size of the C.Vol. reaches an even distribution of crack.

-The reasons for the corner fluctuation were not studied in-depth. Studies considering the size of the domain, variance, size of the cubic unity and application of the boundary conditions could be performed to understand what is really happening in those regions.

- The forces were applied directly using the central nodes of the cubic cells. This configuration promotes a simple form to program the load, but it also yielded fluctuations at the corners, as already discussed. It would be interesting to try to reproduce the load conditions applying the load in different nodes positioned at the borders and search the best configuration to obtain an even distribution of forces. This way, a more consistent description of the constitutive tensor can be achieved.

- The codes implemented are only for a Plane Strain State. Modifications could be made to observe how the responses would perform for a Plane Stress State. Additionally, studies in Macrostress could be carried out for the same reasons.

- Changes to the code could also be made to extract extra dimension properties, i.e., to evaluate the constitutive tensor for a 3D solid.

- Despite the application for a DEM model, nothing restricts the implementation of the homogenization technique for a pure finite element model. It is possible to apply the code to extract the properties for inhomogeneous medium and afterward implement an equivalent material to simplify any given simulation.

REFERENCES

Arbarlooie B., and Hosseini-Toudeshky H., Peridynamic micromechanical prediction of nonlocal damage initiations and propagation in DP steels based on real structure, **International Journal of Mechanical Science**, vol. 153, p. 64-74, 2019.

Anderson T. L., **Fracture Mechanics: Fundamentals and Application**, Second Edition, Department of Mechanical Engineering, Texas A&M University, College Station, USA, 1995.

Ansys ® Workbench18.2 - Ansys Mechanical Product, Ansys, Inc. Products Release 18.2. 2017.

Barbero E. J., **Finite element analysis of composite materials using Ansys®,** CRC Press – Taylor & Francis Group, USA, 2nd edition, 2014.

Bathe K. J., **Finite Element Procedures,** Prentice-Hall International Series in Prentice Hall, Upper Saddle River, 1996.

Batista R.G, **Aplicação do método dos elementos discretos ao estudo de micromecânica do dano de materiais microporosos de matriz metálica**, Thesis (Doctorate), Universidade Federal do Rio Grande do Sul, Porto Alegre, Brazil, 2007.

Belytschko T., and Black T., Elastic crack growth in finite elements with minimal remeshing, **International Journal of Numerical Methods**, vol. 45, p. 601-620, 1999.

Biswas S., Ray P., and Chakrabarti B.K., **Statistical plysics of fracture, breakdown and earthquake. Effects of disorder and heterogeneity**, Wiley-VCH, Statistical Physics of Fracture and Breakdown, 2015.

Bobinski J., and Tejchman J., **Continuous and discontinuous modelling of fracture in concrete using FEM**, Springer, Berlin-Heidelberg, 2013.

Bobinski J., and Tejchman J., Comparison of continuous and discontinuous constitutive models to simulate concrete behavior under mixed-mode failure conditions, **Fin. Elem. Anal. Des.**, vol. 40, p. 406-435, 2016.

Blanco P. J., Sanchez P. J., Souza Neto E. A., and Feijoo R. A., Variational foundations and generalized unified theory of RVE-based multiscale models, **Arch. Comp. Methods Eng.**, 2014.

Branco C. M., **Fadiga de estruturas soldadas**, Fundação Calouste Gulbenkian, Lisbon, Portugal, 1986.

Browaeys J. T., and Chevrot S., Decomposition of the elastic tensor and geophysical applications, **Geophysics Journal**, vol. 159, p.667-678, 2004.

Brunig M., and Michalski A., A stress-state-development continuum damage model for concrete based on irreversible thermodynamics, **International Journal of Plasticity**, vol. 90, p. 31-42, 2017.

Brunig M., and Michalski A., Numerical analysis of damage and failure behavior of concrete, **International Journal of Damage Mechanics**, p. 1-21, 2019.

Carazo F. D., Giusti S.M., Boccardo A. D., e Godoy L. A., Effective propertyies of nodular cast-iron: a multi-scale computational approach, **Computational Materials Science**, vol. 82, p. 378-390, 2014.

Chakrabarti, B. K., and Benguigui L. G., **Statistical physics of fracture and breakdown in disordered systems**, Oxford University Press, 1997.

Chopp D. L., and Sukumar N., Fatigue crack propagation of multiple coplanar cracks with coupled extended finite element/fast marching method, **International Journal of Engineering Science**, vol. 41, p. 845-869, 2003.

Dalguer L. A., Irikura K., and Riera J. D., Simulation of tensile crack generation by three-dimensional dynamic shear rupture propagation during an earthquake. **Journal of Geophysics**, vol. 108, p. 2144, 2003.

Evans P. H., and Marathe M. S., Microcracking and stress-strain curves for concrete in tension, **Materials and Structures (RILEM),** Vol. 1, p. 61 – 64, 1968.

Gerstle W., Sau N., and Silling S., Peridynamic modeling of concrete structures, **Nuclear Engineering and Design,** 237, p. 1250-1258, 2007.

Giusti S. M., Souza Neto E. A., Blanco P. J., and Feijoo R. A., An assessment of the gurson yield criterion by a computational multi-scale approach, **Engineering Computations**, 281, 2009.

Gross D., and Seelig T., **Fracture Mechanics – With an Introduction to micromechanics**, Mechanical Engineering Series, Springer, Germany, 2006.

Hansen A., Hemmer P.C., and Pradhan S., **The fiber bundle model, modeling failure in materials**, Wiley-VCH, Statistical Physical of Fracture and Breakdown, 2015.

Hayashi Y., **Sobre um modelo de discretização de estruturas tridimensionais aplicado em dinâmica não-Linear**, Dissertation (Master), Universidade Federal do Rio Grande do Sul, Porto Alegre, Brazil, 1982.

Hillerborg A., **A model for fracture analysis**, Division of Building Materials, The Lund Institute of technology, Lund University, 1978.

Hillerborg A., Modéer M., and Peterson A. E., Analysis of crack formation and crack growth in concrete by means of fracture mechanics and finite elements, **Cement and Concrete Research**, Vol.6, p. 773-782, Pergamon Press, 1976.

Horii H., and Nemat-Nasser S**.,** Estimate of stress intensity factors for interacting cracks, **Advances in aerospace, structures, materials and dynamics,** Vol.06, p. 111-117, ASME, USA, 1983.

Hutchinson J. W., **A Course on nonlinear fracture mechanics**, Department of Solid Mechanics, The Technical University of Denmark, 1979.

Iturrioz I., Lacidogna G., and Carpinteri A., Experimental analysis and truss-like discrete element model simulation of concrete specimens under uniaxial compression, **Engineering Fracture Mechanics**, vol. 110, p. 81-98, 2013.

Ibijola E. A., On some fundamental concepts of continuum damage mechanics, **Computer methods in applied mechanics and engineering**, vol. 191, p. 1505-1520, 1998.

Iturrioz I., **Aplicação do método dos elementos discretos ao estudo de estruturas laminares de concreto armado**, Tese (Doutorado), Universidade Federal do Rio Grande do Sul, Porto Alegre, Brasil, 1995.

Iturrioz I., Lacidogna, G., w Carpinteri A., Experimental analysis and truss-like discrete element model simulation of concrete specimens under uniaxial compression, **Engineering Fracture Mechanics,** vol. 110, p. 81-98, 2013.

Iturrioz I., Miguel L. F. F., and Riera J. D., **Dynamic fracture analysis of concrete or rock plates by means of the discrete element method**. LAJSS, vol. 6, p. 229–245, 2009.

Javanmardi M.R., and Maheri M. R., Extended finite element method and anisotropic damage plasticity for modelling crack propagation in concrete, **Finite Elements in Analysis and Design**, vol. 165, p. 1-20, 2019.

Jasiuk I., Chen J., and Thorpe M. F., Elastic Moduli of two-dimensional materials with polygonal and elliptical holes, **Applied Mechanics Reviews,** 1994.

Kachanov L., Time of the rupture process under creep conditions, **TVZ Akad Nauk S.S.R. Otd. Tech. Nauk**, vol. 8, p. 26-31,1958.

Kelly P. A., **Mechanics lectures notes**, Department of Engineering Science, University of Auckland, 2015.

Klichowicz M., Fruhwirt T., and Lieberwirth H**., New experimental setup for the validation of DEM simulation of brittle crack propagation at grain size level, Minerals Engineering**, vol. 128, p. 312-323, 2018.

Kosteski L. E., **Aplicação do método dos elementos finitos discretos formado por barras no estudo do colapso de estruturas**, Tese (Doutorado), Universidade Federal do Rio Grande do Sul, Porto Alegre, Brasil, 2012.

Kosteski, L. E., Iturrioz, I., and Barrios, R., Crack propagation in elastic solids using the truss-like discrete element method, **International Journal of Fracture**, vol. 174, p. 139-161, 2012.

Kosteski, L. E., Iturrioz, I., Batista, R. G., and Cisilino, A. P., The truss-like discrete element method in fracture and damage mechanics**. Engineering Computations**, vol. 6, p. 765-787, 2011

Kousznetsova V. G, **Computational homogenization for the multi-scale analysis of multi-phase materials**, Thesis (Doctorate). Technische Universiteit Eindhoven, Eindhoven, Netherlands, 2002.

Krajcinovic D., and Vujosevic M., Intrinsic failure modes of brittle materials, **Int. J. Solids Structures**, Vol. 35, p. 2487-2503, 1998.

Krajcinovic, D. **Damage mechanics**, North-Holland, Amsterdam, 1996.

Kupfer H., Hilsdorf H., e Rusch H., Behavior of concrete under biaxial stresses, **ACI Journal**, vol. 66, p. 653-666.

Landes J. D., and Begley J. A., The J-Integral as a fracture criterion, **American Society for Testing and Materials**, ASTM STP 514**,** p.1-20, USA, 1972.

Lemaitre J., and Desmorat R., **Isotropic and anisotropic Damage Law of Evolution**, Handbook of Materials Behavior, France, 2001.

Lemaitre J., and Dufailly J., **Damage measurements**, Engineering Fracture Mechanics, Vol.28, No 6.6, p. 643-661, UK, 1987.

Lemaitre J., How to use damage mechanics, **Nuclear Engineering and Design**, vol. 90, p. 233-245, Netherland, 1984.

Lerma A. F., Alarcon-Fleming A., and Alvarez E. A., **AF.4 Material constitutive laws**, International Master in Theoretical & Practical Application of Finite Element Methods and CAE Simulation, E.T.S.I. Industriales – U.P.M, Spain, 2018.

Lurie S., Solyaev Y, and Sharmko K., **Comparison between the Mori-Tanaka and generalized self-consistent methods in the framework of anti-plane strain inclusion problem in strain gradient elasticity**, Mechanics of materials, vol. 122, p. 133-144, 2018.

Madenci E., and Oterkus E., **Peridynamic theory and its applications**, Springer Science & Business Media, New York, 2014.

Matlab ® R2016a, MathWorks, Inc, 2016.

Mehrmashhadi J., Chen Z., Zhao J., and Bobaru F., A stochastically homogenized peridynamic model for intraply fracture in fiber-reinforced composites, **Composites Science and Technology**, vol. 182, 2019.

Mori T., and Tanaka K**., Average stress in matrix and average elastic energy of materials with misfitting inclusions, Acta Metallurgica,** vol. 21 (5), p. 571–574, 1973.

MSAT ® Version 1.1.0, MATLAB ® Seismic Anisotropy Toolkit, Copyright and rights by James Wookey and Andrew Walker, 2012.

Mura T., **Micromechanics of defects in solids**, Northwestern University, Martinus Nujhoff Publishers, USA, 1983.

Nagy E., Landis E. N., and David W.G., Acoustic emission measurements and lattice simulations of microfracture events in spruce, **Holzforschung**, vol. 64, p. 455-461, 2010.

Nayfeh A. H, and Hefzy M. **S., Continuum modeling of three-dimensional truss-like space structures. AIAA Journal,** vol. 16 (8), p. 779-787, 1978.

Nemat-Nasser S., and Hori M., **Micromechanics: overall properties of heterogeneous materials.** North-Holland Series in Applied Mathematics and Mechanics, 1999.

Nitka M., and Tejchman J., Meso-mechanical modelling of damage in concrete using discrete element method with porous ITZs of defined width around aggregates, **Engineering Fracture Mechanics**, vol. 231, 2020.

Oliver J., Caicedo M., Roubin E., Huespe A. E., e Hernandez J. A., **Continuum approach to computational multiscale modeling of propagating fracture**, Computational Methods Appl. Mechanical Engineering,2 294, pp. 384-427, 2015.

Osher S., and Sethian J., Fronts propagating with curvature dependent speed: algorithms based on Hamilton-Jacobi formulations, **Journal of Computational Physics**, vol. 79, p. 12-49, 1988.

Papanikolaou V.K., and Kappos A.J., Confinement-sensitive plasticity constitutive model for concrete in triaxial compression, **International Journal of Solids and Structures,** 44, p. 7021-2048, 2007.

Rice J. R., Levy N., Marcal P. V., e Ostergren W.J., Small scale yielding near a crack in plane strain: A finite element analysis, **International Journal of Fracture Mechanics**, vol. 7, p.143-156, 1971.

Richard B., e Ragueneau F., Continuum damage mechanics based model for quasi brittle materials subjected to cyclic loading: formulation, numerical implementation and application, **Engineering Fracture Mechanics**, vol. 98, p. 383-406, 2013.

Richard B., Ragueneau F., Cremona C., and Adelaide L,., Isotropic continuum damage mechanics for concrete under cyclic loading: stiffness recovery, inelastic strains and frictional sliding, **Engineering Fracture Mechanics**, vol. 77, p. 1203-1223, 2010.

Riera J. D., and Iturrioz I., Discrete elements model for evaluating impact and impulsive response of reinforced concrete plates and shells subjected to impulsive loading, **Nuclear Engineering and Design**, vol. 179, p. 135-144, 1998.

Riera J. D, Local effects in impact problems on concrete structures, **Conference on Structural Analysis and Design of Nuclear Power Plants**, Vol.3, 1984.

Riera, J. D., e Iturrioz, I., Discrete element dynamic response of elastoplastic shells subjected to impulsive loading**, Communications in Numerical Methods in Engineering**, vol. 11, p. 417-426, 1995.

Riera J. D., and Rocha, M. M., A note on velocity of crack propagation in tensile fracture, **Revista Brasileira de Ciências Mecânicas**, vol. XII/3, p. 217-240, 1991.

Rinaldi A., **Damage Mechanics and micromechanics of localized fracture phenomena in inelastic solids**, CISM Courses Series, Springer, 2011.

Rinaldi A., Krajcinovic D., and Mastilovic S., **Statistical damage mechanics – constitutive relations,** Journal of Theoretical and Applied Mechanics, 44, vol. 3, p 585-602, Warsaw, 2006.

Rios R. D., and Riera J. D., **Size effects in the analysis of reinforced concrete structures,** Engineering Structures, vol. 26, p. 1115-115, 2004.

Rocha M. M., Riera, J. D., and Krutzik, N. J., Extension of a model that aptly describes fracture of plain concrete to the impact analysis of reinforced concrete, **International Conference and Structural Mechanics in Reactor Technology,** Vol. J, Japan, 1991.

Rocha M. M., **Ruptura e efeitos de escala em materiais não homogêneos**, Dissertation (Master), Universidade Federal do Rio Grande do Sul, Porto Alegre, Brazil, 1989.

Rodrigues R. S.**, Índices de dano aplicáveis a materiais quase-frágeis avaliados utilizando o método dos elementos discretos formado por barras**, Dissertation (Master), Universidade Federal do Rio Grande do Sul, Porto Alegre, Brazil, 2015.

Sagar R. V., and Prasad B.K., Modeling heterogeneity of concrete using 2D lattice network for concrete fracture and comparison with AE study, **Sadhana,** vol. 34(6), p. 865-886, 2009.

Sarikaya A., and Erkmen R.E., A plastic-damage model for concrete under compression, **International Journal of Mechanical Sciences**, vol.150, p. 584-593, 2019.

Schlangen E., and van Mier J.G.M**, Crack propagation in sandstone: combined experimental and numerical approach, Rock Mechanics and Rock Engineering**, vol. 28, p. 93-110, 1995.

Silling S. A., Reformulation of elasticy theory for discontinuities and long-range forces, **Journal of the Mechanics and Physics of Solids**, vol. 48, p. 175-209, 1999.

Silling S. A. et al**., Peridynamics states and constitutive modeling**, **Journal of Elasticity**, vol. 88, p. 151–184, 2007.

Soares F. S., **Modelagem de fenômenos de fadiga em materiais quase frágeis heterogêneos utilizando uma versão do método de elementos discretos formado por barras**, Thesis (Doctorate), Universidade Federal do Rio Grande do Sul, Porto Alegre, Brazil, 2019.

Stolarska M., Chopp D. L., Moes N., and Belyschko T., Modelling crack growth by level sets in the extended finite element method, **International Journal of Numerical Methods**, vol. 51, p. 943-960, 2001.

Sukumar N., Srolovitz J., Baker T., and Prevost J., Brittle fracture in polycrystalline microstructures with extend finite element method, **International Journal of Numerical Methods**, vol. 56, p. 2015-2037, 2003.

Sukumar N., Chopp D. L., Bechet E., ans Moes N., Three-dimensional non-planar crack growth by a coupled extended finite element and fast marching method, **International Journal of Numerical Methods**, vol. 76, p. 727-748, 2008.

Svoboda L. et al., **uMech micromechanics library**, Advances in Engineering Software, 100, pp. 148-160, Prague, 2016.

Tao R., Sharifzadeh M., Zhang Y., and Feng X. T., Analysis of mafic rocks microstructure damage and failure process under compression test using quantitative scanning electron microscopy and digital images processing, **Engineering Fracture Mechanics**, vol. 231, 2020.

Ventura G., On elimination of quadrature subcells for discountinous functions in the extended finite element method, **International Journal of Numerical Methods**, vol. 66, p. 761-795, 2006.

Voyiadjis G. Z., Taqieddin Z. N., and Kattan P. I., Anisotropic damage-plasticity model for concrete, **Internationla Journal of Plasticity**, p. 1946-1965, 2008

Walker A.M., andWookey J.M., **MSAT – A new toolkit for the analysis of elastic and seismic anisotropy**, School of Earth Science, University of Bristol, 2012.

Well A. A., **Unstable crack propagation in metals: cleavage and fast Ffacture**, Proceedings of the Crack Propagation Symposium, Vol. 1, Paper 84, Cranfield, UK, 1961.

Wang P., Gao N., Ji K., and Stewart L., Arson C., DEM analysis on the role of aggregates on concrete strength, **Computers and Geotechnics**, vol. 119, 2020.

Wu J. Y., Li J., and Faria R., An energy release rate-based plastic-damage model for concrete, **International Journal of Solids and Structures**, vol. 43, p. 583-612, 2005.

Yaghoobi A., and Chorzepa M.G., Fracture analysis of fiber reinforced concrete structures in the micropolar peridynamic' analysis framework, **Engineering Fracture Mechanics**, vol. 169, p. 238-250, 2017.

Yazid A., Abdelkader N., and Abdelmadjid H., A state-of-the-art review of the X-FEM for computational fracture mechanics, **Applied Mathematical Modelling**, vol. 33, p. 4269-4282, 2009.

Zhang W., and Cai Y., **Continuum damage mechanics and numerical applications**, Zhejiang University Press, China, 1995.

Zohdi T.I., **Computational modeling and design of new random microheterogeneous materials**, CISM Course Notes, 2002.

APPENDIX A – Scripts for Ansys: Prep7

The script below was developed using Ansys® APDL for the implementation of the 3D lattice structure simulating the DEM structure. The script can only be used for Ansys® version superior to v.17 due to the change in Link180 APDL commands. It is introduced in Appendix A only the preparation commands (\PREP7) to define the nodes coordinates, the elastic properties and section areas of each element (stiffness characterization). The example is for a routine for a random distribution of crack produced by the FORTRAN code.

```
!ARQUIVO NO TEMPO =  0.00E+000
/PREP7
/TITLE, TEMPO =  0.00E+000
ET,1,link180
Em = 35000000000.00
MP,EX,1,Em


! Coordinates for each node of the structure up until N = 19041.
N,      1       ,       0       ,       0                       ,       0
N,      2       ,       0.0075  ,       0                       ,       0
N,      3       ,       0.015   ,       0                       ,       0
N,      4       ,       0.022500001     ,       0               ,       0
N,      5       ,       0.029999999     ,       0               ,       0
….
! Only represented 5 nodes with x, y and z coordinates. The overall number of nodes go up to 19041 nodes.
! Each element is defined below according to the description:

! The name of the file with the stiffness information is “Z_XXYY” with the first column for non-damaged bar (column 1) and a second column with damaged bars (column 2).
! This example is for Z = 1 (the first structure of five that will be evaluated – 1st Scenario case). YY = 03 (the size of the crack is 03+1 -> 4). XX= 1:13 (there is 13 cases changing the density crack parameter).

Z = '1'   ! Number of the random distribution of cracks (file)
YY = '03'  ! Size of the crack (file)
*DO, XX,1,1,13   ! Number of crack file
Z_XXYY  = '%Z%_%XX%%YY%'
AA = '%Z%_%XX%%YY%POSX'
BB = '%Z%_%XX%%YY%Y'
CC = '%Z%_%XX%%YY%XY'

N_D = 93933      ! Column for non-damaged bar (column 1)
D = 93934        ! Column for damaged bar (column 2)
nelem = 93932
to_skip=0

! An additional file attached called “connect” must contain the connectivity.

/INQUIRE,numlines1,LINES,Z_XXYY,txt
/INQUIRE,numlines2,LINES,connect,txt
to_read1 = numlines1-1
to_read2 = numlines2-1
*DIM,M_dano,TABLE,to_read1,2
*DIM,connecti,TABLE,to_read2,2
*TREAD,M_dano,Z_XXYY,txt,,to_skip
```

```
*TREAD,connecti,connect,txt,,to_skip

! Below the iteration to create a damaged and undamaged structure with 93932 elements each. The total amount of link 180 elements will be of 187864, containing two bars at each position. One for compression and another for traction.
! SECTYPE: Defines the type of element. In this case, Link180, which is a line/bar element, is applied. Just traction and compression accepted.
! SECDATA: Defines the cross-section of each link element. It varies according to damage and position on the structure.
! SECCONTROL: defines if the element responds to loading only under traction (1) or compression (-1). All the elements are duplicated.
! E: defines the connectivity. It represents the nodes at which the element begins (i-coordinates) and ends (j-coordinates).

*DO,i,1,nelem
SECTYPE,i,LINK
SECDATA,M_dano(i,D)
SECCONTROL,,1
SECNUM,i
E,connecti(i,N_D),connecti(i,D), !EL i
*ENDDO

*DO,j,1,nelem
SECTYPE,j+nelem,LINK
SECDATA,M_dano(j,N_D)
SECCONTROL,,-1
SECNUM,j+nelem
E,connecti(j,N_D),connecti(j,D), !EL i
*ENDDO

! The file below is called to generate the load necessary to capture the properties. Appendix B (\Solu)
/input, Z_RXXYYPOS,txt
```

APPENDIX B – Scripts for Ansys: Solu

Appendix B introduces the solution (\Solu) for the preprocessing system assembled in appendix A (\Prep7). The following code corresponds to the prescribed displacement at the C.Vol. boundaries on the x-axis. The same procedure must be done for the load at the y-axis and xy-plane (shear). These two last scripts will not be presented here, but can be easily derived from the given script. The domain described is formed by 1 x 1 group (70 x 70 cells). To create, per example, four domains, it would be necessary to change to "cel=35" and "FS=2". This would imply in 2 x 2 groups (35 x 35 cells).

```
/SOLU
ANTYPE, STATIC
NLGEOM, ON
def=1E-6        ! Prescribed constant strain (not change)
L=0.0075        ! Size in meters of each cell (not change)
cel=70          ! Number of unit cells for each iteration
FS=1            ! Number of interactions at each axis
IL=1            ! Initial loop position
K=0.00175       ! Offset for ekill procedure
G=(L)/2
OS=4            ! Offset of cell x and y directions

*DO,q,IL*cel,FS*cel,cel
*DO,j,IL*cel,FS*cel,cel

        YInf1=L*(j-cel)+(2*OS+1)*L/2
        Ysup1=L*(j)+(2*OS+1)*L/2
        Xsup1=L*(q)+(2*OS+1)*L/2
        Xinf1=L*(q-cel)+(2*OS+1)*L/2

        LSCLEAR, ALL
        EKILL, ALL
        EALIVE, ALL
        DOFSEL, S, U
        DDELE, ALL

! Select nodes with prescribed displacement

NSEL,   S,      LOC,    Z,      0
D,      ALL,    UZ,     0.00E+00
NSEL,   ALL,
NSEL,   S,      LOC,    Z,      L
D,      ALL,    UZ,     0.00E+00
NSEL,   ALL,
NSEL,   S,      LOC,    Z,      L/2     ,
NSEL,   R,      LOC,    Y,      Yinf1-K,        Ysup1+K
NSEL,   R,      LOC,    X,      Xsup1-L/2       ,       Xsup1+L/2
D,      ALL,    UX,     (Def*(Xsup1)-0.29625E-6)

D,      ALL,    UY,     0
NSEL,   ALL,
NSEL,   S,      LOC,    Z,      L/2     ,
NSEL,   R,      LOC,    Y,      Yinf1-K,        Ysup1+K
NSEL,   R,      LOC,    X,      Xinf1-L/2       ,       Xinf1+L/2
```

```
D,      ALL,    UX,     (Def*(Xinf1)-0.29625E-6)
D,      ALL,    UY,     0
NSEL,   ALL,

NSEL,   S,      LOC,    Z,      L/2     ,
NSEL,   R,      LOC,    X,      Xinf1-K ,       Xsup1+K
NSEL,   R,      LOC,    Y,      Ysup1-L/2       ,       Ysup1+L/2
D,      ALL,    UY,     0
NSEL,   ALL,

NSEL,   S,      LOC,    Z,      L/2     ,
NSEL,   R,      LOC,    X,      Xinf1-K ,       Xsup1+K
NSEL,   R,      LOC,    Y,      Yinf1-L/2       ,       Yinf1+L/2
D,      ALL,    UY,     0
NSEL,   ALL,
```

! Kill the elements by the side of each region

```
        ESEL,   S,      CENT,   X,      Xsup1+K         ,       0.6
        ESEL,   A,      CENT,   X,      0       ,       Xinf1-K
        ESEL,   A,      CENT,   Y,      Ysup1+K         ,       0.6
        ESEL,   A,      CENT,   Y,      0       ,       Yinf1-K
        CM, AMEM, ELEM
        EKILL, AMEM
        ESEL, ALL

        SOLVE

SAVE
```

! An additional load with zero is proposed to cancel de displacement from previous loading. “It is a trick”.

```
LSCLEAR, ALL
        EKILL, ALL
        EALIVE, ALL
        DOFSEL, S, U
        DDELE, ALL
```

! Select nodes with prescribed displacement

```
NSEL,   S,      LOC,    Z,      0
D,      ALL,    UZ,     0.00E+00
NSEL,   ALL,
NSEL,   S,      LOC,    Z,      L
D,      ALL,    UZ,     0.00E+00
NSEL,   ALL,
NSEL,   S,      LOC,    Z,      L/2     ,
NSEL,   R,      LOC,    Y,      Yinf1-K ,       Ysup1+K
NSEL,   R,      LOC,    X,      Xsup1-L/2       ,       Xsup1+L/2
D,      ALL,    UX,     0
D,      ALL,    UY,     0
NSEL,   ALL,

NSEL,   S,      LOC,    Z,      L/2     ,
NSEL,   R,      LOC,    Y,      Yinf1-K ,       Ysup1+K
NSEL,   R,      LOC,    X,      Xinf1-L/2       ,       Xinf1+L/2
D,      ALL,    UX,     0
D,      ALL,    UY,     0
```

```
NSEL,   ALL,


NSEL,   S,      LOC,    Z,      L/2     ,
NSEL,   R,      LOC,    X,      Xinf1-K ,       Xsup1+K
NSEL,   R,      LOC,    Y,      Ysup1-L/2       ,       Ysup1+L/2
D,      ALL,    UX,     0
D,      ALL,    UY,     0
NSEL,   ALL,

NSEL,   S,      LOC,    Z,      L/2     ,
NSEL,   R,      LOC,    X,      Xinf1-K ,       Xsup1+K
NSEL,   R,      LOC,    Y,      Yinf1-L/2       ,       Yinf1+L/2
D,      ALL,    UX,     0
D,      ALL,    UY,     0
NSEL,   ALL,

! Kill the elements by the side of each region

ESEL,   S,      CENT,   X,      Xsup1+K         ,       0.6
ESEL,   A,      CENT,   X,      0       ,       Xinf1-K
ESEL,   A,      CENT,   Y,      Ysup1+K         ,       0.6
ESEL,   A,      CENT,   Y,      0       ,       Yinf1-K
CM, AMEM, ELEM
EKILL, AMEM
ESEL, ALL

                SOLVE

        SAVE

*ENDDO
*ENDDO
```

APPENDIX C – Scripts for Ansys: Post1

Appendix C is related to the post-processing script (\Post1) used to collect the data generated during the Appendix A/B script. Below, the shear forces are collected and stored in a file "XY_1_1" (example). The case is for a domain of 1x1 (70 x 70 cells).

```
! Example for the Post-processed script to collect data from the shear solution (XY). The same procedure can be made for "ForcaX" and "ForcaY" with little changes.

/POST1
*DIM, FORCAXY,,1,4
*DO,q,IL*cel,FS*cel,cel
*DO,j,IL*cel,FS*cel,cel

        YInf1=L*(j-cel)+(2*OS+1)*L/2
        Ysup1=L*(j)+(2*OS+1)*L/2
        Xsup1=L*(q)+(2*OS+1)*L/2
        Xinf1=L*(q-cel)+(2*OS+1)*L/2
        t=((q/cel) - 1)*FS+j/cel
        M=2*t-1
                SET,M
                NSEL,   ALL,
                NSEL,   S,      LOC,    Z,      L/2     ,
                NSEL,   R,      LOC,    Y,      Yinf1-K,        Ysup1+K
                NSEL,   R,      LOC,    X,      Xsup1-L/2       ,       Xsup1+L/2       FSUM, FY
*GET, FORCAXY(1,1), FSUM,0,ITEM,FY

NSEL,   ALL,
NSEL,   S,      LOC,    Z,      L/2     ,
NSEL,   R,      LOC,    Y,      Yinf1-K,        Ysup1+K
NSEL,   R,      LOC,    X,      Xinf1-L/2       ,       Xinf1+L/2
FSUM, FY
*GET, FORCAXY(1,2), FSUM,0, ITEM, FY

NSEL,   ALL,
NSEL,   S,      LOC,    Z,      L/2     ,
NSEL,   R,      LOC,    X,      Xinf1-K,        Xsup1+K
NSEL,   R,      LOC,    Y,      Ysup1-L/2       ,       Ysup1+L/2
FSUM, FX

*GET, FORCAXY(1,3),FSUM,0,ITEM,FX
        NSEL,   ALL,
        NSEL,   S,      LOC,    Z,      L/2     ,
        NSEL,   R,      LOC,    X,      Xinf1-K,        Xsup1+K
        NSEL,   R,      LOC,    Y,      Yinf1-L/2       ,       Yinf1+L/2
        FSUM, FX
        *GET,FORCAXY(1,4),FSUM,0,ITEM,FX
        NSEL,   ALL,



*CFOPEN, XY1_1,'txt', , APPEND
*VWRITE, FORCAXY(1,1), FORCAXY(1,2), FORCAXY(1,3), FORCAXY(1,4)
(E15.6, E15.6, E15.6, E15.6)
*cfclos
```

```
*ENDDO
*ENDDO
etable, epelxyi, lepel, 1
etable, sxy, ls, 1
etable, forcexy, smisc, 1
etable, area, smisc,2
```

APPENDIX D – Constitutive Matrix Decomposition: anistropy analysis

The application of the MSAT ® program described in Section 2.5 can be used to decompose the constitutive matrix in order to separate the isotropic and non-isotropic parts, as explained previously. However, we are going to assume that only in-plane can undergo changes in their isotropy conditions. Therefore, out-of-plane entries are prescribed as in an undamaged state. Decomposing the extracted tensors using Equation (2.70), a percentage for each type of tensor shown in Equation (2.69) can be obtained. Figure D.1 shows the results for nonproportional and proportional loading. The lifespan analysis was increased up to 70%, indicating the convergence of both curves. As expected, the isotropic state was established as 95.5% for the proportional loading and 94% for the nonproportional loading. It agrees with the statement that the nonproportional damage causes more damage leading the material to a "more" orthotropic description. The solution also states that most of the domain does not have large drops in the isotropic configuration. The directional properties are small, which keeps the body mainly isotropic despite the substantial damage during cycling.

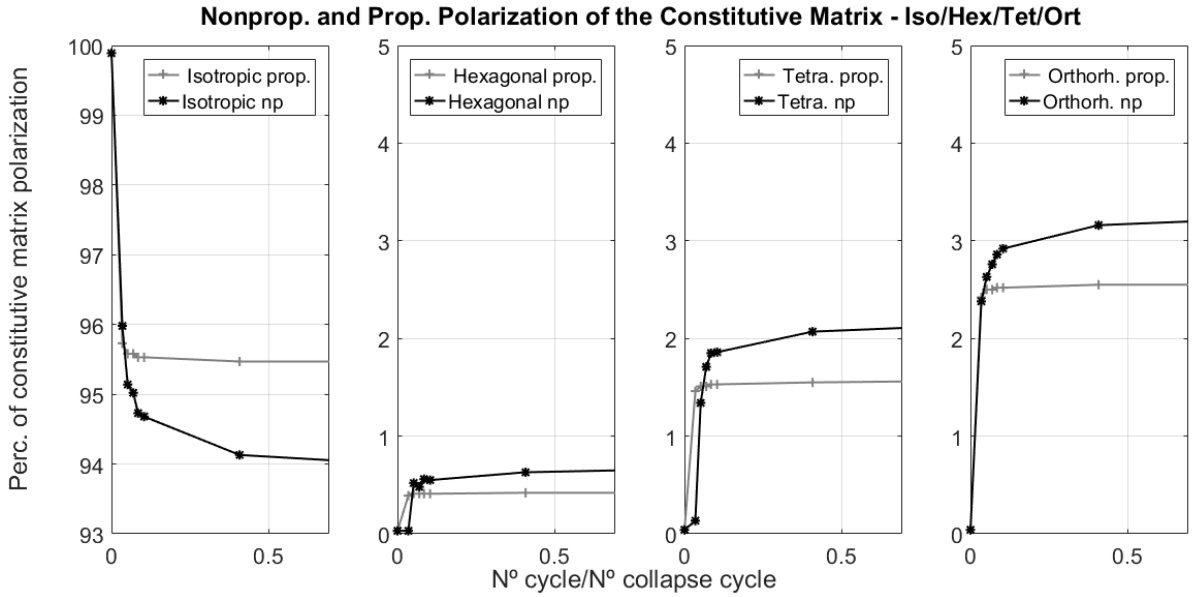

Figure D.1 – Anisotropy for proportional and nonproportional loading. The differences contemplate the idea that the nonproportional case is more severe, inducing greater perturbation at the stiffness matrix. The lifespan was increased up to 70%.

APPENDIX E – Results for the Subdivision Analysis for Ey and G

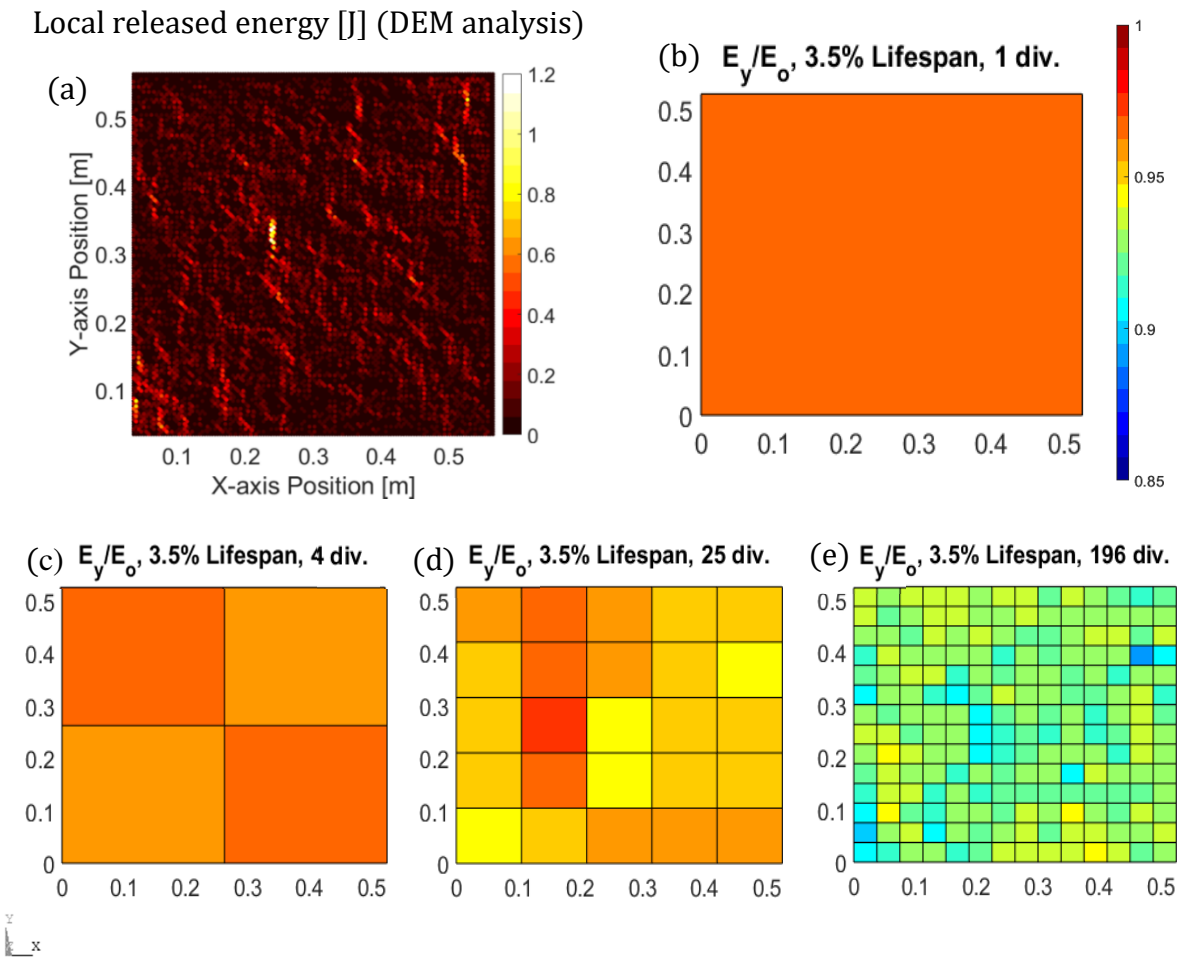

Figure E.1 - (a) The released energy showing clusters of crack formation. (b) Plate's discretization in 1 C.Vol. (70 cubic LDEM modules of side), (c) in 4 C.Vols. (35 cubic LDEM modules of side), (d) in 25 C.Vols. (14 cubic LDEM modules of side) and in 196 C.Vols. (5 cubic LDEM modules of side). Case at 3.5% lifespan observing E_y/E_o for the proportional cyclic loading.

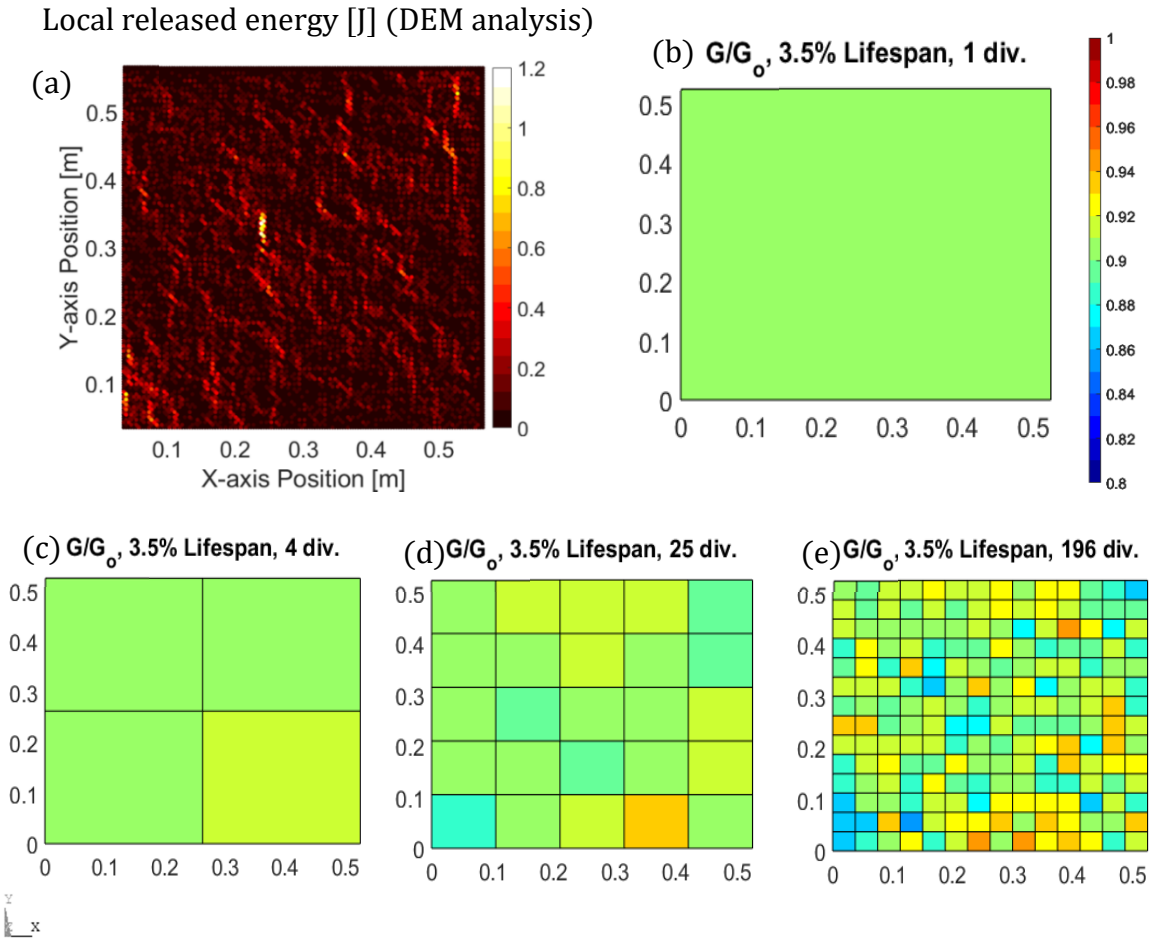

Figure E.2 - (a) The released energy showing clusters of crack formation. (b) Plate's discretization in 1 C.Vol. (70 cubic LDEM modules of side), (c) in 4 C.Vols (35 cubic LDEM modules of side), (d) in 25 C.Vols (14 cubic LDEM modules of side) and in 196 C.Vols. (5 cubic LDEM modules of side). Case at 3.5% lifespan observing G/G_o for the proportional cyclic loading.

APPENDIX F – Article submitted for Approval in a Scientific Journal

Continuum damage evaluation in quasi-fragile materials simulated using a lattice discrete element method

Abstract

The simulation of the damage process is a challenge for researchers nowadays. In ductile materials, the continuum damage mechanics is based on the plasticity framework, but quasi-fragile materials have some characteristic phenomena such as localization and size effects, among others, that could not be taken into account with this approach. The discrete element method has demonstrated considerable success in simulating the damage process in this kind of material. One of the advantages of this approach consists of capturing the transition between continuum and faults in a natural way. As a first approach, cracks are introduced in a lattice structure and the variations of the mechanical properties are evaluated comparing it with the analytical responses based on continuum damage theory. The finite element method and micromechanics concepts are incorporated for that purpose. The changes in the number of cracks and their sizes are analyzed, evaluating the overall behavior of the structure. Additionally, the study of the subdivision of the domain shows the intrinsic error associated with small DEM structure in describing the continuum with the applied technique. As a final scenario, the study of a lattice under progressive damage is carried out to evaluate the increasing anisotropy and loss of stiffness during a cyclic process.

Keywords
Lattice discrete element method (LDEM), Finite element analysis (FEA), damage mechanics, micromechanics, homogenization process.

Introduction

The evolution of the damage process in quasi-fragile materials, like ground stones concrete, and other synthetic composite materials, is an open problem in solid mechanics. The discussion developed by Krajcinovic (1996) [1] dealing with the classical damage methodology is inspiring. He and other authors developed and presented the discrete element method as an alternative where the continuum mechanics assumptions are loosened up to a certain point and the random distribution of properties can be easily incorporated. The discrete element models based on mass particles that interact by field functions, such as the one developed by Silling (2007) [2], is one of the alternatives. Another branch of research involves defining the interaction between the elements applying links that establishes a regular or non-regular structure. The latter method is hereon called Lattice Discrete Element Method (LDEM), where the solid is characterized by an interconnected web of uniaxial elements where the masses are located at the nodes.
The stiffness of each of these uniaxial elements is correlated directly with the solid material properties. The line elements yield a force field among the nodes that hold them together. The fracture is characterized, in these cases, as the result of an extreme reduction of the forces among nodes. Different approaches than the one applied in this work using LDEM can be found in Krajcinovic and Vujosevic (1998) [3], Sagar and Prasad (2009) [4], Nagy et al. (2010) [5], Schalangen (1995) [6] and Rinaldi (2011) [7]. The proposed lattice model used as a base in this work was developed by Riera (1984) [8]. The extracted data from the LDEM structure at different circumstances will be treated applying continuum damage mechanics concepts at two sets of examples. At the first, the theoretical results are known, and in the second, a more complicated situation will be evaluated.

The Lattice Discrete Element Method

The LDEM is based on a cubic arrangement with uniaxial element assuming a truss-like structure; therefore, only with three degrees of freedom. The basic module is described with twenty bars and nine nodes conceived initially by Nayfeh and Hefzy (1978) [9]. The problems regarding dynamic issues assume the masses concentrated at the nodes where the central node has half of the total mass, while each one of the remaining eight nodes has one-sixteenth of the total mass of the representative cube. The lengths of longitudinal and diagonal elements are L_n and $L_d = \sqrt{3}L_n/2$, respectively. The equations that relate the properties of the elements with the elastic constants of an isotropic medium are:

$$\delta = \frac{9\vartheta}{4-8\vartheta} \quad A_n = \frac{{L_n}^2(9+8\delta)}{2(9+12\delta)} \quad A_d = \frac{2\delta\, A_n}{\sqrt{3}} \tag{1}$$

The axial stiffness of the longitudinal and diagonal elements is defined as EA_n/L_n and EA_d/L_d, respectively, where ϑ and E values denote the Poisson's ratio and Young Modulus. In the case of Poisson's ratio equal to 0.25, the represented cubic arrangement shown in Figure 1a has the same constitutive relations as an isotropic continuum, while for different values of ϑ, the shear coefficients will progressively diverge. The dynamic system enforces at every node the motion equation:

$$\mathrm{M}u(\ddot{t}) + Cu(\dot{t}) + f(t) + p(t) = 0 \tag{2}$$

in which M represents the diagonalized mass matrix, u the generalized nodal displacements, C the diagonal damping matrix, $f(t)$ the internal forces operating on the lumped masses and $p(t)$ representing the external forces. The system is uncoupled and a central finite differences approach can be applied to integrate the motion equation over the time domain. The nodal coordinates are updated at each time-step, which

allows large displacements to be accounted for naturally. The simplest constitutive law applied for quasi-brittle materials was proposed by Hillerborg (1978) [10], considering a triangular element constitutive relationship (ECR) at each normal and diagonal element. It accounts for the irreversible effects of faults nucleation and propagation. Figure 1b shows the relation between force and strain where the area below the curve defines the energy density necessary to fracture the cross-section area of the element. Therefore, for any given point P at the curve, the grey area quantifies the dissipated energy density by the ongoing damage. At the moment the damage energy density reaches the total fracture energy, the link fails and loses the capacity to carry additional loadings. This behavior is assumed for components under traction and, due to the higher ability of quasi-fragile materials to endure much greater loads under compression, all elements are considered linear elastic in these circumstances independent of the load magnitude.

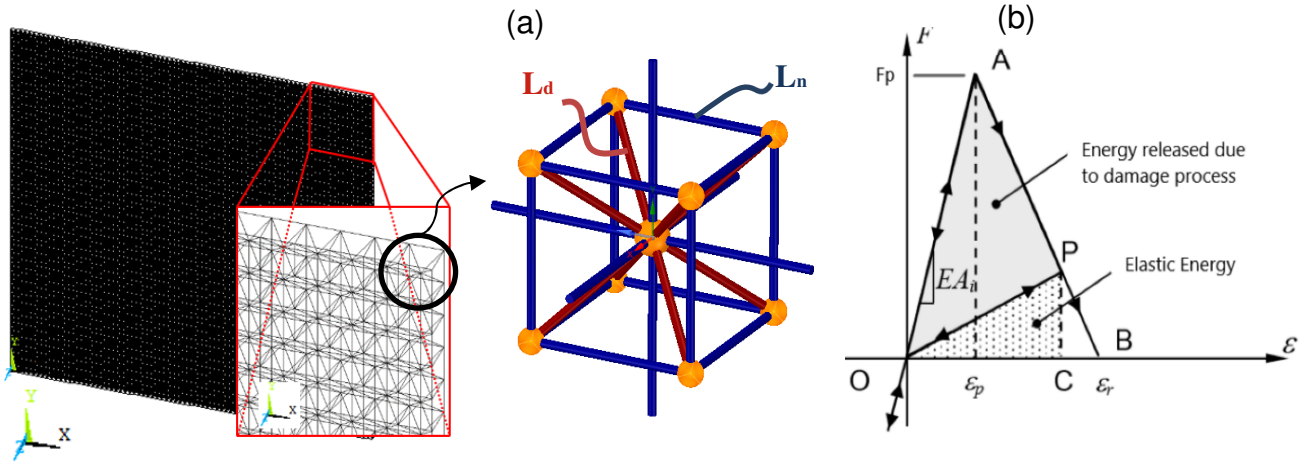

Figure 1. (a) The interconnected web and the single cubic arrangement defined by the LDEM scheme. (b) Constitutive law and energy released during damage and elastic energy recovered after unloading in the path OAB [Iturrioz et al., 2013].

Thus, failure in compression is induced by indirect tension. The element axial force F depends on the axial strain ε. An equivalent fracture area A_i^f, where the subindex i indicates if the bar is normal (n) or diagonal (d), must satisfy the equivalence of the energy dissipated by the fracture of the continuum and its discrete representation. Iturrioz et al. (2013) [11] studies and explores the fracture of a cubic sample of side L_n where this equivalence is detailed. As a consequence, the strains ε_p and ε_r (see Figure 1b) must be related to another material parameter, the characteristic length d_{eq}, employing the expressions:

$$\varepsilon_p = \sqrt{\frac{G_f}{E\, d_{eq}}} \qquad \varepsilon_r = \varepsilon_p d_{eq} \left(\frac{A_i^f}{A_i}\right)\left(\frac{2}{L_i}\right) \tag{3}$$

In principle, unstable fracture propagation requires that the characteristic length of the structure exceeds d_{eq}. The role of the characteristic length in the fracture process is discussed by Taylor (2007) [12]. It should be noted that ε_r depends on the material properties and also on the level of discretization. More details about the LDEM formulation employed in this paper may be found in previous contributions of other authors (Birck et al., 2016) [13].

The random distribution of material properties, which mimic the real materials, can take into account small perturbation on the mesh according to a normal distribution. Therefore, the performance prediction in compression improves, making the mean equal to zero and the coefficient of variation C.Vol. equal to 2.5%. Additional details introducing the geometric imperfection field can be found in Riera et al. (2014) [14]. Another form to mimic the random material nature consists of proposing the toughness G_f as a random field with a probability function of two-parameter Weibull function, defined by the mean value and the coefficient of variation. Additionally, the spatial field distribution is given by the correlating lengths in the three space directions. More information about these topics could be found in Puglia et al. (2019) [15].

The faults in Continuum Mechanics

The main objective of this work consists of linking the results obtained with LDEM and the classical micromechanics approaches. Gross and Seelig (2006) [16], among others, considers the multiphase case scenario introducing the so-called Representative Volume Element (RVE). For linear elasticity cases, the relationship between averages for the stress and strain fields implies the definition of an effective stiffness property C* or compliance property S* which are not related to the material property, but a mean of computing the correlation between different averaged fields of the RVE:

$$< \sigma >_{V_{RVE}} = C^* < \varepsilon >_{V_{RVE}} \quad \text{or}$$

$$< \varepsilon >_{V_{RVE}} = S^* < \sigma >_{V_{RVE}} \quad \text{where}$$

$$<\cdot> = \frac{1}{V}\int(\cdot)dv \tag{4}$$

Notice that the relation (4) also is called the Hill Principle, one of the fundamental concepts in the micromechanics framework (see Nemat-Nasser and Hori (1999) [17]). The phase ratio can be used as a weight parameter ($c_n = V_n/V_{RVE}$) where the subindex n represents the different phases of the mixture. If c_M represent the matrix volume ratio of the matrix, and c_c represents the particular case where the dispersed phases are fissures or cavities, we apply the framework of micromechanics to represent the continuum damage theory, propose originally by Kachanov (1958) [18]. Microcracks

distribution embodies the damage in this scenario. This dispersed phase has no contribution to the total volume; therefore, one can define the overall strain as the matrix strain $< \varepsilon_{ij} >_M$, c_M equals to one and the fraction of the crack c_c can be considered null. Applying the divergent theorem at the external area of the body ∂V and including the internal surface of the crack $\partial\Omega_c$, it is possible to derive:

$$< \varepsilon_{ij} > = c_M < \varepsilon_{ij} >_M + \frac{1}{2V} \cdot \int_{\partial\Omega_c} u_i n_j + u_j n_i \, \partial A = < \varepsilon_{ij} >_M + \underbrace{< \varepsilon_{ij} >_c}_{crack\ effect} \quad (5)$$

Otherwise, inverting the relation:

$$< \sigma_{ij} > = C_{ijkl_M}(< \varepsilon_{kl} >_M + \underbrace{< \varepsilon_{kl} >_c}_{crack\ effect}) \quad or$$
$$< \varepsilon_{ij} >= S_{ijkl_M} < \sigma_{ij} > + \underbrace{< \varepsilon_{kl} >_c}_{crack\ effect} \quad (6)$$

In this case, the crack strain tensor ε_c is related to the average strain field ε^0 by a damage influence tensor defined as J. Conversely, the stress path will lead to an influence tensor H. Equation (7) defines the effective elasticity tensors depending on the application of macrostrain ε^o or macrostress σ^o, respectively. The reduction of the matrix stiffness due to the presence of the damages inside the representative volume can be clearly observed:

$$S^{*\sigma} = S_M + H \quad or \quad C^{*\varepsilon} = C_M : (1 - J) \quad \text{where}$$
$$\varepsilon_c = H : \sigma^o = H : C_M : \varepsilon^o = J : \varepsilon^o \quad (7)$$

Several analytical solutions under different circumstances are available to compute the effect of cracks on the material properties. The Dilute approach takes the Eshelby solution directly, but it does not consider any interaction among the defects. Changes in the formulation allow the introduction of small interactions among the induced fields around the cracks, which permit higher fault densities. The Self Consistent (SC) method is one of them, where the changes in the in-plane overall shear (G) and Young Moduli (E) according to f in a plane strain state can be computed (Eq.8 - see Nemat-Nasser and Hori (1999) [17]). The term crack density parameter f is defined as the number of cracks N_f per unit area multiplied by the crack size parameter a^2, i.e., $f = N_f \cdot a^2$, establishing that all cracks have the same size $2a$. The solutions presented are for frictionless and permanently open faults. One observation about these methods is that for values larger than f >>0.15, neither Self-consistent nor Dilute methods are reliable approaches.

$$\overline{G^{(SC)}} = G(1 - f\,\pi)(1 - f\,\pi\vartheta)^{-1}$$
$$\overline{E^{(SC)}} = E(1 - \mathrm{f}\,\pi)(1 - f\,\pi\vartheta^2)^{-1} \quad (8)$$

Methodology

The damage evolution during the simulation process is translated into element stiffness degradation. The configuration of the LDEM model in several stages during the damage process is stored to explore the damage evolution in the LDEM model, using the continuum damage framework. This information is incorporated into an equivalent finite element model. The connecting elements are defined by tension/compression uniaxial components with three degrees of freedom at each one of the two end nodes. In the context of Ansys 18.2 (2018) [19], the element which fulfills these requirements is LINK180. As the structure presents different behavior under traction and compression due to its quasi-fragile constitutive law, the component can be defined to support tension-only (sectype = 1) or compression-only (sectype = -1). This option turns the numerical solution into a non-linear iterative process. Therefore, the model is characterized in the FEA scheme applying two overlapping pin-joints structures, where at each represented line element, two links can be activated depending on the load condition on a specific configuration. This configuration is defined as a "closed crack" scenario.

On the other hand, if the tractive constitutive law is also assumed for the compression regime, the study defines what is called "open cracks." The codes to convert the LDEM model into an FEA model are presented in the appendices of Giordani (2019) [20]. The global domain is defined as 79 x 79 x 1 cubic unities in plane strain state. Each cell is characterized by a length size (L_n) equal to 0.0075 m. The material properties consider the linear elastic behavior with Young's modulus equal to 35 GPa and Poisson's ratio of 0.25. A plane strain state requires three load conditions to define the components of a representative constitutive tensor (Figure 2a, b, c). In this study only a controlled strain situation is imposed, i.e., the input characterizes a constant strain ${\varepsilon^0}_{ij}$ over the domain defining a known displacement u_i at the boundaries x_j :

$$u|_{\partial\Omega_o} = {\varepsilon^0}_{ij} \cdot x_j \rightarrow {\varepsilon^{(I-III)}}_{ij} \cdot x_j \quad (9)$$

The three load cases are the constant axial strain in the x-axis, the constant axial strain in the y-axis and the constant shear deformation in the xy-plane. The application of such displacements is set at the central nodes of each unity cube (Figure 2d). When the configuration presents a certain degree of damage, the forces at the boundaries will decrease, because the stiffness was reduced, producing modifications on the constitutive tensor. These changes can be computed in many forms. One of them is establishing the damage tensor J making it possible to extract mechanical properties such as modified E_x, E_y and G, which are related directly to the diagonal terms of the new stiffness tensor.

A particular situation for the "closed cracks" regime must be pointed out. The local stiffness in these circumstances is dependent on the load conditions, i.e., the constitutive tensor is load-dependent and it will assume other values depending on how the three loads are set. "Open cracks," as the properties remain the same under compression or tension, the material properties will be independent of the load configuration.

Comparison with analytical solutions

The validation of the proposed approach could be done, comparing an LDEM model with some known classic pattern with a well-established solution. Specifically, an LDEM model with randomly oriented cracks with different sizes, orientation and quantity are used to compute the homogenized properties of the proposed internal structure. Faults with 4 x L_n, 7 x L_n and 11 x L_n, are spread randomly over the control volume (C.Vol.) defined by the plate domain of 79 x L_n of side, considering plane strain condition. Five random distributions

for each configuration tested are evaluated to characterize the statistical properties of the random response. Three simulation sets are considered:
4 x L_n case with up to 120 cracks ($f \approx 0.15$)
7 x L_n case considering up to 85 cracks ($f \approx 0.17$)
11 x L_n case, which reaches only 23 cracks ($f \approx 0.12$).

The Self-Consistent analytical solution is considered a reference for the homogenized properties computed for each level of f. Figure 3 shows examples for each crack size configuration under analysis. As follows, three aspects of the simulations are discussed:

(i) *The relation between E_x and E_y:*
In the implemented procedure, three elastic constants are computed: the in-plane Young' moduli E_x and E_y in the two orthogonal directions and the in-plane transversal modulus G_{xy}. The studied cases presented matrices with different fault densities randomly distributed, as illustrated in Figure 3. For these configurations, transversal isotropy for the simulated domain is expected; therefore, E_x and E_y must be equivalents. In Figure 4a the normalized values of E_x and E_y respect to the Young modulus of the matrix, for different levels of f, are displayed. The analytical solution obtained using the Self-consistent method is plotted with a blue line. The correlation between the blue line and the values obtained using the LDEM model are remarkably good up to $f \approx 0.1$. This result is expected because the analytical expression is valid for low values of f. In Figure 4b the same results displayed in Figure 4a are shown but considering the value E_{mean} as an averaged term of E_x and E_y. When comparing the two plots, it is possible to observe that the max. coefficient of variation of E_x and E_y reaches 8% and for E_{mean} it does not surpass 2%. The same tendency presented in Figure 4 occurs for the other simulation sets (4 x L_n and 11 x L_n).

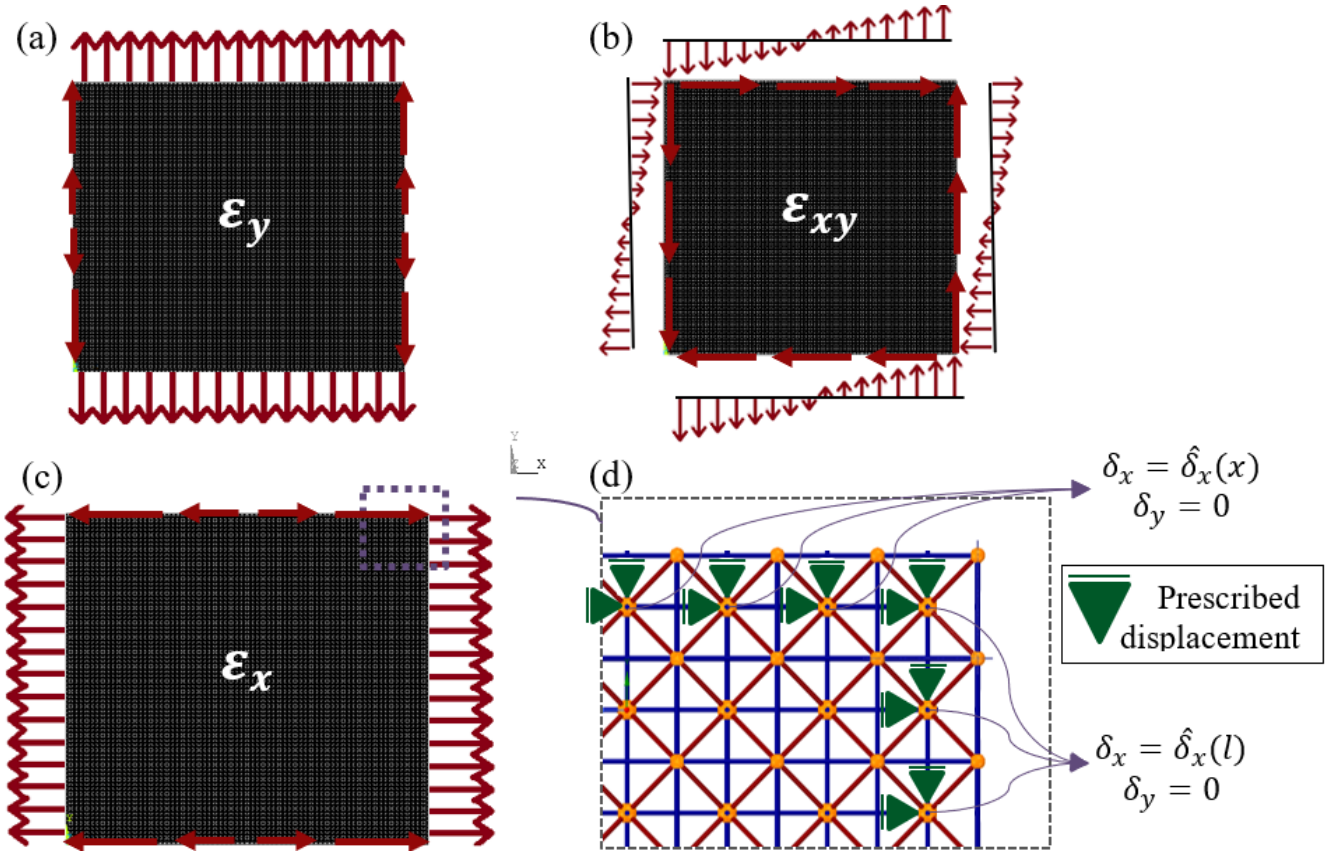

Figure 2. (a) Axial displacement at the border in u_y to generate a constant strain field ε_y. (b) Shear displacement in x and y direction to establish a constant strain field ε_{xy}. (c) Axial displacement at the border in u_x to generate a constant strain field ε_x. (d) Detail at the right top corner of case c showing the constrained central nodes.

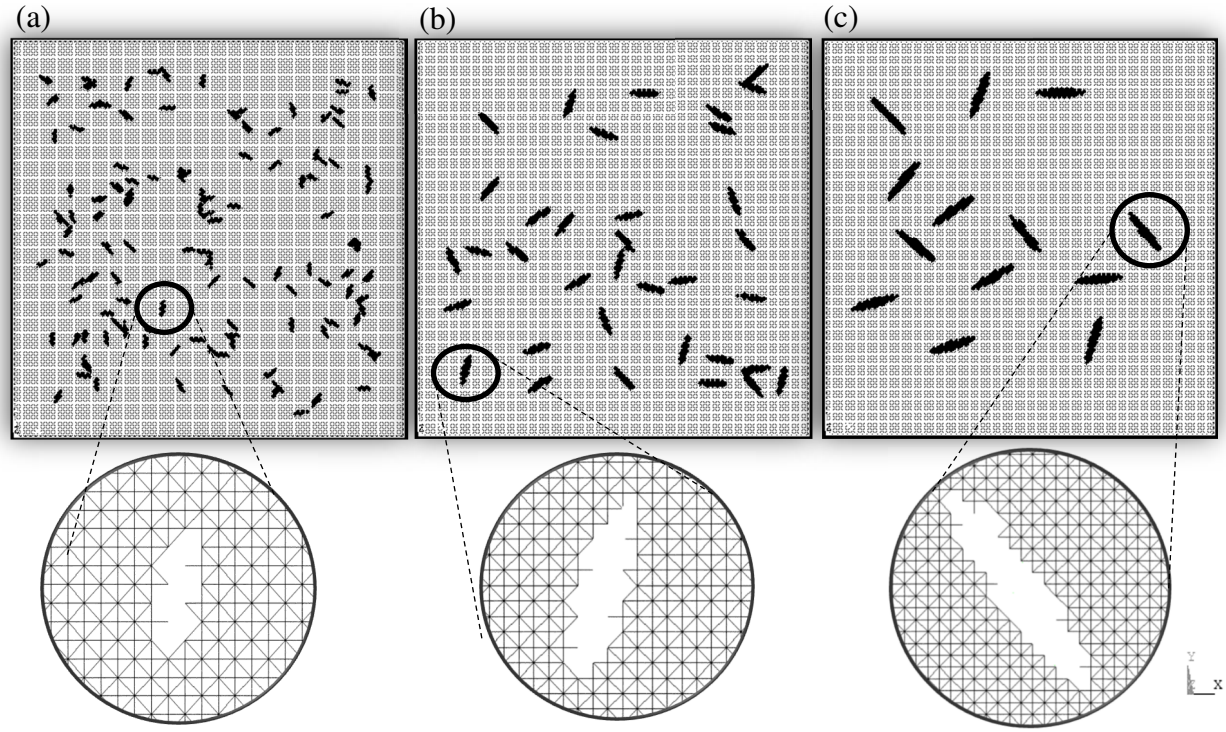

Figure 3. (a) Examples with a random distribution of cracks with 4 x L_n, (b) with 7 x L_n and (c) 11 x L_n over a control volume (C.Vol.) with 79 x L_n of side.

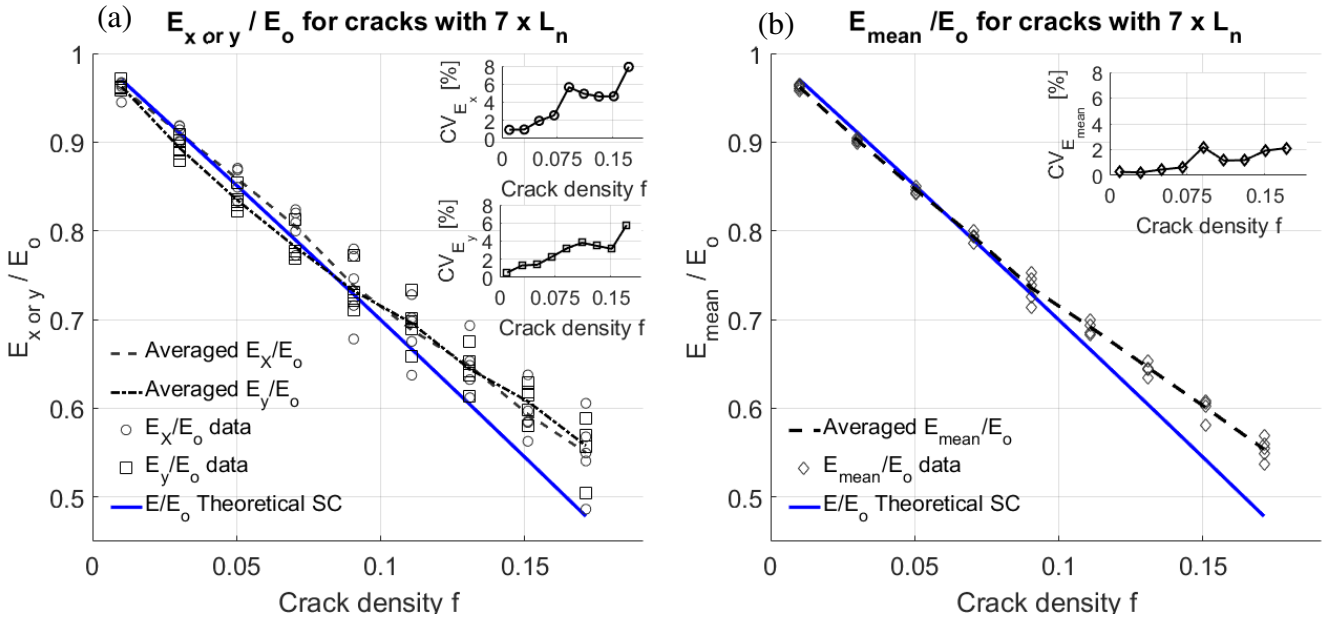

Figure 4. (a) E_x/E_o and E_y/E_o variation according to crack density f. The coefficient of variance (C.Vol.) is also presented for each axis. (b) Averaged relative Young's modulus using X and Y-axis values showing lower variation. 7 x L_n case. Faults overlapping each other is permitted.

(ii) *The influence of the fissure overlapping in the results:*
In the configuration illustrated in Figure 3, it is possible to observe that the cracks can overlap each other. In Figure 5a and b, the configuration comparison with and without overlapping are considered for faults set of 11 x L_n. Note that to create a configuration without defects overlapping, a restriction in the fissure generation must be taken. The results for both types of arrangements for f in the interval between [0.025, 0.04] are displayed and the results obtained show the same tendency.

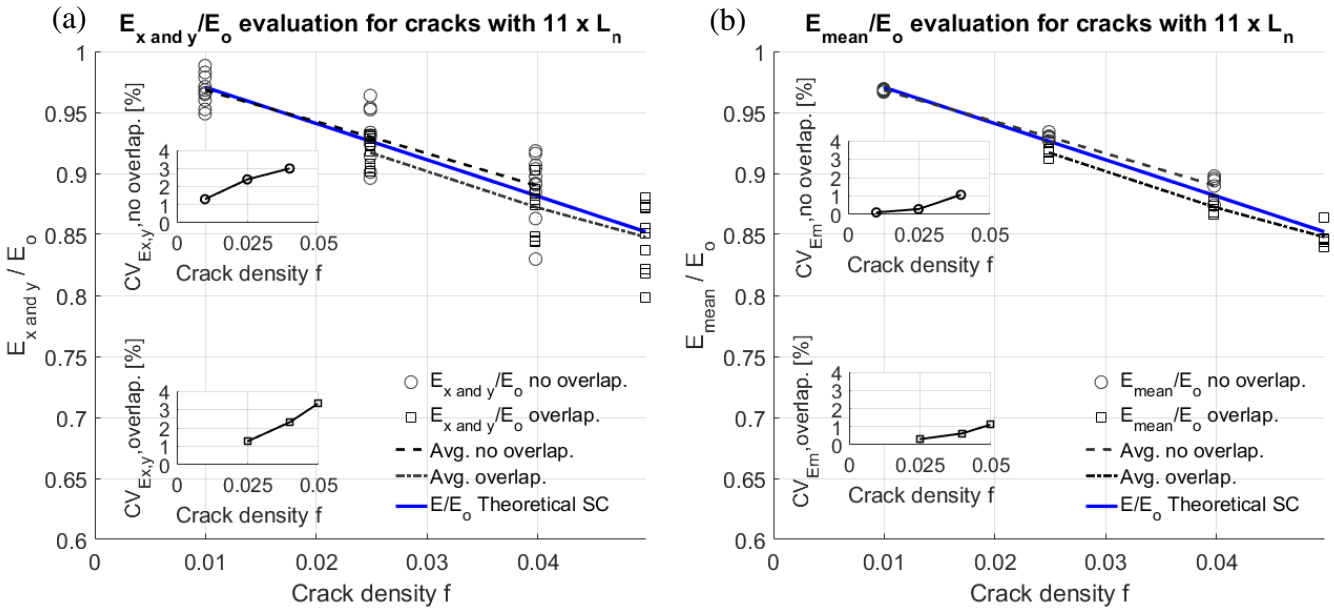

Figure 5. (a) E_x/E_o and E_y/E_o data are showing the domain with cracks with "no overlapping" and with "overlapping" allowed for small fault densities f. (b)The averaged relative Young's modulus at each case presents low C.Vol. variation (<2%). 11 x L_n case.

(iii) *Discussion about the result for the "Open crack" and "Close crack" situation:*

Controlled axial strains outward do not alter the results significantly when the cracks are "open" or "closed." However, the application of a constant shear strain will affect each fault differently depending on the chosen situation. Nemat-Nasser and Hori (1999) [17] demonstrates that for "closed cracks," the solution is non-linear and the effective properties are dependent on the stress configuration on the domain. Taking a region under shear stress, every single crack will be in a state of opening or closing that is highly dependent on the faults' angle. The integration of the individual responses will define the stiffness or compliance tensor. In this study, the shear modulus was extracted considering both scenarios. The "open crack" scheme shows a good agreement with the Self-Consistent approach and a considerably low variation of the coefficient of variance (<3% for the 7 x L_n case). However, the "closed cracks" study displayed approximately half of the value compared to the "open" one. Figure 6 plots the distributions and their respective coefficient of variation for both situations. Statistically, for a random distribution of cracks, half of all faults will be aligned at an angle that will induce a compression state when a shear process is assumed, which means an undamaged material property characterization ("closed" form). The other half will be in traction mode defining a 50% reduction of the G_{xy} relative to the "Open faults" scenario. The same was observed for the 4 x L_n and 11 x L_n cases where the coefficient of variation also progressively increases with the growing set of crack size.

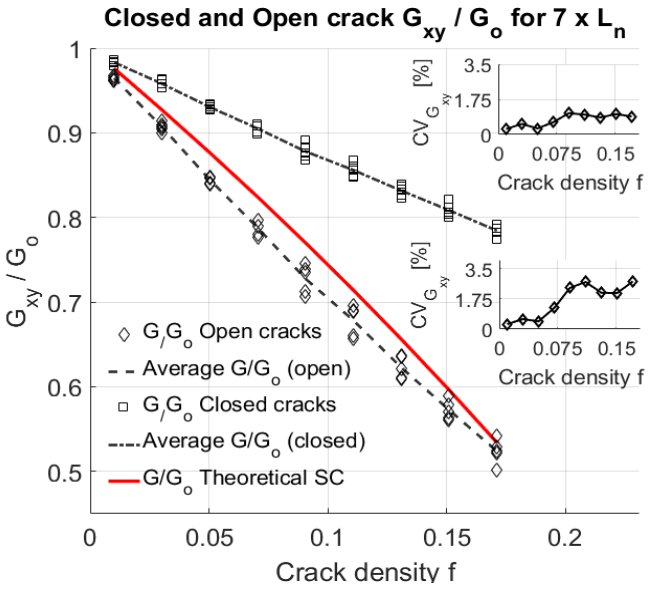

Figure 6. G_{xy}/G_o for "open" and "closed" cracks schemes. The "open" scenario is close to the theoretical Self-Consistent model, while the "closed" case has half the "open" case values. 7 x L_n case.

The dispersion of the simulation sets is presented in Figure 7 (4 x L_n, 7 x L_n and 11 x L_n) for different levels of crack density f with the results normalized respect the Self-Consistent solution. Only the "open faults" approach with overlapping allowed is displayed. The solutions in all the cases present an error < 4% for crack densities lower than $f = 0.1$. Remember that the Self-Consistent method is valid only for small values of f. Therefore, the technique here proposed to compute the effective properties using the LDEM model is successful in representing the actual loss of stiffness caused by a known distribution of faults.

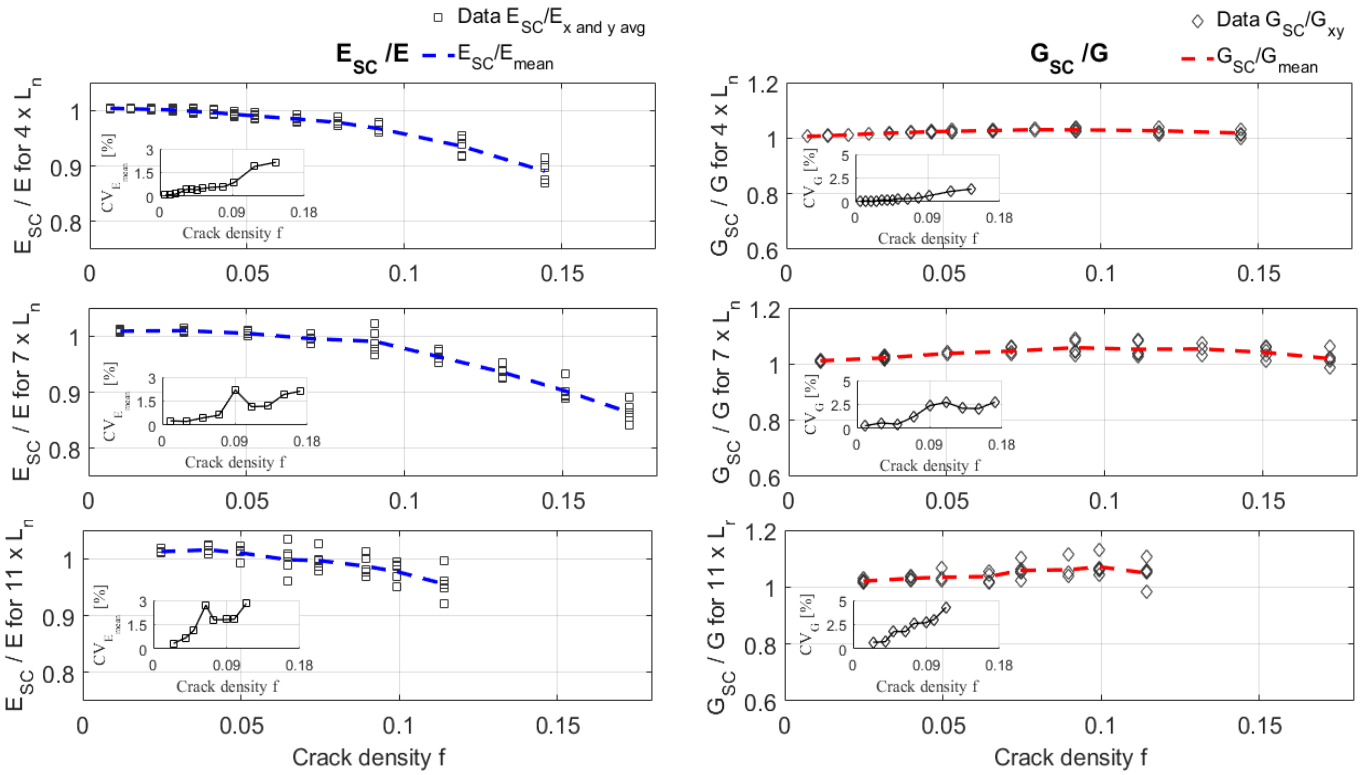

Figure 7. Relation E_{SC}/E and G_{SC}/G for "open cracks" at the three scenarios under analysis (4 x L_n, 7 x L_n, 11 x L_n). As the crack density f increases, the dispersion of the results also increases.

Application case: Nonproportional and proportional loading

In the present section, the LDEM method and the proposed methodology are applied for a square domain at plane strain state under multiaxial oscillating loading. The evaluation analyzes how the damage evolves over time. Two sets are considered, one is at proportional and the other at nonproportional loading. A proportional load establishes that shear stresses τ_{xy} and normal stresses σ_x are in-phase, while the nonproportional case implies a 90º out-of-phase normal and shear stresses. The two load cases are defined with stress amplitudes that will generate the same number of cycles until the moment of rupture; therefore, the stress amplitude differs between the nonproportional and proportional scenarios, as depicted in Figure 8. More detailed about this example can be founded in Soares (2019) [21].

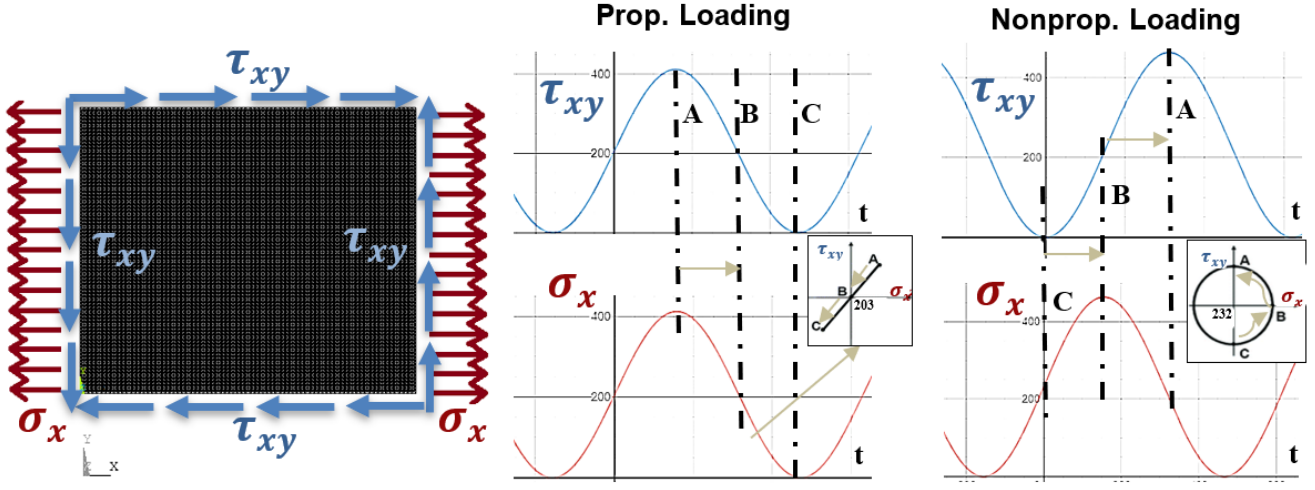

Figure 8. The proportional and nonproportional sinusoidal stress σ_x and τ_{xy} set at the domain's borders during the LDEM simulation. Stress ratio R = 0 at plane strain state.

During the damage evolution, the stiffness of each element can be stored at different time-steps and the effective properties variation over time can be analyzed. The relative parameters E_x, E_y and G at each moment are computed using the same approach described in the previous section.

The results are presented in Figure 9, where the effective properties evolution up to 40% of the total lifespan is displayed. It is possible to verify that the nonproportional loading produces more damage compared to the proportional one. Additionally, the Young modulus in the X-direction is the one that suffers a considerably higher level of damage. Therefore, the values of E_x and E_y evolves differently during the damage growth, which will lead to an anisotropic description of the media during the process

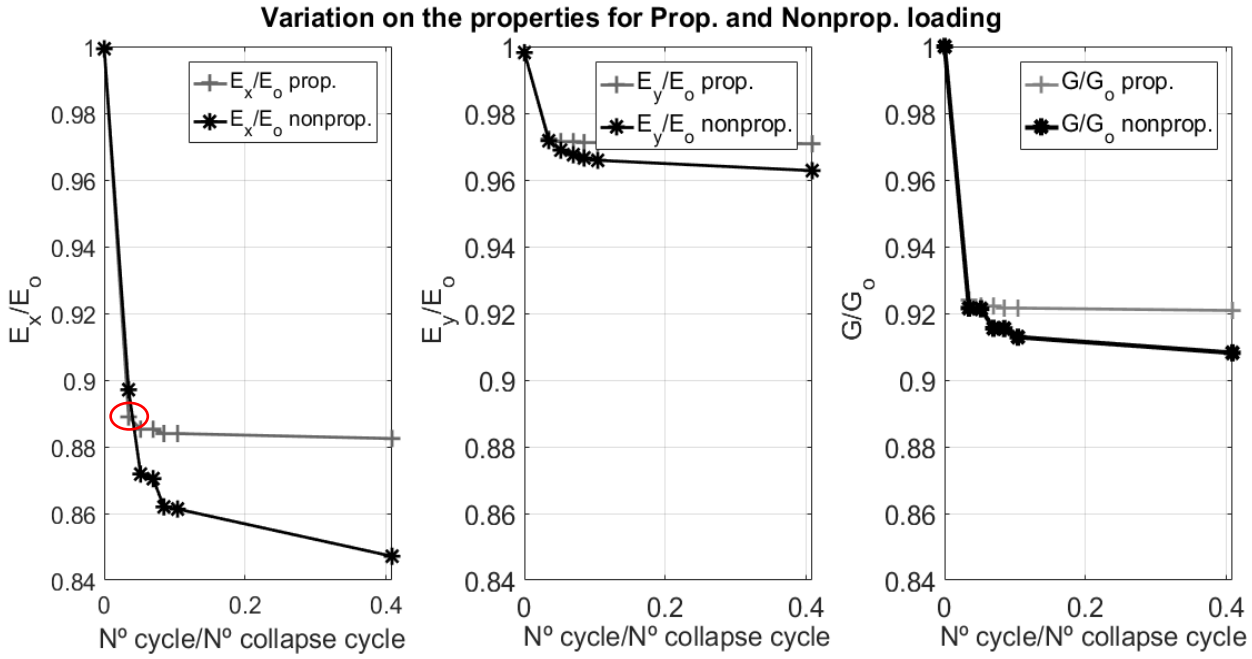

Figure 9. (a) X-axis relative Young's modulus, (b) Y-axis relative Young's modulus and (c) relative shear modulus variation with increasing damage over a cyclic process evaluated at nonproportional and proportional conditions up to 40% of the total lifespan. Plane strain state.

Effect of decreasing Control Volume

The body under investigation is composed of 79 x 79 cubic cells where the loads are prescribed at the central nodes at the borders. The undamaged domain provides almost the same result as the continuum mechanical approach by an error of 0.2%. In the following analysis, the outer region comprised of 4 cubic cells is disregarded due to some consideration for the application of the forces (see Soares (2019) [21]). Then, the volume of interest will be described with 70 x 70 cubic cells. The problem here consists of investigating how the effective properties will be modified when the control volume (C.Vol.) decreases. In the present study, the model without damage is analyzed over different dimensions of the C.Vol.. The model is subdivided into domains with 2 x 2 up to 70 x 70 cubic cells to evaluate the undamaged variation of the in-plane elastic values $E_{x\ or\ y}$. The scheme presented in Figure 10a illustrates the division when the C.Vol. has 14 x 14 cubic cells. Figure 10b shows that for small C.Vols., such as 2 x 2 cubic cells, the DEM proposition will return values equal to 94.5% of the classical mechanics, i.e., an error of 5.5%. The increasing C.Vol. size decreases the error exponentially, achieving values inferior to 1% for domains larger than 25 x 25 cubic cells.

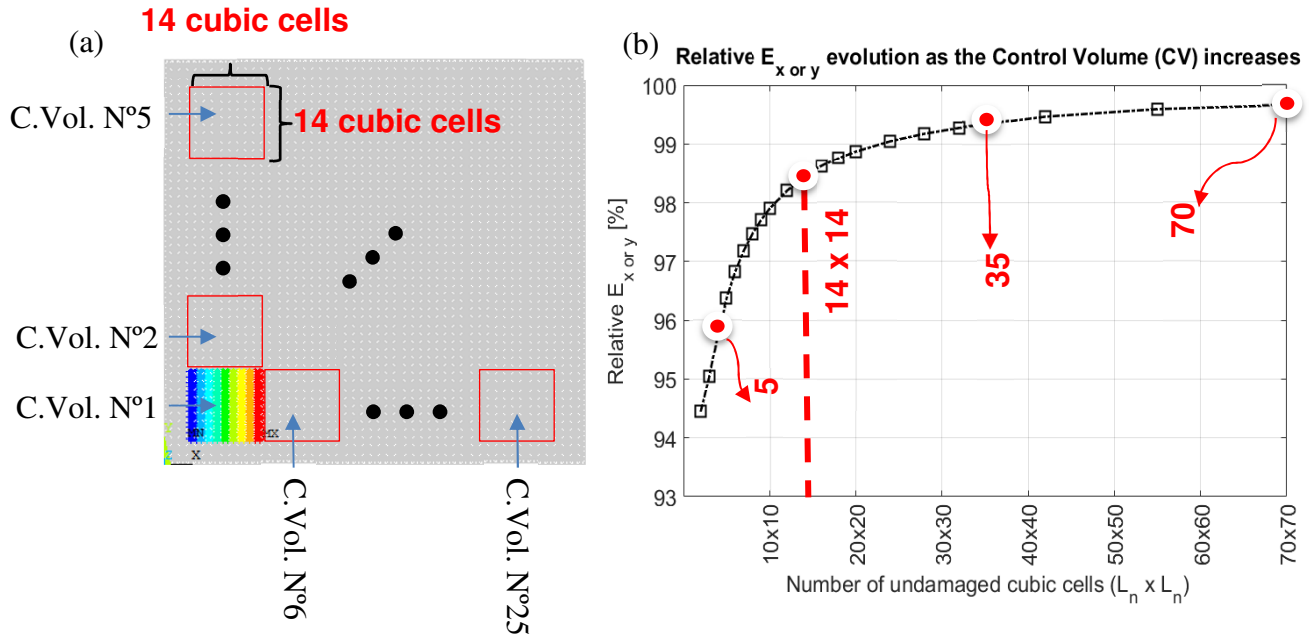

Figure 10. (a) Example of model subdivision into 25 subregions formed by 14 x 14 cubic cells (b). The effect on $E_{x\ or\ y}$ as the control volume (C.Vol.) decreases from 2 x 2 up to 70 x 70 cubic cells. Example 14 x 14 is presented at (a) and highlighted in red-dash at (b).

The analysis of the local variation allows us to evaluate how the local parameter will change according to the coordinate point. To demonstrate this effect, the time-step under proportional loading equal to 3.5% of the total lifespan, indicated with a red circle in Figure 9a, was chosen to analyze how the decreasing control volume (C.Vol.) will modify the material properties. The application of such technique provides support to define a consistent Representative Volume Element (RVE) depending on how the variation of properties will be displayed over the body. Figure 10a shows the dissipated energy extracted from the LDEM model developed by Soares (2019) [21]. It is possible to observe peaks where clusters of microcracks are forming, defining the potential sources of growing fissures. An example of how the relative E_x is affect as the domain decreases from 70 x 70 to 5 x 5 cubic cells is shown in Figure 11b, c, d, e. The largest subdivision presents a considerable variation in the damaged regions compared to undamaged areas. It is possible to extract the effective properties from these different control volumes (C.Vol.). The analysis can be presented by an average and their dispersion (Max. – Min.) as shown in Figure 12 for E_x, E_y and G_{xy}. It is evident that the variation increments as the C.Vol. decreases, which also means that the equivalent property for the whole body (RVE) becomes more imprecise. On the other hand, when the subdivision is small, as, e.g., with four subdomains, the interval Max. – Min. is subtle. Therefore, it can be said that for the 70 x 70 cubic cells scenario (1 subdivision), the C.Vol. is a good approximation of the RVE.

It is interesting to observe the averaged values for the relative E_x and E_y. A constant factor dislocates their curves from the undamaged cases (blue line). This fact becomes clearer for G where the undamaged curve is not affected by the domain size as occurred for E_x and E_y.

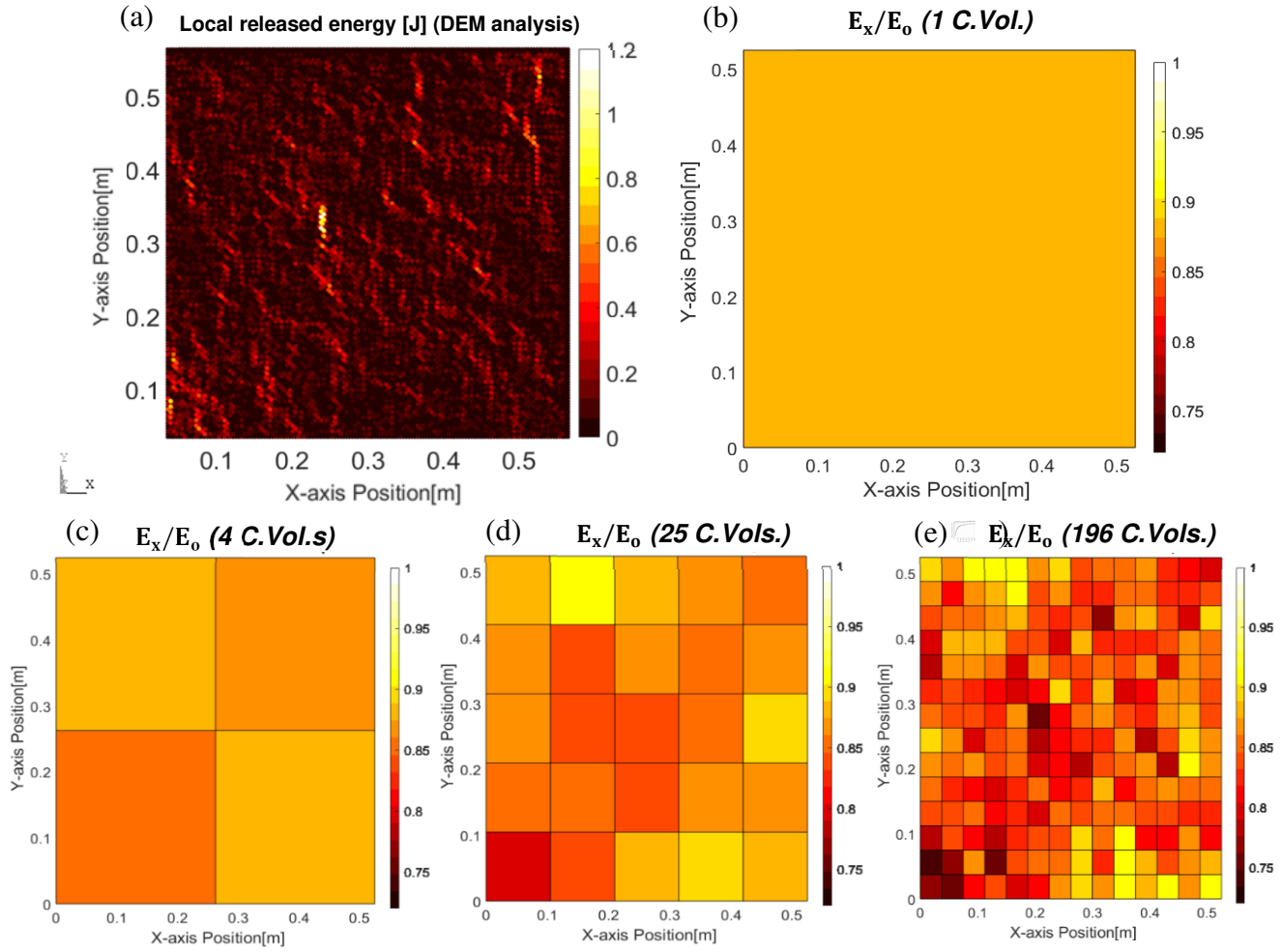

Figure 11. (a) The released energy showing clusters of crack formation. Extracted from Soares [21]. (b) Plate's discretization in 1 C.Vol. (70 cubic LDEM modules of side), (c) in 4 C.Vols. (35 cubic LDEM modules of side), (d) in 25 C.Vols. of (14 cubic LDEM modules of side) and in 196 C.Vols. (5 cubic LDEM modules of side). Case at 3.5% lifespan observing E_x/E_o for the proportional cyclic load.

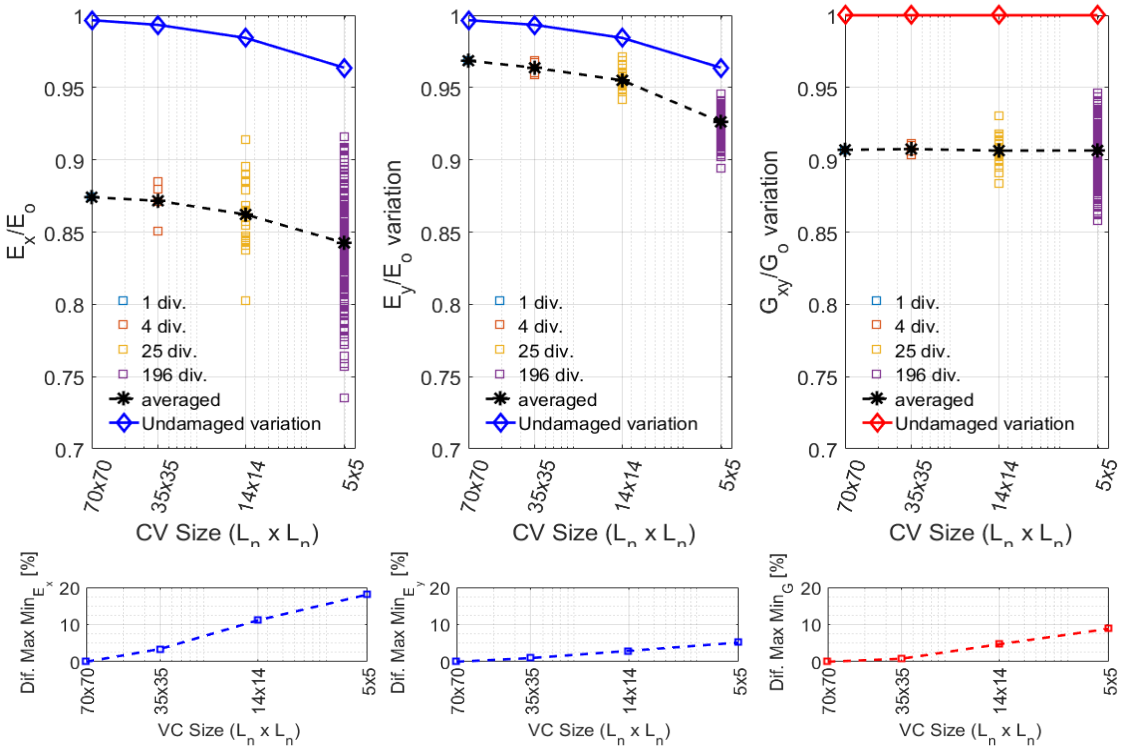

Figure 12. E_x/E_o, E_y/E_o and G/G_o variation decreasing the control volume (C.Vol.) size. The difference between max. and min. at each plot shows how the subdivision of the damaged body into smaller domains causes the dispersion of the properties caused by clusters of cracks

Conclusion

The application of the homogenization procedure in an LDEM model is a capable tool of correlating the continuum mechanics and the discrete models. The comparison between analytical and the numerical solution for a random distribution of cracks presented excellent agreement considering the extracted properties. Additionally, the given variations were consistent with micromechanics concepts, where the size of the defects influences precisely the description of an RVE. Additionally, the study of "open" and "closed" faults was performed without enforcing any new theory, which supports the argument that the LDEM approach naturally mimics the continuum description.

The example of proportional and nonproportional cycling loads considering 70 x 70 cubic cells showed that after the initial steps, the overall properties do not change significantly at the global scale as also predicted by Soares (2019) [21] which considered the released energy during damage evolution. Nevertheless, the nonproportional case has clearly caused a more significant impact on structural properties.

An analysis considering the effect of the domain size has demonstrated that as the size of the C.Vol. gets smaller, inconsistencies between numerical and the analytical evaluations start to grow up to 5% for mechanical properties as E_x and E_y . However, for domains larger than 25 x 25 cubic cells, the variation is lower than 1%, and useful predictions can be made. Despite the intrinsic error for small C.Vols., the break of the damaged body into several subdomains presented averaged mechanical properties equal at all cases disregarding the inherited variation of the undamaged media. The analysis of the dispersion of the values is also introduced to establish a way to converge the control volume towards a consistent RVE description.

Despite the examples presented, the methodology is easily adaptable to be applied along with the LDEM approach, serving as a collaboration to extract more information of the media under investigation.

Acknowledgements

The author wishes to thank the National Council for Scientific and Technological Development (CNPq – Brazil) and Coordination for the Improvement of Higher Education Personnel (CAPES – Brazil) for funding this research

References

1. Krajcinovic, D., **Damage mechanics**, North-Holland, Amsterdam, 1996.
2. Silling, S.A. et al., **Peridynamics states and constitutive modeling**, *Journal of Elasticity*, 88, pp. 151-184, 2007.
3. Krajcinovic, D. and Vujosevic M., **Intrinsic Failure Modes of Brittle Materials,** *Int. J. Solids Structures*, Vol. 35, No.19, pp. 2487-2503, 1998.
4. Sagar, R.V., Prasad, B.K., **Modeling heterogeneity of concrete using 2D lattice network for concrete fracture and comparison with AE study**, *Sadhana*, 34(6), pp. 865-886, 2009.
5. Nagy, E., Landis, E.N., David, W.G., **Acoustic emission measurements and lattice simulations of microfracture events in spruce**, *Holzforschung*, 64, pp 455-461, 2010.
6. Schlangen, E., van Mier, J.G.M, **Crack propagation in sandstone: combined experimental and numerical approach**, 2005 *Rock Mechanics and Rock Engineering*,

28(2), pp. 93-110, 2005.
7. Rinaldi, A., **Damage Mechanics and Micromechanics of Localized Fracture Phenomena in Inelastic Solids**, CISM Courses Series, Springer, 2011.
8. Riera, J.D, **Local effects in impact problems on concrete structures**, Conference on Structural Analysis and Design of Nuclear Power Plants, Vol.3, 1984.
9. Nayfeh, A.H, Hefzy, M.S., **Continuum modeling of three-dimensional truss-like space structures**, *AIAA Journal*, 16(8), pp. 779-787,1978.
10. Hillerborg, A., **A model for fracture analysis**, Division of Building Materials, The Lund Institute of technology, Lund University, 1978.
11. Iturrioz I., Lacidogna G., Carpinteri A., **Experimental analysis and truss-like discrete element model simulation of concrete specimens under uniaxial compression,** Engineering Fracture Mechanics, 110, 81-98, 2013.
12. Taylor D., **The Theory of Critical Distances: A New Perspective in Fracture Mechanics**, Elsevier, 2007.
13. Birck G., Iturrioz I., Lacidogna G., Carpinteri A., **Damage process in heterogeneous materials analyzed by a lattice model simulation**, *Engineering Failure Analysis*, 70, pp. 157-176, 2016.
14. Riera, J. D., Miguel, L. F. F., Iturrioz I.**, Assessment of Brazilian tensile test by means of the truss-like Discrete Element Method (DEM) with imperfect mesh.** *Engineering Structures***,** 81, pp. 10-21, 2014.
15. Puglia, V.B, Kosteski, L.E, Riera J.D, Iturrioz, I., **Random field generation of the material properties in the lattice discrete element method**, *Journal of strain analysis for engineering design*, v.54, 2019.
16. Gross, D. and Seelig, T., **Fracture Mechanics – With an Introduction to Micromechanics**, Mechanical Engineering Series, Springer, Germany, 2006.
17. Nemat-Nasser S. and Hori M., **Micromechanics: overall properties of heterogeneous materials.** North-Holland Series in Applied Mathematics and Mechanics, 1999.
18. Kachanov L., **Time of the rupture process under creep conditions**. *TVZ Akad Nauk S.S.R. Otd. Tech. Nauk*, 8, pp. 26-31, 1958.
19. **Ansys ® Workbench18.2** - Ansys Mechanical Product, Ansys, Inc. Products Release 18.2., 2017.
20. Giordani, G., **Continuum damage evaluation and homogenization process in quasi-fragile materials simulated using lattice discrete element method***, Thesis (Master)*, Universidade Federal do Rio Grande do Sul, Porto Alegre, Brazil, 2020
21. Soares, F. S., **Modelagem de Fenômenos de Fadiga em Materiais Quase Frágeis Heterogêneos Utilizando uma Versão do Método de Elementos Discretos Formado por Barras**. *Thesis (Doctorate),* Universidade Federal do Rio Grande do Sul, Porto Alegre, Brazil, 2019.